Order Number 9010487

Tropical squall lines of the Arizona monsoon

Smith, Walter Prestont, Ph.D.

The University of Arizona, 1989

U·M·I
300 N. Zeeb Rd.
Ann Arbor, MI 48106

TROPICAL SQUALL LINES OF THE ARIZONA MONSOON

by

Walter Prestont Smith

A Dissertation Submitted to the Faculty of the

DEPARTMENT OF ATMOSPHERIC SCIENCES

In Partial Fulfillment of the Requirements
For the Degree of

DOCTOR OF PHILOSOPHY

In the Graduate College

THE UNIVERSITY OF ARIZONA

1989

THE UNIVERSITY OF ARIZONA
GRADUATE COLLEGE

As members of the Final Examination Committee, we certify that we have read the dissertation prepared by Walter Prestont Smith

entitled Tropical Squall Lines of the Arizona Monsoon

and recommend that it be accepted as fulfilling the dissertation requirement for the Degree of Doctor of Philosophy.

Robert L. Gall	8/23/89 Date
William D. Sellers	8/23/89 Date
Dean O. Staley	8/23/89 Date
Owen K. Davis	8/23/89 Date
	Date

Final approval and acceptance of this dissertation is contingent upon the candidate's submission of the final copy of the dissertation to the Graduate College.

I hereby certify that I have read this dissertation prepared under my direction and recommend that it be accepted as fulfilling the dissertation requirement.

Dissertation Director	9/13/89 Date

STATEMENT BY AUTHOR

This dissertation has been submitted in partial fulfillment of requirements for an advanced degree at The University of Arizona and is deposited in the University Library to be made available to borrowers under the rules of the Library.

Brief quotations from this dissertation are allowable without special permission, provided that accurate acknowledgement of source is made. Requests for permission for extended quotation from or reproduction of this manuscript in whole or in part may be granted by the copyright holder.

SIGNED: Walter Prescott Smith

ACKNOWLEDGEMENTS

I would like to thank the members of my committee, Bob Maddox, and Glenn Rasch for their comments and suggestions. This research was supported by NASA grant NAS8-36278. Additional funding came from NASA training grant NGT-03-002-808. The numerical simulations were run on the computing system at NCAR which is supported by the National Science Foundation.

TABLE OF CONTENTS

TABLE OF CONTENTS--Continued

LIST OF ILLUSTRATIONS

LIST OF ILLUSTRATIONS--Continued

LIST OF ILLUSTRATIONS--Continued

LIST OF ILLUSTRATIONS--Continued

LIST OF ILLUSTRATIONS--Continued

LIST OF ILLUSTRATIONS--Continued

LIST OF TABLES

ABSTRACT

Squall lines possessing nearly all the characteristics of tropical squall lines occasionally develop during the summer monsoon over southern Arizona and northwestern Mexico. Initial thunderstorm formation is over the mountains along the Continental Divide in the late afternoon. Satellite imagery, cloud-to-ground lightning strike data, and surface observations indicate the squall lines move from east to west or northeast to southwest by discrete propagation faster than all the winds below 20 kPa so that most of the anvil clouds lag behind.

The synoptic-scale circulation is anomalous with a strong ridge located over the western United States and a deep trough located over the eastern United States. West to northwest winds are found in the boundary layer over southern Arizona and northwest Mexico while a deep layer of east winds are observed above. As a result, most of the environmental wind shear is confined to the lowest 2.5 km above the ground. The low-level wind shear seems to be required for the westward propagation of thunderstorms and the formation of the squall lines. Extremely dry midtropospheric air develops in the easterly flow through some combination of advection and subsidence and also appears to

be an important factor in the development of the squall lines.

A two-dimensional, nonhydrostatic, numerical model was able to simulate many of the features observed in these squall lines. Solar heating of the elevated terrain in the model caused the initial thunderstorm to develop over the Continental Divide. Continued development of new thunderstorms to the west of the Divide produced a squall line that travelled westward by translation of cells and discrete propagation, wherein new cells would develop 10-25 km ahead of the old ones, at a speed greater than all the winds below 30 kPa.

Upward motion produced by westward propagating gravity waves and by the strong low-level convergence found just ahead of the gust front appeared to cause several episodes of discrete propagation. The creation of horizontal potential temperature gradients and the vertical and horizontal advection of preexisting vorticity gradients combined to produce the vorticity field associated with the rear inflow jet that developed beneath the simulated squall line.

CHAPTER 1

INTRODUCTION

The weather of Arizona generally is benign most of the year, especially when compared to that of the rest of the United States. Nevertheless, Arizona sometimes experiences severe weather, usually damaging downburst winds and flash flooding, with the greatest frequency in the summer monsoon which normally begins during the first or second week of July and ends in the middle of September. The monsoon commences when the westerlies migrate northward over North America and change the circulation aloft over Arizona so that dry west to southwest winds are replaced by moist south to southeast winds. This change of wind direction is immediately followed by a sharp increase in cloudiness and precipitation. As seen in Table 1.1, which lists average monthly precipitation at several stations (their locations are shown in Fig. 4.18) in Arizona and the neighboring state of Sonora, Mexico. July rainfall averages more than 900% of that in June. Precipitation increases to the south and with elevation so that the mountains of southern Sonora receive by far the highest totals.

When monsoon conditions prevail, isolated to scattered showers and thunderstorms develop every day, and although

TABLE 1.1 Average Monthly Precipitation (mm) during the Summer Monsoon at Selected Stations in Arizona and Sonora, Mexico.

Station		Elev. (m)	Jun	Jul	Aug	Sep
Arivaca 1 E, Az.	(ARI)	1121	10.7	107.4	87.6	44.7
Douglas, Az.	(DOU)	1232	15.0	100.8	73.4	36.6
Kitt Peak, Az.	(KTP)	2074	11.4	105.4	112.3	63.8
Redington, Az.	(RED)	883	7.8	74.7	55.6	27.9
Tucson WSO, Az.	(TUS)	789	6.1	64.5	51.6	34.0
Hermosillo, Son.	(HMO)	200	5.9	66.9	74.2	29.0
Nacozari, Son.	(NAC)	1100	20.4	141.0	94.5	59.4
Santa Ana, Son.	(STA)	690	9.4	96.2	84.5	39.0
Yécora, Son.	(YEC)	1500	60.4	260.0	208.4	81.4

the rains typically are light, their frequent occurrence sometimes generates relatively large monthly totals. Nonetheless, research currently in progress has determined that a significant fraction of the precipitation during the summer monsoon comes from disturbances: easterly waves; lows that form along the monsoon boundary (Adang and Gall 1989 and Moore et al. 1989); weakening or dissipated tropical cyclones (Smith 1986); and mesoscale convective systems (MCSs) which develop either from isolated clusters of thunderstorms that merge or from squall lines. The purpose of this research is to show that tropical squall lines composed of strong to severe thunderstorms occasionally develop over Arizona and Sonora, Mexico during the summer monsoon and to simulate the initiation and development of these squall lines with a two-dimensional (2D) numerical model.

A tropical squall line is a MCS composed of a leading edge of strong convection that propagates faster than the winds at most if not all levels in the troposphere and thus leads to inflow ahead and outflow behind the squall line which is followed by a large anvil cloud (Hamilton and Archbold 1945; Zipser 1969, 1977; Houze 1977; Houze and Betts 1981; Gamache and Houze 1982, 1985; Houze and Rappaport 1984; Chong et al. 1987; Roux 1988). Convective-scale

downdrafts from thunderstorms along the squall line form a gust front at the surface and are associated with a relatively brief period of heavy rain. In addition, a mesoscale unsaturated downdraft forms beneath the trailing anvil cloud. The anvil cloud may arise partly from mesoscale ascent caused by midtropospheric convergence and heating to the rear of the squall line and is associated with a much longer period of light rain (Zipser 1969, 1977; Leary and Houze 1979a,b; Leary 1979; Gamache and Houze 1982, 1985; Houze and Rappaport 1984).

Studies of squall lines at midlatitudes have demonstrated that some of these systems also possess many of the features found in tropical squall lines (see Maddox 1980; Ogura and Liou 1980; Bluestein and Jain 1985; Smull and Houze 1985, 1987a,b; Srivastava et al. 1986; Hane et al. 1987; Kessinger et al. 1987; Leary and Rappaport 1987; Maddox et al. 1987; Rutledge and Houze 1987; Rutledge et al. 1988). However, some squall lines at midlatitudes are noticeably different from their tropical counterparts. Rotunno et al. (1988) argue environmental wind shear is responsible for the differences and believe there are only two types of long-lived squall lines: those that develop in an environment of pronounced low-level shear, typically oriented perpendicular to the line, with weak shear aloft;

and those that form where the shear, usually at an angle to the line, is stronger and extends to higher altitudes.

One of the earliest simulations of a tropical squall line was performed by Moncrieff and Miller (1976) who found the propagation speed of a cell relative to the midlevel flow in their steady-state model was mostly a function of the convective available potential energy, CAPE, of the environment. Later, Miller and Betts (1977) stated the mesoscale unsaturated downdraft under the trailing anvil in their model was dynamically induced by a spreading density current while Brown (1979) concluded it was produced mainly by the evaporation of raindrops in his model.

Most tropical squall line simulations have been initialized with data obtained from either the eastern tropical Atlantic or adjacent West Africa and have been run in two dimensions due to limited computer resources. However, there have been some three-dimensional (3D) and quasi-3D experiments (Bolton 1984, Pointin 1985, Rotunno et al. 1988, Redelsperger and Lafore 1988, Nicholls and Weissbluth 1988). Rotunno et al. (1988) compared the results of 2D and 3D simulations and found there were no significant differences. Similarly, Nicholls and Weissbluth (1988) concluded that in some circumstances 2D and 3D simulations yield nearly identical results. In light of these findings

and the limited computer resources available, a 2D version of T. L. Clark's model (see Clark 1977, 1979, Clark et al. 1987) was utilized to simulate the tropical squall lines described in chapter 4.

A low-level density current produced by evaporating rain and water loading has been invoked by many researchers as the primary reason for the generation of new cells and the propagation of the multicellular tropical squall lines observed in the eastern tropical Atlantic and West Africa (Pointin 1985, Dudhia et al. 1987, Nicholls 1987, Redelsperger and Lafore 1988, Nicholls et al. 1988, Nicholls and Weissbluth 1988, Lafore and Moncrieff 1989) and in Venezuela (Moncrieff and Miller 1976, Miller and Betts 1977). Nevertheless; Dudhia et al. (1987), Nicholls et al. (1988), and Lafore and Moncrieff (1989) discovered that a density current did not form when the tropical easterly jet was removed from their initial wind profiles and the magnitude of the upper-level wind shear was reduced. They found the development of new convection and the propagation of this "unicell" squall line was caused by surface convergence at the gust front which resembled a propagating gravity wave.

Observations presented by Ley and Peltier (1981) and Lu et al. (1984) showed gravity waves were produced by distant

thunderstorms while Kuettner et al. (1987) pointed out that convection in a heated boundary layer can also generate gravity waves. The propagating gravity waves seen by Ley and Peltier (1981) had a 10 km horizontal wavelength, moved at 12 ± 5 m s^{-1}, and caused banded clouds to form when they moved into a favorable environment several hundred kilometers from the apparent source, a severe thunderstorm. Data obtained from dual-Doppler radar analyses suggest gravity waves may initiate and enhance convection along colliding outflow boundaries (Mahoney 1988).

Gravity waves have been noted in many numerical simulations. For example, Brown (1979) detected gravity waves moving away from his simulated tropical squall line at 12-16 m s^{-1} relative to the mean zonal flow. Droegemeier and Wilhelmson (1985) stated gravity waves modified the collision line between two simulated thunderstorm outflows. Convection in a heated boundary layer generated gravity waves in the overlying free troposphere which then helped organize the boundary layer eddies and clouds in the simulations of Clark and Hauf (1986), Clark et al. (1986), and Hauf and Clark (1989). Furthermore, simulations performed by Balaji and Clark (1988) implied deep convection was initiated when the upward motion in the free tropospheric gravity waves moved in phase with the upward motion of the

boundary layer eddies. Gravity waves also seemed to help organize both dry and moist convection over an idealized topographic profile of the western Great Plains of eastern Colorado in the experiments carried out by Redelsperger and Clark (1989).

The deep convection in the tropical squall line simulations of Redelsperger and Lafore (1988) and Nicholls et al. (1988) produced numerous gravity waves. Waves produced by the convection in the experiments of Nicholls (1987) and Crook and Moncrieff (1988) seemed to cause clouds to grow out ahead of their MCSs. In the former case, cumulonimbus developed when the gust front moved under these clouds while in the latter, new cells were seen to form approximately 10 km in advance of the main squall line updraft and low-level cold pool. Tripoli and Cotton (1989a,b) noticed the deep convection in their simulated midlatitude MCS generated gravity waves which, in the 50% wind case (Tripoli and Cotton 1989b), appeared to initiate new convection and cause discrete propagation of the system. Schmidt and Cotton (1989) believe many of the features observed in 2D squall line simulations are related to the interaction of lower and upper tropospheric gravity waves in a sheared environment.

Wave theory has already been utilized by Raymond (1984)

in his wave-CISK model and by Bolton (1984) in a linear gravity wave model to simulate the formation and growth of tropical squall lines. The preceding results suggest gravity waves are produced by thunderstorms and boundary layer convection and that these waves may play an important role in both the evolution of the preexisting convection and in the development of new convection.

The two following chapters describe the geography of the study area and the sources and quality of the data. Chapter 4 presents three examples of squall lines that formed over Arizona and Sonora on 16-17 and 17-18 July 1984 and 2-3 August 1986. Hereafter, they are referred to as squall line 1, 2, and 3, respectively. Data obtained by satellite, both conventional imagery (visible, infrared, and enhanced infrared) and VAS (VISSR atmospheric sounder) derived fields; surface data; records of cloud-to-ground (CG) lightning strikes; and radiosonde observations (RAOBs) are used to establish that these MCSs are tropical squall lines and that they developed in an environment of relatively strong low-level shear with very weak shear aloft.

The version of Clark's model utilized in this study is described in chapter 5 as are the modifications made to this form of the model. The results of the three 2D simulations; dry, rain (R), and rain and ice (RI); are reviewed

in Chapter 6. They suggest heating of the elevated terrain in the absence of any other forcing will create an environment with pronounced low-level wind shear with weak shear aloft and create a strong low-level convergence zone over the highest terrain. These results also indicate that deep convection will erupt over the convergence zone and eventually will develop into a system which exhibits many of the features observed in squall lines 1-3 and other previously described tropical squall lines when a moisture profile representative of the precursory conditions found over southeast Arizona is inserted into the model. In addition, gravity waves will be shown to play a significant part in several episodes of discrete propagation which occurred in the mature phase of the modelled squall line. A summary and discussion of the findings are given in the last chapter.

CHAPTER 2

GEOGRAPHY

The area of interest is plotted in Figs. 4.16 and 4.18. Figure 4.18 shows more of Mexico than Fig. 4.16, the locations of the sites listed in Tables 1.1 and 4.2, and elevations above 2 km. The high terrain that extends from the lower right corner to almost the Arizona-New Mexico-Mexico border is the northernmost portion of the Sierra Madre Occidental. The southern Rocky Mountains are seen in the upper right quadrant and, in Arizona, they consist of the Mogollon Rim in the central part of the state and the White Mountains along the eastern border. In southeast Arizona several northwest-southeast trending valleys and ranges (some with peaks over 3 km) separate the Sierra Madre Occidental from the southern Rockies. The Continental Divide lies just to the east of the Arizona-New Mexico border (about 109°W) while the Sonora desert covers southwestern Arizona and western Sonora with its wide gently sloping valleys interspersed with scattered mountain ranges.

CHAPTER 3

DATA

The deserts of the southwestern United States and northwestern Mexico are some of the most sparsely populated areas of North America. Much of the western two-thirds of the Sonora desert is essentially uninhabited because of the extreme summer heat and lack of fresh water. Consequently, surface weather observations are made at a very small number of stations that are located primarily in the valleys of the region and are concentrated in and around the cities of Phoenix and Tucson. At many of these stations only high and low temperature and daily precipitation data are taken. As a result, several relatively large areas in the region are nearly void of traditional surface weather observations.

Cloud-to-ground lightning strikes obtained from the Bureau of Land Management (BLM) lightning detection network supplemented the meager surface data and were employed to help identify and track thunderstorms. Systematic errors, commonly referred to as site location errors, are present in these data and are caused by nearby metallic objects, buildings, and mountains which distort the incoming magnetic field associated with lightning strikes (Reap 1986).

As a result, an unknown number of detected lightning strikes are incorrectly located. This effect is seen in Fig. 4.16 which shows lightning strikes recorded in cloud-free areas. Two other factors, location of the direction finders and temporal gaps in the record, limited the usefulness of the BLM data. In July 1984 the southernmost direction finder was located approximately 25 km northwest of Tucson and only two were found south of 35°N. Consequently, the detection efficiency, percentage of CG strikes actually recorded, probably was less than the average 50-70% estimated by Reap (1986) for the entire BLM network. Between 1200 UTC 16 July and 0338 UTC 18 July 1984 there were eight breaks in data collection that lasted from 5 to 147 minutes. Two of these gaps were caused by power failures during the passage of squall line 1 across Tucson. No data were saved between 0338 and 1300 UTC on the 18th because of the failure of the data reception system.

Nonsurface data utilized in this project came from the radiosonde network and from satellite. The most important problem with the RAOBs in the area is missing data. Some RAOBs; such as those from Tucson, Albuquerque, and Chihuahua at 1200 UTC 17 July 1984; contain information from just the mandatory pressure levels (surface, 85, 70, 50 kPa

etc.) and a few; like Guaymus, which is on the coast about 130 km due south of Hermosillo, at 0000 UTC and Tucson at 1200 UTC 3 August 1986; do not have any upper tropospheric observations. However, the lone serious problem is the total lack of upper air data from Winslow, Arizona; El Paso, Texas; and Ely, Nevada on 2-3 August 1986 due to equipment malfunctions. Winslow is the closest upper air station to the north of the squall line area while El Paso is the nearest one to the east (upstream).

All the available visible, infrared, and VAS 6.7 μm imagery from 1245 UTC 16 July to 0000 UTC 19 July 1984 and from 1800 UTC 2 August to 1200 UTC 3 August 1986 was examined during this project. The time resolution of the visible and infrared imagery was 30 min while that of the VAS 6.7 μm imagery was 6 hrs. The 12 channel VAS data sets came from 1048-1118 UTC and 1248-1318 UTC 16 July, 1018-1048 UTC and 1618-1648 UTC 17 July, and 1018-1048 UTC 18 July 1984. VAS-derived fields; temperature, dewpoint, etc.; are subject to several potentially important sources of error. They include contamination of the sounding-field-of-view by unresolvable small clouds, lack of surface and radiosonde data with which to train the retrievals, and varying topography (Mostek et al. 1986). Earlier research by Petersen et al. (1984) and Mostek et al. (1986) noted

that VAS retrievals often could not determine the correct temperature or dewpoint at specific pressure levels but that VAS retrievals could provide accurate estimates of vertically integrated parameters like precipitable water. Thus, in this study all VAS fields were used only in cloud-free environments and, except for precipitable water, were employed only in a qualitative fashion to fill the gaps of the radiosonde network.

CHAPTER 4

THREE EXAMPLES OF TROPICAL SQUALL LINES IN ARIZONA

4.1 Life-Cycle of the Squall Lines as seen in Satellite Imagery

Satellite imagery indicated the initiation, growth, and dissipation of all three squall lines were very similar. By early afternoon scattered thunderstorms covered much of the southern Rockies and Sierra Madre Occidental with towering cumulus just beginning to form over the isolated peaks of southeast Arizona and northeast Sonora. Mid afternoon satellite images (Fig. 4.1) showed mature thunderstorms over the Rocky Mountains and Sierra Madre with strong thunderstorms rapidly developing over southeast Arizona and northeast Sonora. Subsequently, cirrus clouds from these latter thunderstorms merged while the storms in the remainder of the region weakened slightly (see Figs. 4.2 and 4.3). The squall lines all became organized during the late afternoon-early evening hours over southeast Arizona and northeast Sonora and enhanced infrared images taken at this time indicated large areas of high, very cold clouds. Satellite derived cloud top temperatures of the strongest thunderstorms of each squall line were estimated to be at least -81, -81, and -75°C, respectively which suggest maximum tops of 17-18 km. However, most

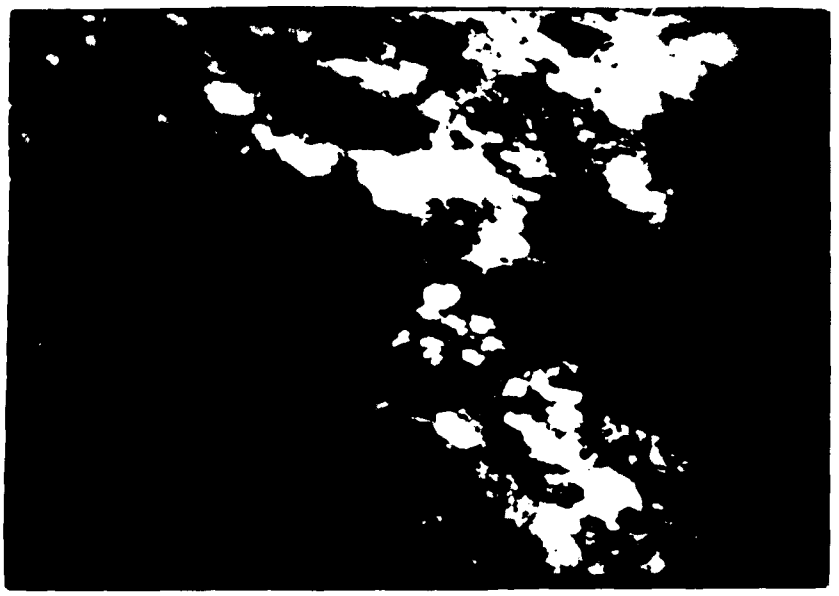

Figure 4.1 Visible image showing rapidly growing thunderstorms over southeast Arizona and northeast Sonora at 2115 UTC 16 July 1984. The resolution is 2 km.

Figure 4.2 Visible image showing strong thunderstorms over southeast Arizona and northeast Sonora at 2315 UTC 16 July 1984. Squall line 1 developed from these and other storms in the following hour and a half. The resolution is 2 km.

Figure 4.3 Enhanced infrared image of squall line 1 at 0115 UTC 17 July 1984. The resolution is 2 km, cloud top temperatures are in °C, and the enhancement curve (MB) is at the bottom of the image.

Figure 4.4 As in Figure 4.3 but from 0315 UTC 17 July 1984.

thunderstorms reached altitudes of 14-16 km. These estimated cloud tops are almost identical to those calculated by Houze (1977) for a GATE tropical squall line, Leary and Rappaport (1987) for a Texas MCC that developed from a squall line, Smull and Houze (1985) for an Oklahoma squall line, and Heymsfield and Schotz (1985) for a different Oklahoma squall line.

Late afternoon-early evening images of squall lines 1 and 2 also indicated cirrus clouds were advected to the west of the initial thunderstorms so that part of the upper level outflow was ahead of these systems before they developed into tropical squall lines (much more so with 1 than 2). Late evening imagery (Figs. 4.4, 4.5, and 4.6) showed the squall lines propagating basically from east to west across southern Arizona and northern Sonora. Elsewhere, thunderstorms were quickly dissipating at sunset. The anvil cloud systems reached maximum extent between 0400 and 0700 UTC (i.e., before midnight local time), and as they expanded westward, the eastern edge (upstream) remained nearly stationary over the Continental Divide. During this period, strong thunderstorms occasionally developed at the periphery of the anvil clouds. The most intense ones, with satellite-derived cloud top temperatures $\leq$ -75°C, formed near Douglas (DOU), Arizona and Hermosillo (HMO), Sonora;

Figure 4.5 As in Figure 4.3 but of squall line 2 at 0245 UTC 18 July 1984.

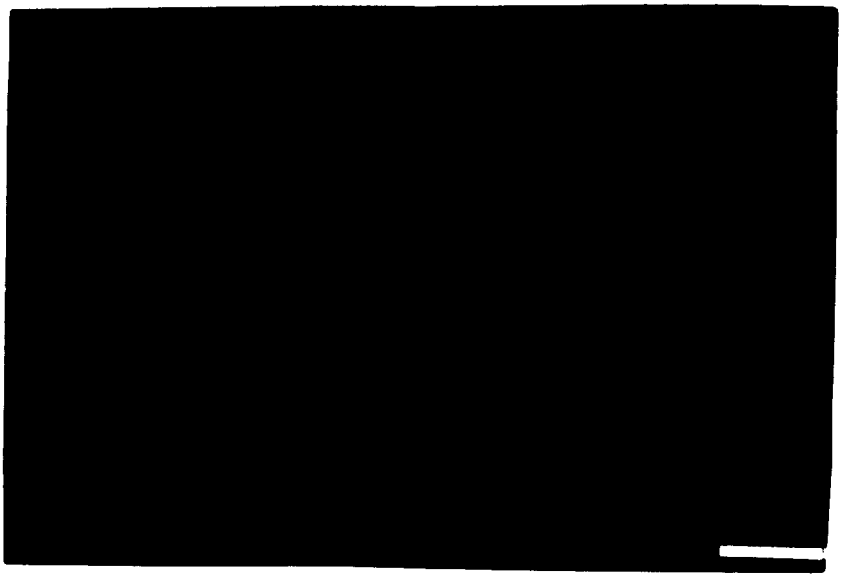

Figure 4.6 As in Figure 4.3 but of squall line 3 at 0300 UTC 3 August 1986.

over the Phoenix (PHX) metropolitan area; and south of Douglas in association with the anvil cloud systems of squall lines 1, 2, and 3, respectively. Thunderstorms continued developing along the leading edge of the anvil clouds until about 0700 UTC when weakening began. The southern parts of the squall lines rapidly dissipated as they neared the Gulf of California and the northern portions dissipated soon thereafter so that by 1000 UTC the squall line systems had essentially ceased to exist.

Visible and infrared images taken after the three squall lines had dissipated revealed cirrus clouds moving anticyclonically above a midlevel cyclonic circulation, a feature previously described in both tropical and midlatitude MCSs. For example, Houze (1977) found a small-scale cyclonic circulation at 70 kPa in the trailing anvil region of a tropical squall line while Leary (1979) observed one in a tropical cloud cluster. Gamache and Houze (1982, 1985) and Houze and Rappaport (1984) also showed a midlevel cyclonic circulation in two different GATE squall lines. In addition, Johnston (1982) described cyclonically rotating features, which he referred to as mesoscale vorticity centers (MVCs), that form at heights of 2.5-4.5 km within MCCs in the central United States and Smull and Houze (1985) detected a cyclonic vortex in the region of strati-

form rain behind an Oklahoma squall line. Leary and Rappaport (1987) also observed a midlevel cyclonic circulation with radar in a west Texas MCC that developed from a squall line.

The midlevel cyclonic circulation or MVC associated with squall line 1 is shown in Figs. 4.7-9 while the one from squall line 2 can be seen in Fig. 4.10. The wind barbs and axes of the cloud bands in these figures have been plotted in Figs. 4.11-14. The patterns of spiralling cloud bands in Figs. 4.7-14 are very similar to the low-level reflectivity patterns in figures 25 and 30 of Leary and Rappaport (1987) which show the rainbands to the rear of their squall line. Both systems were advected to the west-northwest by the midtropospheric winds at velocities of about 6 and 5.5 m s^{-1} and initiated thunderstorms as they moved across the mountains of southern California and northern Baja California during the afternoon.

An estimate of the average relative vorticity of these features was made using the midlevel (60-45 kPa) cloud drift winds determined from the McIDAS (Man Computer Interactive Data Access System) single pixel method (McIDAS Reference Manual 1987). In this method individual cloud elements are subjectively followed in a sequence of three visible and infrared images to obtain the mean wind vector.

Figure 4.7 Visible image showing the remains of squall line 1 at 1715 UTC 17 July 1984. The wind barbs are cloud drift winds (long = 5 m s^{-1}, short = 2.5 m s^{-1}) and the resolution is 2 km.

Figure 4.8 As in Figure 4.7 but from 1915 UTC 17 July 1984.

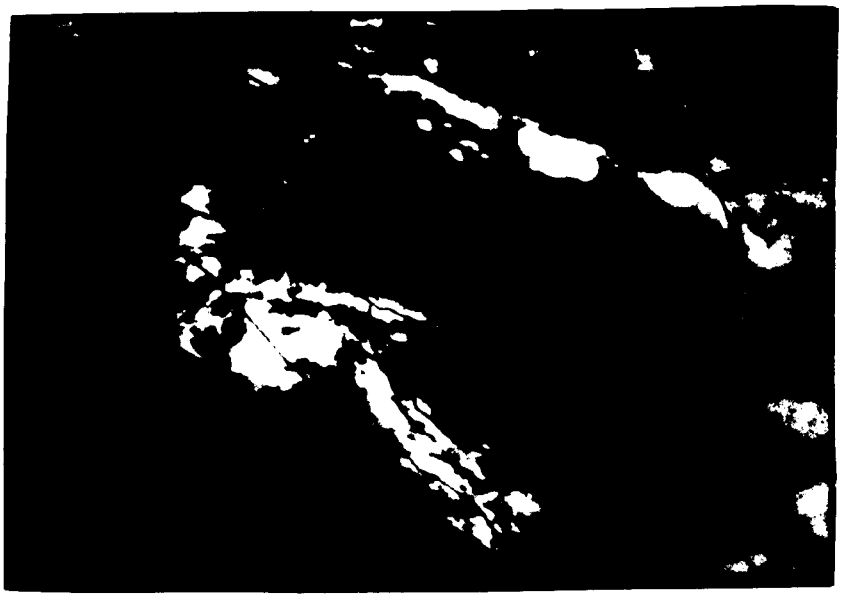

Figure 4.9 As in Figure 4.7 but from 2115 UTC 17 July 1984.

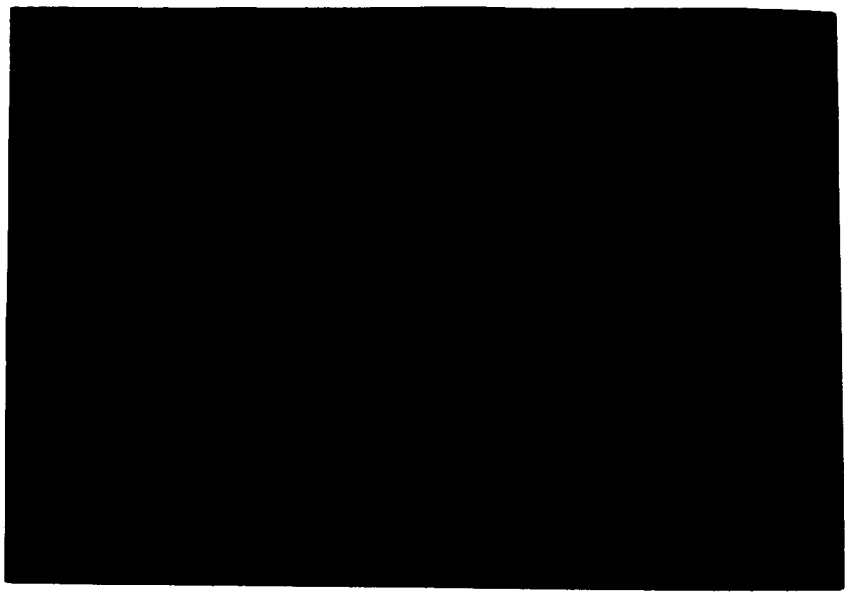

Figure 4.10 As in Figure 4.7 but of squall line 2 at 1615 UTC 18 July 1984.

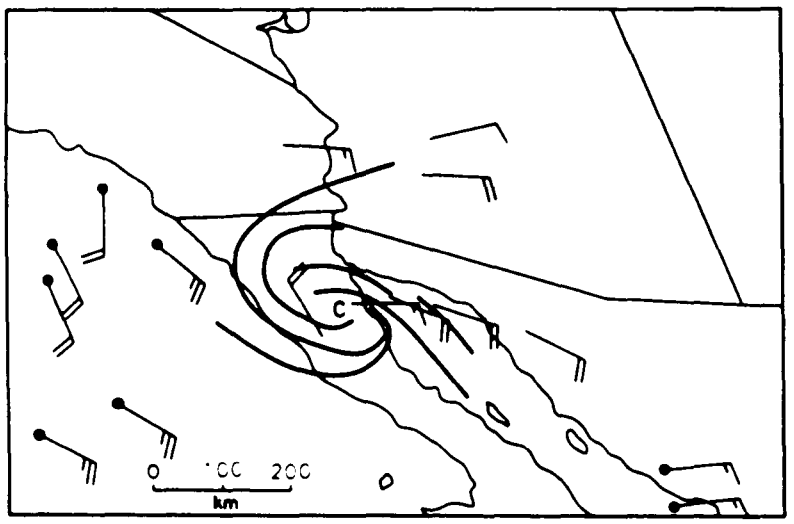

Figure 4.11 Cloud drift winds taken from the image in Figure 4.7. Midlevel, 60-45 kPa, and high level, 35-20 kPa, winds (the barbs with the dot at the end) are plotted and the long = 5 m s^{-1} and the short = 2.5 m s^{-1}. C marks the center of rotation of the cyclonic circulation and the thick solid lines are the axes of the cloud bands seen in Figure 4.7.

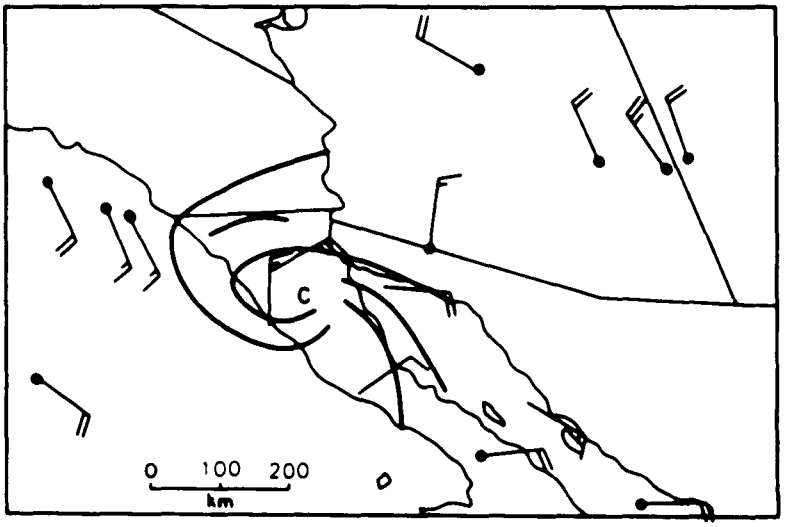

Figure 4.12 As in Figure 4.11 but from the image in Figure 4.8.

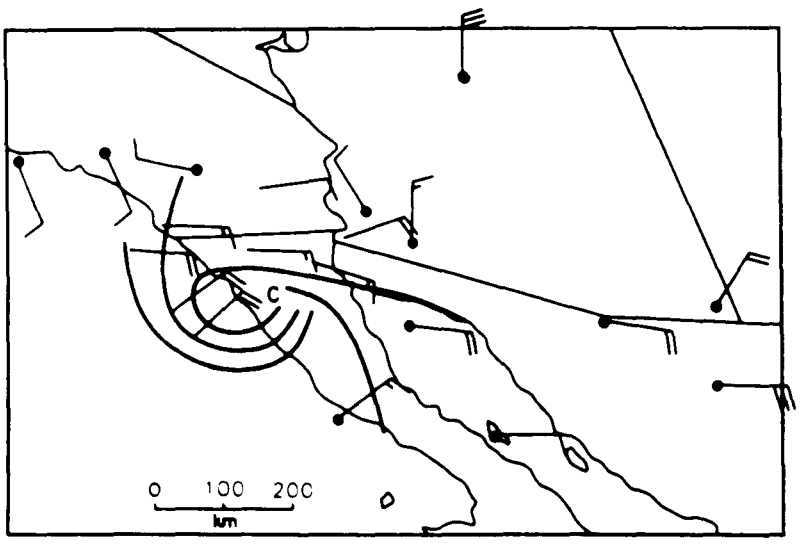

Figure 4.13 As in Figure 4.11 but from the image in Figure 4.9.

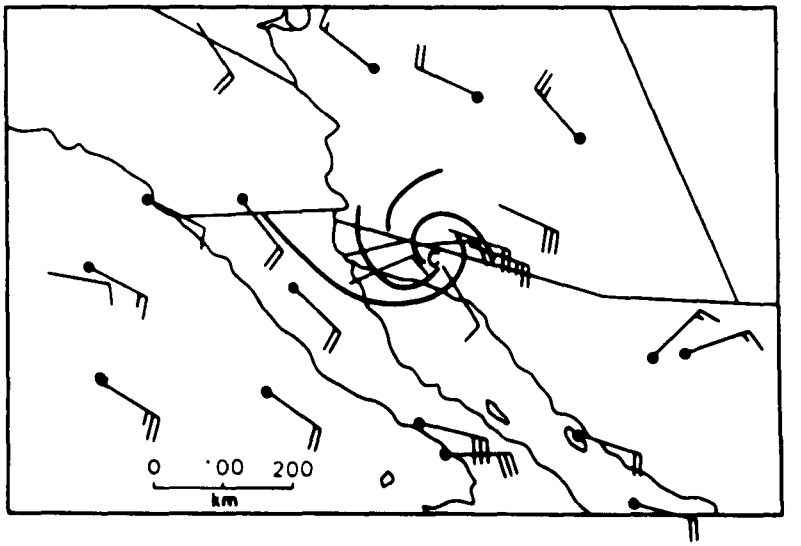

Figure 4.14 As in Figure 4.11 but from the image in Figure 4.10.

After the wind vectors were determined they were interpolated onto a circle 125 km in radius located at the C, the center of circulation, in Figs. 4.11-14. The average relative vorticity was calculated by computing the circulation around the circle and dividing by the area. The average relative vorticity of the first system was approximately 5 X 10^{-5} s^{-1} and the second about 4 X 10^{-5} s^{-1}. For comparison, the average relative vorticity (over a circle 125 km in radius) of Hurricane Anita on 2 September 1977 at an altitude of 3012 m was approximately 40 X 10^{-5} s^{-1} (Sheets 1979) and the earth vorticity ($f = 2\Omega\sin\phi$) at 31°N is 7.5 X 10^{-5} s^{-1}.

Anticyclonic flow aloft was clearly observed above all three systems when the satellite images were looped and has been noted earlier in tropical MCSs by Houze (1977), Leary (1979), Houze and Rappaport (1984), and Gamache and Houze (1985) and in midlatitude MCCs by Fritsch and Maddox (1981) and Wetzel et al. (1983). The average upper tropospheric relative vorticity associated with the remnants of squall line 1 (Fig. 4.9) and 2 (Fig. 4.10) was estimated after interpolating the upper-level winds onto a circle centered at the C in Figs. 4.13 and 4.14, respectively. The vorticity was about -4 X 10^{-5} s^{-1} and is comparable to the -3.9 X 10^{-5} s^{-1} value obtained by Leary (1979).

20 kPa divergence obtained from the RAOBs of 1200 UTC 17 and 18 July 1984 was a maximum, 2.0 X 10^{-5} s^{-1} and 1.5 X 10^{-5} s^{-1} respectively, above the remains of squall lines 1 and 2. These values are slightly less than those calculated for other tropical convective systems by Houze (1977), 2.9 X 10^{-5} s^{-1}, and by Leary (1979), 2.4 X 10^{-5} s^{-1}. In contrast, they are significantly smaller than the values, 10 X 10^{-5} s^{-1}, reported by Wetzel et al. (1983) for two Midwest MCCs and almost an order of magnitude less than the divergence, 15.0 X 10^{-5} s^{-1}, computed for a composite of 10 midlatitude MCCs by Fritsch and Maddox (1981). Possible reasons for the near order of magnitude difference are the paucity of radiosonde observations in this area and the fact that all three squall lines here had essentially dissipated by 1000 UTC while 7 of the 10 MCCs studied by Fritsch and Maddox (1981) did not even reach maximum extent until after 0830 UTC.

4.2 Surface Observations

Traditional surface observations; temperature, wind speed and direction, pressure, precipitation, etc.; corroborate the information obtained from satellite imagery. The data showed that all three systems exhibited features typically associated with tropical squall lines. They included a strong gust front at the surface; a narrow band

of intense convection, the squall line, which caused a brief period of heavy precipitation; and a trailing region of light rain which lasted for several hours and fell from relatively high-based clouds.

The passage of the squall lines across Tucson was recorded at the University of Arizona and the wind speed and direction measurements are presented in Fig. 4.15. The left hand side of all three plots shows the normal late afternoon-early evening wind conditions in Tucson, i.e., generally upslope northwest winds. The winds shifted from west or northwest to the northeast or east as the gust fronts moved past. Severe thunderstorms associated with squall line 1 produced two short-lived tornadoes and caused significant wind damage over a large part of Tucson as straight line winds reached 29 m s^{-1} (Fig. 4.15a) at the university before the anemometer failed. The equivalent potential temperature (θ_e) of the air in this downburst was estimated to be 332°K and suggests the air originated approximately 4.5 km above the surface. Wind gusts of squall line 2 reached at least 25 m s^{-1} in east Tucson but only about 14 m s^{-1} at the university (Fig. 4.15b) while the third produced 24 m s^{-1} winds (Fig. 4.15c). Wind gusts from the strongest thunderstorms, which satellite imagery suggests were to the south of Tucson in all three cases,

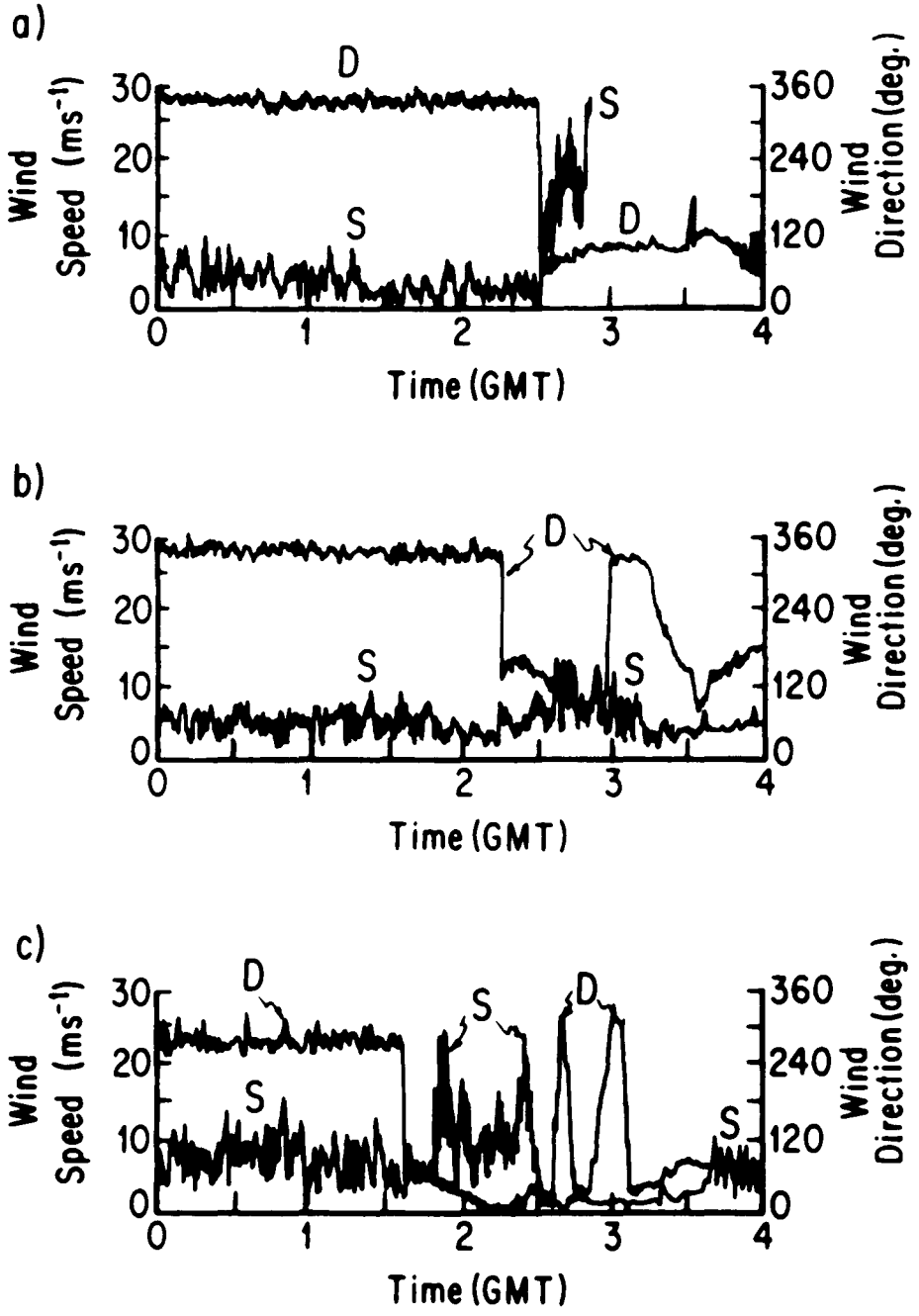

Figure 4.15 Wind speed (S) and direction (D) recorded at the University of Arizona during the passage of three tropical squall lines on (a) 17 and (b) 18 July 1984 and (c) 3 August 1986.

may have been significantly greater than those recorded in Tucson. These winds are much stronger than the 12-15.4 m s^{-1} winds reported by Zipser (1969), Miller and Betts (1977), Houze (1977), and Chong et al. (1987) for squall lines in the tropics and are comparable to the gusts frequently observed in the central United States. Temperature and pressure changes associated with these three gust fronts are also notably higher than those reported in the tropics. For instance, in the hour following the arrival of the gust fronts, the temperature declined 11-15°C as the pressure rose 0.4-0.5 kPa. Houze (1977) and Chong et al. (1987), who measured a pressure rise of only about 0.2 kPa, both reported temperature decreases of just 4°C.

Southeast Arizona most likely experienced stronger winds than the tropics because the low θ_e, potentially cold air aloft (look ahead to Figs. 4.21-23) which comprised the intense downdrafts not only descended significant distances, 4-5 km, to reach the surface of the desert but also fell through much thicker layers of unsaturated subcloud air. The lifting condensation levels (LCLs) above Tucson were approximately 2.3-2.8 km above the ground and were far higher than the LCLs in the tropics where Chong et al. (1987) and Barnes and Sieckman (1984) reported they were just 0.8 and 0.45 km above the surface, respectively. The

higher LCLs above Tucson were the result of lower relative humidities which arose from the combination of higher temperatures and lower absolute humidities. Consequently, a large fraction of the falling hydrometeors melted and/or evaporated before reaching the desert surface to generate downbursts that produced larger temperature and pressure perturbations and higher wind gusts.

The present weather conditions and hourly rainfall observed at the Tucson National Weather Service office (WSO) from 0000-0900 UTC 17 and 18 July 1984 and 3 August 1986 are listed in Table 4.1 and several noteworthy features are apparent. One is that each of the squall lines propagated over Tucson at about the same time of day and another is that thunder continued for 2-4 hours after the squall lines left the city. A third notable feature is that no heavy rain fell at Tucson WSO in connection with any of the systems. However, heavy rains were observed a few kilometers to the north and south. The total precipitation recorded at several stations in southeast Arizona from the three squall lines and their trailing anvil clouds is listed in Table 4.2. The University of Arizona is only 13 km north of Tucson WSO and received significantly more rain than Tucson WSO in all three cases. The large variation in precipitation over relatively short distances

Table 4.1 Present Weather and Hourly Rainfall (mm) at Tucson WSO.

Time (UTC)	00	01	02	03	04	05	06	07	08	09
I: weather			T	T	——	TRW	TRW	TRW⁻	TRW⁻	
rain	0	0	0	1.8	3.0	3.6	0.7	T	0	0
II: weather					TRW⁻	TRW⁻	TRW⁻	TRW	RW⁻	RW⁻
rain	0	0	0	1.0	1.5	2.0	3.0	2.5	1.8	T
III: weather				T	TRW⁻	TRW⁻	RW⁻	——	RW⁻	
rain	0	0	0	T	T	T	T	T	T	0

—— = missing data
I = 17 July 1984
II = 18 July 1984
III = 3 August 1986

TABLE 4.2 Total Precipitation (mm) at Selected Stations in Arizona from three Tropical Squall Lines

Station		I	II	III
Arivaca 1 E	(ARI)	48.3	32.0	16.5
Douglas	(DOU)	5.1	5.6	12.7
Kitt Peak	(KTP)	11.7	31.8	14.5
Redington	(RED)	39.4	77.5	21.6
Tucson WSO	(TUS)	9.1	11.9	T
Tucson U. of Az.*		18.5	25.4	11.4
Tucson**		8.9	11.2	14.7

* ~ 13 km north of TUS
** ~ 8 km due west of TUS
I = 16-17 July 1984
II = 17-18 July 1984
III = 2-3 August 1986

reflects the nature of the squall lines. Visual observations and the CG lightning strike data (discussed in the following section) revealed they are made up of distinct clusters of strong to severe thunderstorms separated by areas of much weaker or no convection. Furthermore, the squall lines appeared to move by discrete propagation as discussed by Houze (1977) whereby new thunderstorms or line elements would begin forming ahead of the line, develop rapidly as the line approached, reach maximum intensity as the line moved past, and then weaken behind the line eventually becoming part of the trailing anvil cloud.

Light rain which fell from the anvil cloud at rates of 0.7-3.6 mm h^{-1} and lasted from 4-6 hours accounted for almost all of the precipitation received at Tucson WSO with squall lines 1 and 2. The rain began around one-half hour after the passage of the gust fronts. Only a trace amount of rain was observed in association with squall line 3 because Tucson was on the northern edge of the anvil cloud as seen in Fig. 4.6. However, Douglas which was near the eastern edge of the anvil cloud reported that rain fell at an average rate of 2.5 mm h^{-1} for 5 hours. These rainfall rates are similar to the 1-10 mm h^{-1} rates observed in other tropical and midlatitude convective systems by numerous researchers; e.g., Zipser (1969), Leary and Houze

(1979b), Ogura and Liou (1980), Chong et al. (1987), and Johnson and Hamilton (1988). Zipser (1977), Kessinger et al. (1987), and Leary and Rappaport (1987) also observed light rain to the rear of squall lines.

Maximum reported precipitation for the three systems ranged from 22.9-77.5 mm with the latter amount from Redington (RED) equal to 104% of the average July precipitation. The combined total at Redington from squall lines 1 and 2 was 35% of the average annual precipitation. Heavy rainfall also was observed in association with thunderstorms that formed at the periphery of the anvil clouds. A cluster of thunderstorms that developed at the northern edge of the anvil cloud of squall line 2 left up to 63.5 mm of rain in the Phoenix metropolitan area where the normal annual rainfall is just 175-225 mm. Thus, these systems are capable of producing not only a significant fraction of the summer monsoon rainfall but also an important part of the annual precipitation. Similarly, Fritsch et al. (1986) found that over much of the central United States MCSs cause 30-70% of the warm season, April-September, precipitation and an even higher percentage during the summer. An analysis by Kane et al. (1987) of 74 MCCs which formed east of the Rocky Mountains indicated the "typical" MCC generated an average rainfall of 16.1 mm and that every MCC

produced a maximum of at least 26 mm and most more than 75 mm. Precipitation data listed in Table 4.2 and from other locations in southeast Arizona suggest the three squall line/anvil cloud systems produced an average rain depth close to that of the MCCs studied by Kane et al. (1987). Maximum reported precipitation was less than that commonly measured with the MCCs but this may be due to the lack of data from the mountains, especially the Sierra Madre Occidental, which normally receive the greatest amounts of rain.

4.3 Cloud-to-Ground Lightning Strike Data

Records of CG lightning strikes from the BLM network were used primarily to identify thunderstorms and to locate squall lines 1 and 2 in areas devoid of surface observations. The lightning data also indicated the squall lines were composed of distinct clusters of thunderstorms separated by much weaker convection. This can be seen in Figs. 4.16 and 4.17 which show the positions of approximately 2500 and 750 CG strikes recorded between 0100-0200 UTC and 0500-0600 UTC respectively on 17 July 1984. Figure 4.16 indicates that at 0200 UTC the northern part of squall line 1 was composed of one large and two smaller mesoβ-scale (see Orlanski 1975) clusters of thunderstorms and that the southern part was composed of at least two large clusters,

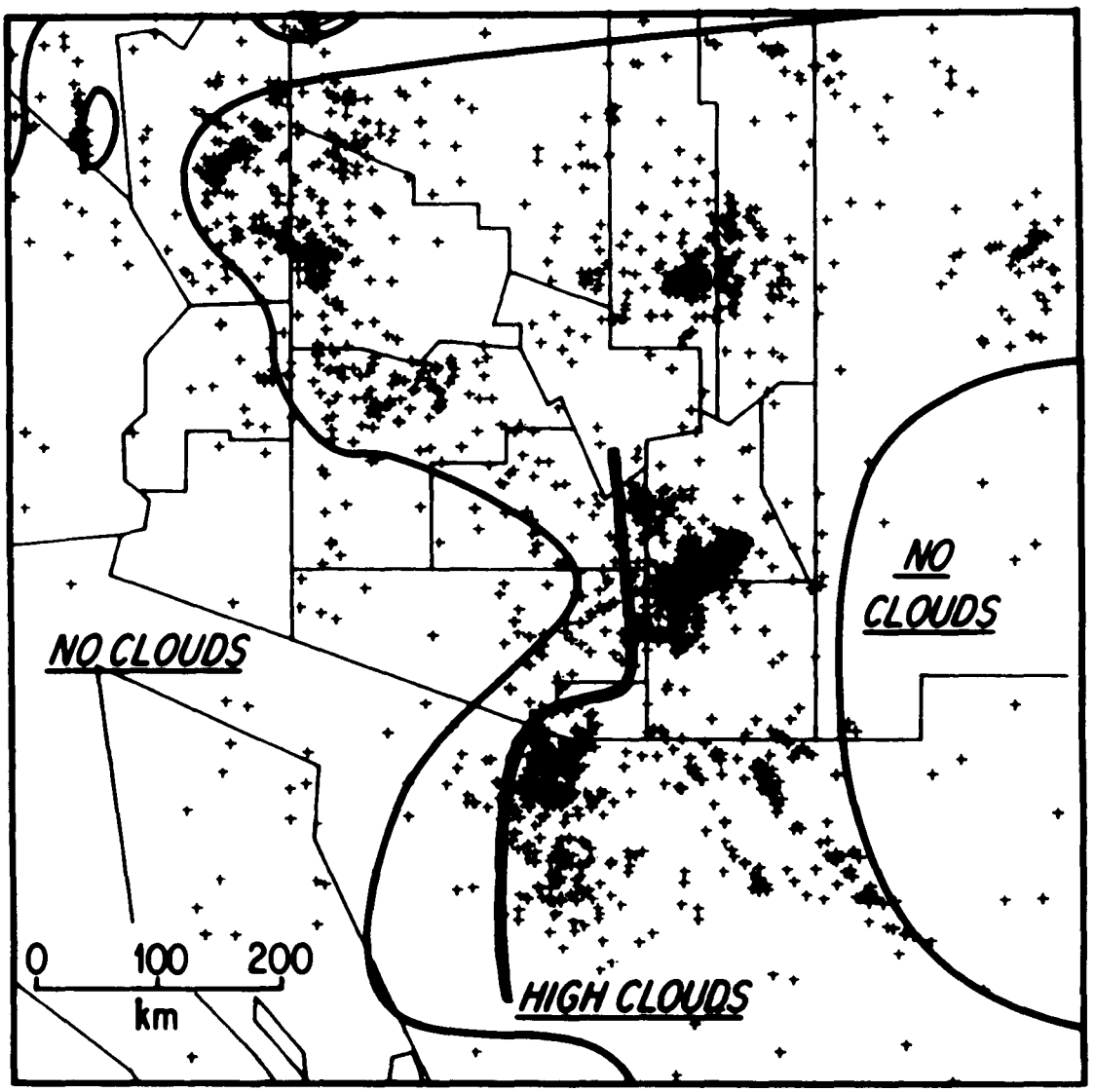

Figure 4.16 Cloud-to-ground lightning strikes and nephanalysis of squall line 1 for 0100-0200 UTC 17 July 1984. The figure shows most of Arizona, including all the counties; western New Mexico; southernmost Nevada; southeastern California; the northern end of the Gulf of California; and northwestern Mexico including parts of three states (their borders are not on the figure): northern Sonora, northeastern Baja California, and northwestern Chihuahua. The thick solid line shows the position of the squall line at 0200.

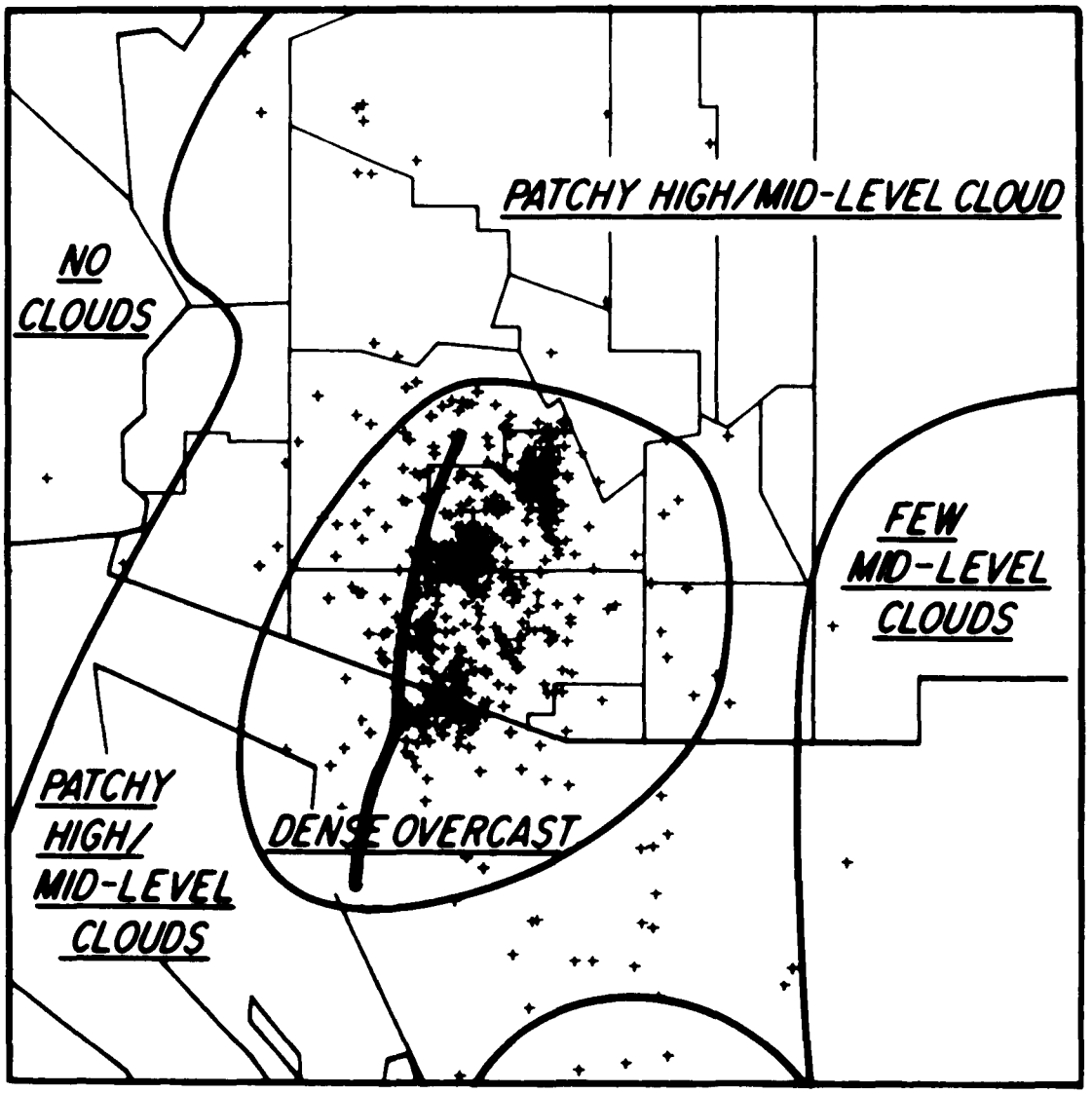

Figure 4.17 As in Figure 4.16 but for 0500-0600 UTC 17 July 1984. The thick solid line shows the position of the squall line at 0600.

one along and to the south of the Arizona-Sonora border which was moderately well sampled by the BLM network and one further south which was poorly sampled.

About 1100 CG discharges were recorded from 0100 to 0200 UTC in the vicinity of the squall line system and if a detection efficiency of 50% is assumed for the system as a whole, the average discharge rate during this period may have been nearly 37 min^{-1}. More than 1000 CG strikes were recorded in each of the following three hours with the maximum of 1250 detected between 0400 and 0500 UTC when the peak rate was 28 min^{-1}. These rates of CG lightning strikes are comparable to those reported by Rutledge and MacGorman (1988) and by Goodman and MacGorman (1986) who studied 10 MCCs in the southern Great Plains. They found the average MCC produced CG strokes at a rate of more than 1000 h^{-1} for 9 successive hours and that the average peak rate was 42 min^{-1} but sometimes was greater than 60 min^{-1}. The locations of the CG discharges observed from 0500 to 0600 UTC are plotted in Fig. 4.17 which shows the squall line was comprised of at least three large clusters of thunderstorms with another forming in between and slightly ahead of the two southern ones. The clusters appeared to have a lifetime of about 2-3 hours.

Besides the 1100 CG discharges associated with the squall line system shown in the bottom half of Fig. 4.16, more than 1300 were recorded elsewhere, mostly over the mountains of northern Arizona and northwestern New Mexico. Satellite imagery and the data presented in Fig. 4.17 imply nearly all of the thunderstorms in the aforementioned areas had dissipated by 0500 when the squall line was still very active. The figure also reveals that CG strikes occurred at significant distances behind the squall line. Lightning and thunder were observed in Tucson (see Table 4.1) when squall lines 1 and 2 were approximately 100 km west of the city. Krehbiel (1986) stated that horizontal discharges of lightning between propagating thunderstorms and the trailing region of light rain have been observed to travel 50-100 km and that they sometimes produce a positive CG stroke. In addition, since the lightning typically happens every few minutes a slow charging process might be continuously creating the positive charge which may be related to either the production and/or fall of snow that melts before reaching the surface to form light rain. In contrast, Rutledge and MacGorman (1988) concluded the positive CG strikes recorded in the MCS they studied probably resulted from the accumulation of small, positively-charged ice particles in the upper regions of the squall line thun-

derstorms which then became incorporated into the trailing anvil cloud as the squall line propagated away. However, they also stated the generation of positive charge in the anvil cloud may be important.

Plots of the lightning data collected during the formation and growth of squall line 2 were very similar to those of the first. For example, a plot of the CG discharges from 0200-0300 UTC showed squall line 2 was composed of at least three large, mesoβ-scale groups of thunderstorms, two in Arizona and one in Sonora, and one small group which was developing approximately 30 km ahead of the line over the Arizona-Sonora border. The tendency for new clusters of thunderstorms to form ahead of both squall lines 1 and 2 was noted many times and when combined with the surface observations strongly suggests the squall lines moved by discrete propagation. Individual clusters again seemed to form, mature, and dissipate in less than 3 hours. Thunderstorms over the mountains of northern Arizona and northwestern New Mexico dramatically weakened after 0200 UTC so that less than 20 CG lightning strikes were recorded there in the half-hour prior to the loss of data while more than 625 were detected in the squall line.

All three mesoα-scale (see Orlanski 1975) squall line systems developed from mesoβ-scale clusters of thunderstorms

that originated over the mountains of southeast Arizona and northwest Mexico. Furthermore, at any given moment the squall lines were composed of several distinct mesoβ clusters of thunderstorms as shown in Figs. 4.16 and 4.17. After a detailed examination of several long-lived Great Plains MCCs, Cotton et al. (1983) and Wetzel et al. (1983) also found that many of their mesoα-scale MCCs formed from mesoβ-scale systems of thunderstorms whose initial development was over the Rocky Mountains.

Without lightning data the location of squall line 1 could not have been accurately determined at any time outside southeast Arizona because part of the anvil cloud system spread to the west (ahead) of the squall line in a region with no surface observations. Squall lines 2 and 3 were much easier to locate as very little of the anvil cloud system was ahead of either one. All available surface observations, lightning data, and satellite images were utilized to estimate the positions of the three squall lines drawn in Figs. 4.18-20. The dashed lines represent areas where the convection was very weak or nonexistent.

Squall lines 1 and 2 propagated east to west, from 90°, while 3 propagated east-northeast to west-southwest, from about 70°. The average propagation velocity of all three was estimated to be 12 ± 1 m s^{-1} which in each case was

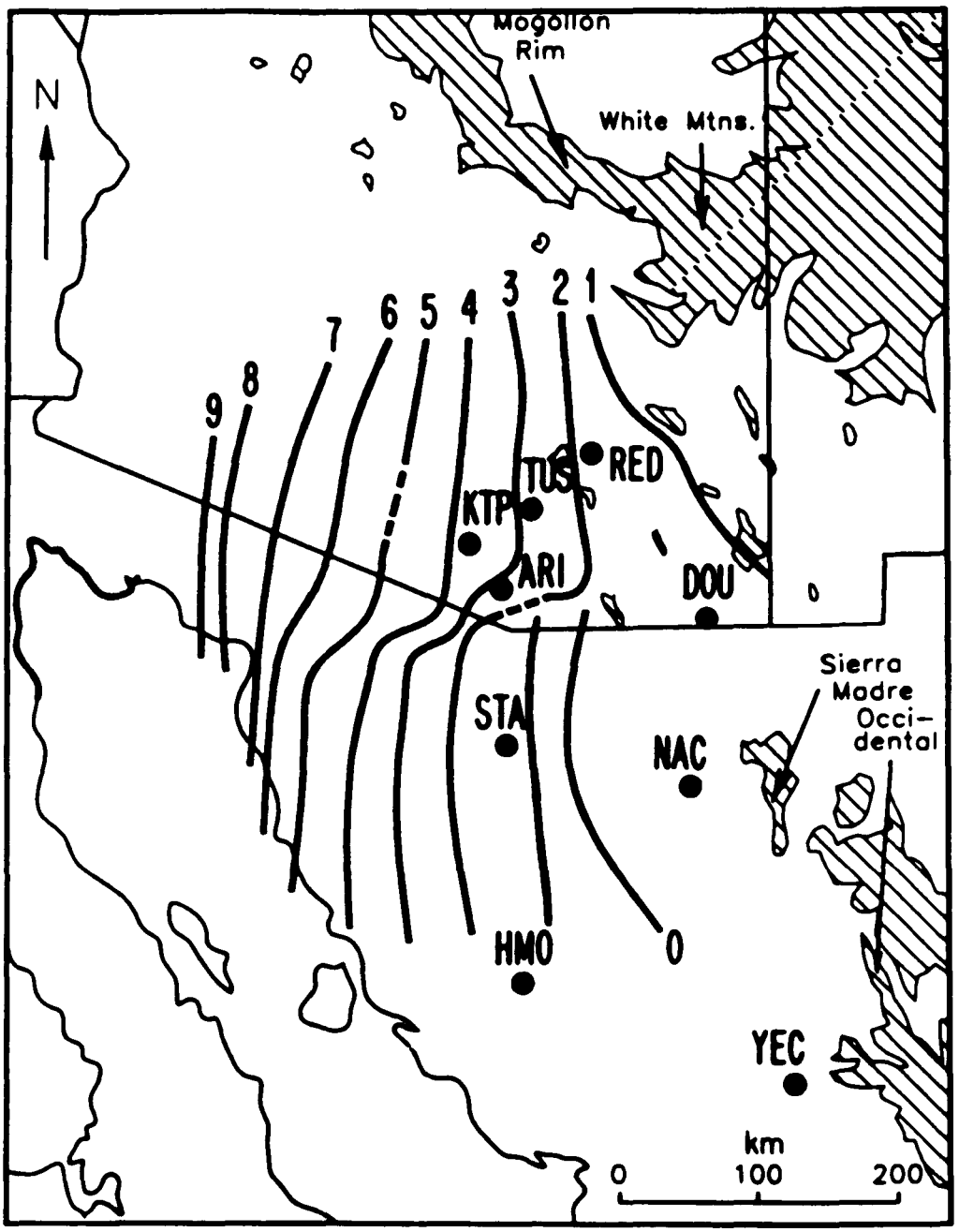

Figure 4.18 Isochrones marking the locations of the tropical squall line of 16-17 July 1984. Dashed lines denote areas with little or no convection. The stations plotted are listed in Table 1.1 and areas above 2 km are outlined.

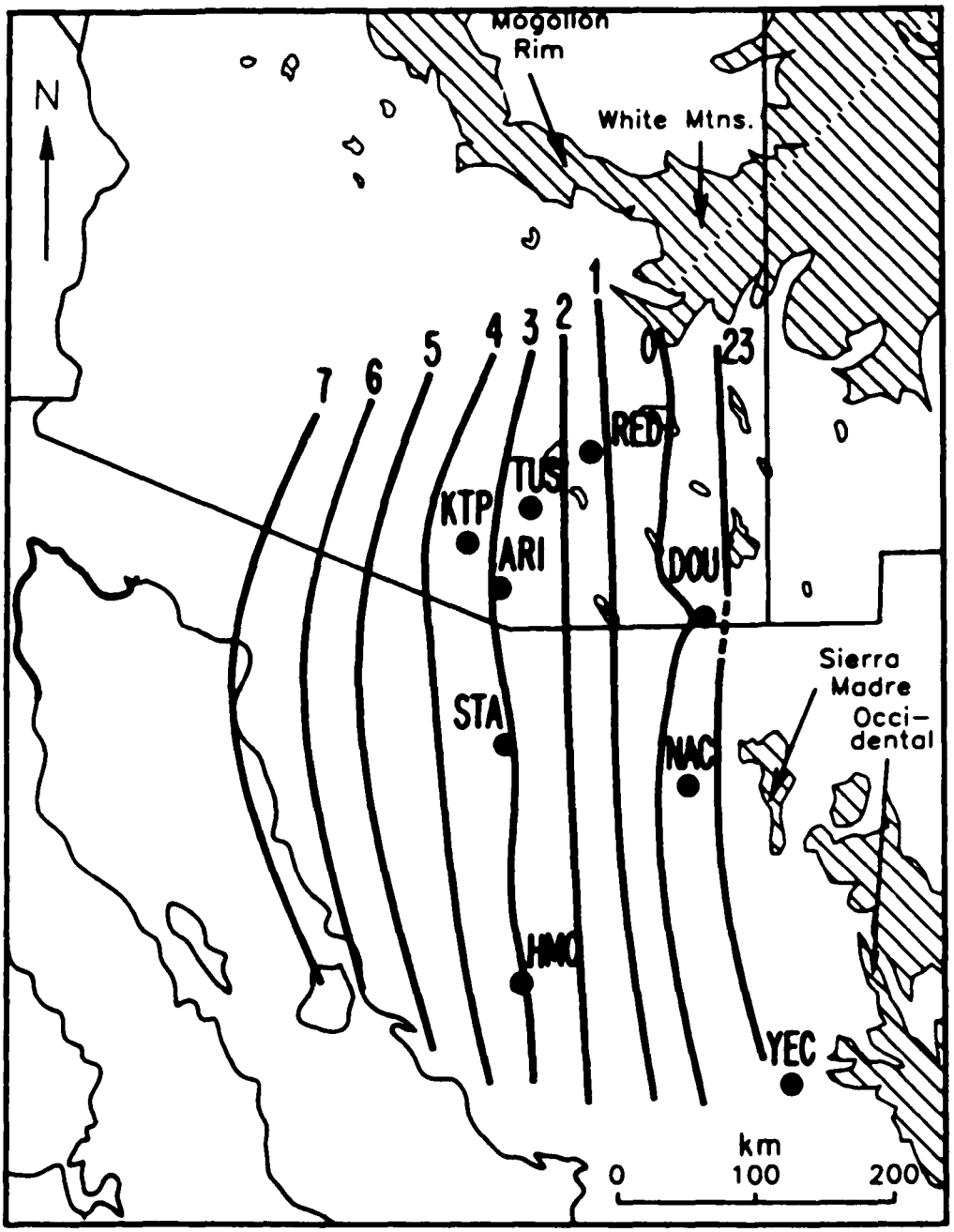

Figure 4.19 As in Figure 4.18 but for the tropical squall line of 17-18 July 1984.

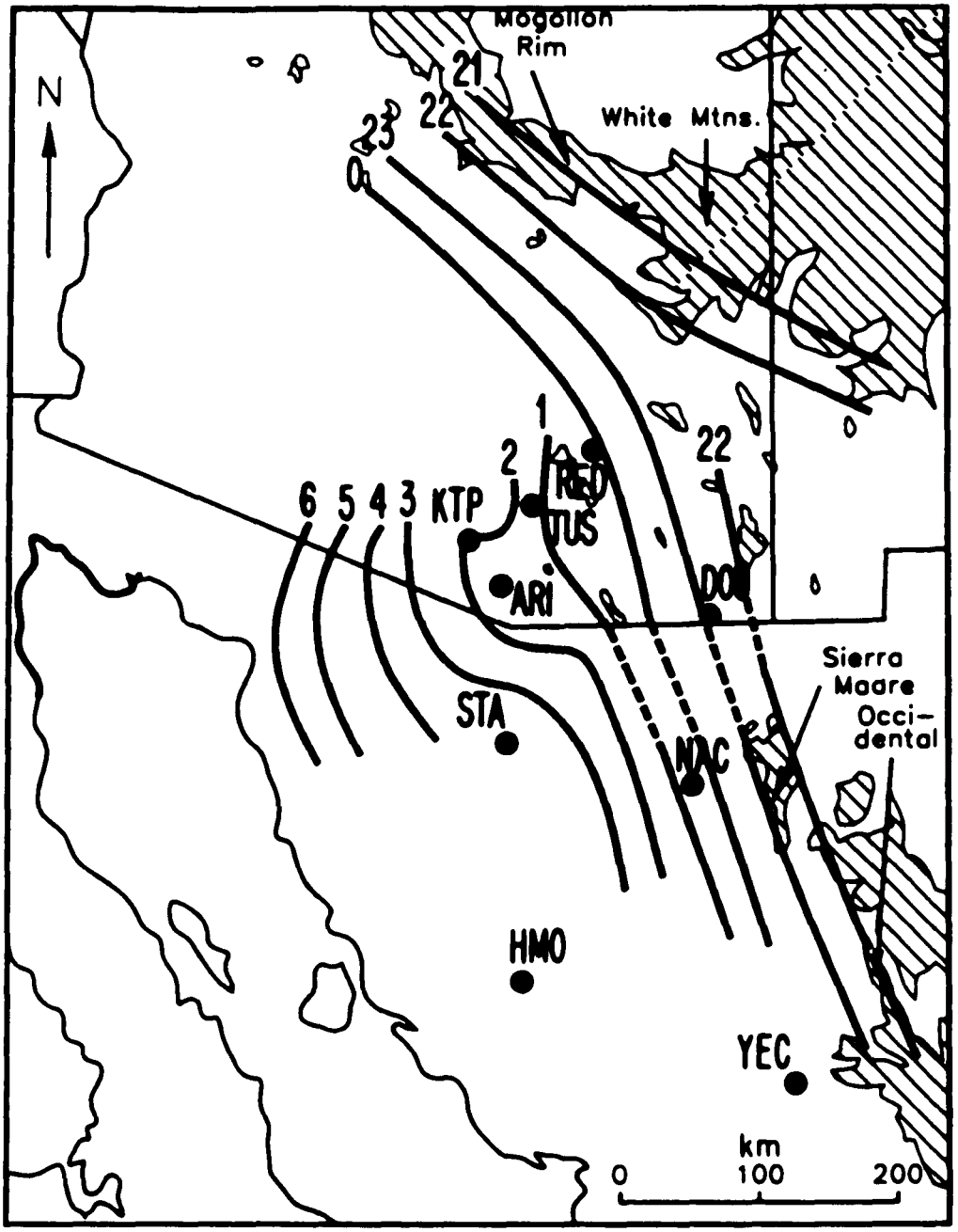

Figure 4.20 As in Figure 4.18 but for the tropical squall line of 2-3 August 1986.

greater than the environmental flow at all levels below 20 kPa. This velocity also is comparable to the mean propagation speeds, some of which are listed in Table 4.3, previously determined for squall lines in both the tropics and midlatitudes.

4.4 Tucson Weather Service Office Radiosonde Observations

The 0000 UTC 17 and 18 July 1984 and 3 August 1986 Tucson WSO RAOBs were made just prior to the arrival of the squall lines and skew T-log P plots of the data can be seen in Figs. 4.21-23. The soundings indicate similar conditions prevailed ahead of the squall lines. Boundary layer winds (surface to 75 kPa) were from the west to northwest at 3-8 m s^{-1} while midtropospheric winds (75 to 30 kPa) blew from the east-northeast to southeast at 5-10 m s^{-1}. The maximum midtropospheric speeds were 8.0-10.0 m s^{-1} near 55 kPa. Upper tropospheric winds (30 to around 11 kPa) before squall lines 1 and 2 were predominantly out of the east at 7-12 m s^{-1} but ahead of the third they were from the northwest at 3-8 m s^{-1}.

Comparing the direction of propagation and average propagation velocity of each squall line with the corresponding Tucson WSO wind direction and speed data indicates front-to-rear flow ahead of each system from the surface to 20 kPa (at least in southeast Arizona) and to the

TABLE 4.3 Mean Propagation Velocity (m s^{-1}) of Some Tropical Squall Lines

Location	Date/s		V
Arizona	17,18 July 1984; 3 Aug. 1986		12 ± 1
Eastern Atlantic[a]	4,11,12,16 Sept.	1974	11.8
Eastern Atlantic[b]	28 June, 13 Aug., 12 Sept.	1974	11.1
Venezuela[c]	June-Sept.	1972	14.5
West Africa[d]	22 June	1981	14.5
Caribbean Sea[e]	18 August	1968	14.4
Central Pacific[f]	31 March-1 April	1967	15.0
Oklahoma[g]	22 May	1976	13.9
Texas[h]	8 June	1980	11.5

a - Mansfield (1977)
b - Barnes and Sieckman (1984)
c - average of 6 squall lines from Betts et al. (1976)
d - Chong et al. (1987
e - average of northern and southern portions of squall line from Zipser (1977)
f - Zipser (1969)
g - Ogura and Liou (1980)
h - Leary and Rappaport (1987)

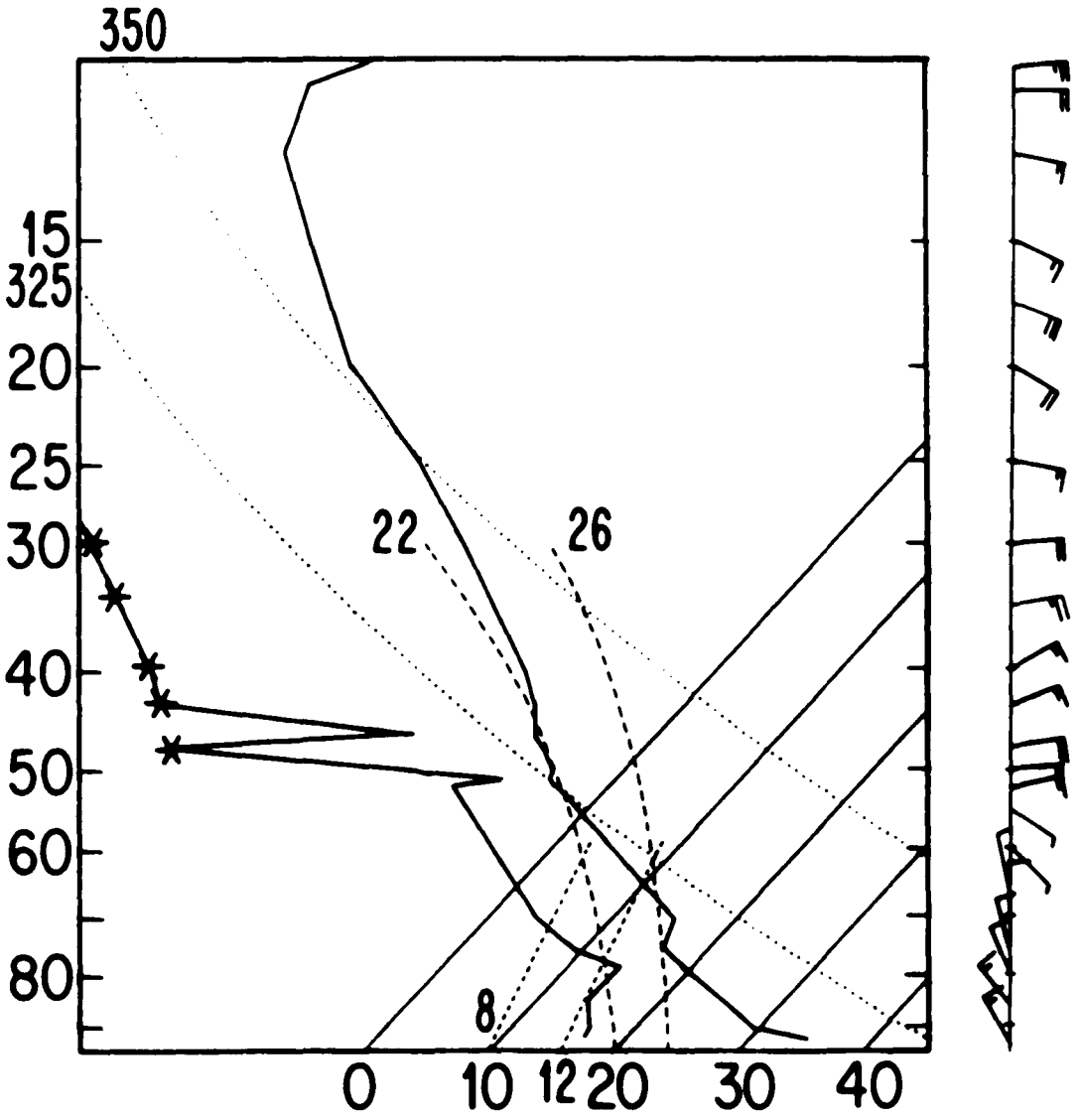

Figure 4.21 Skew T-log P plot of the 0000 UTC Tucson WSO sounding of 17 July 1984. Isotherms and moist adiabats are in °C, dry adiabats in °K, saturation mixing ratio in g kg^{-1}, pressure in kPa, and wind speed in m s^{-1} (long barb = 5 m s^{-1}, short barb = 2.5 m s^{-1}). Dew-point depressions ≥ 30°C are indicated by an *.

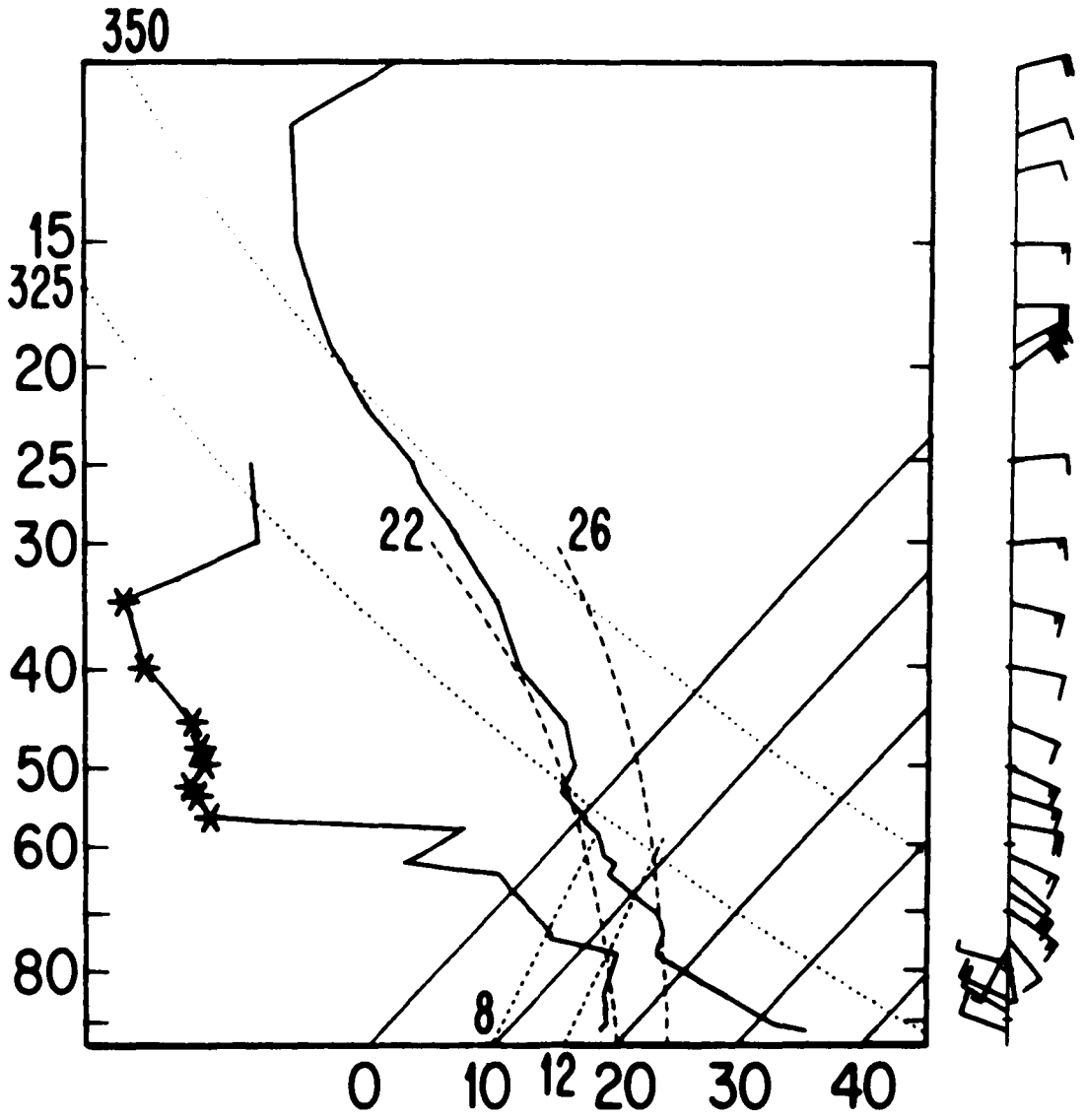

Figure 4.22 As in Figure 4.21 but for 18 July 1984.

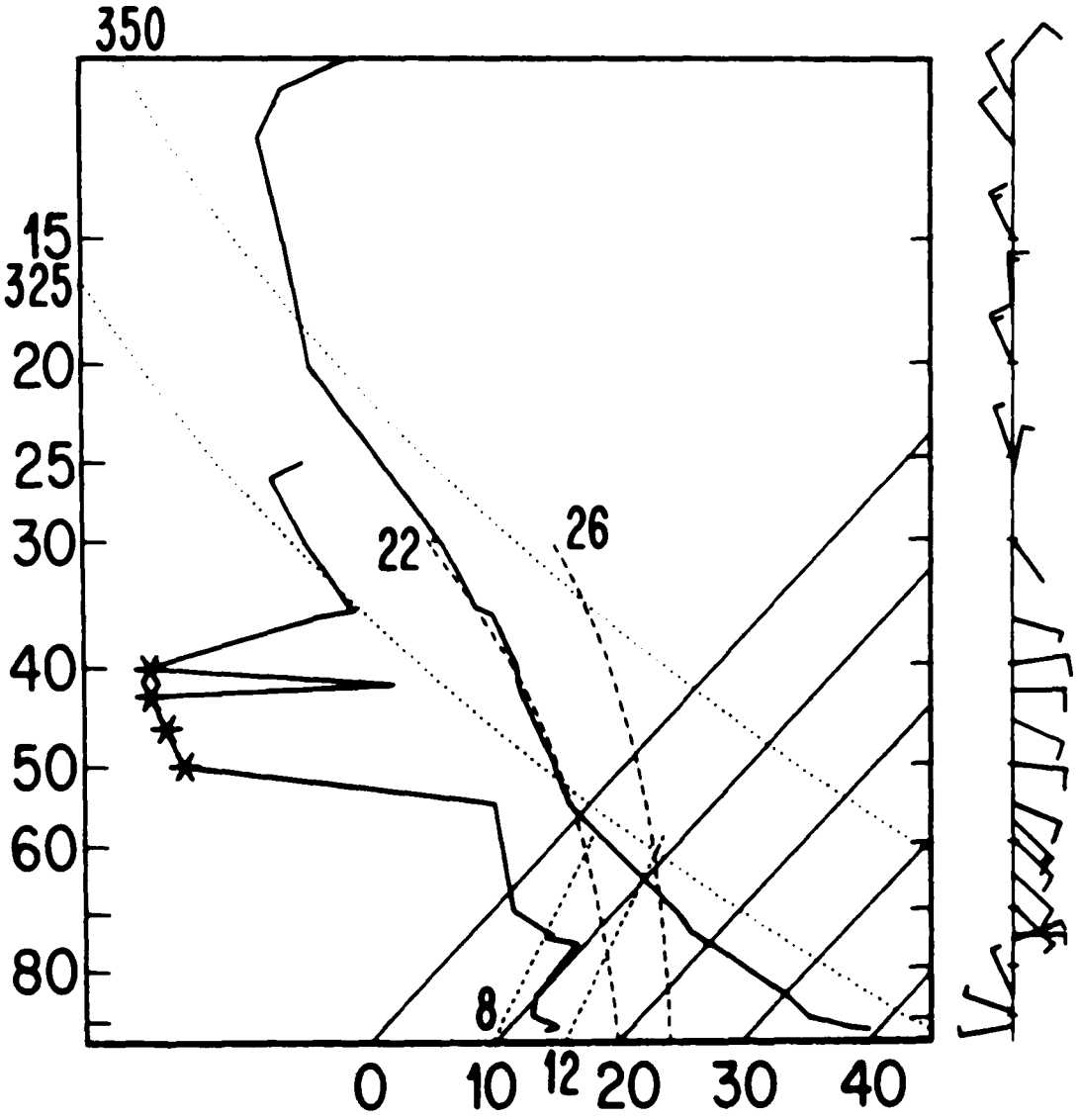

Figure 4.23 As in Figure 4.21 but for 3 August 1986.

tropopause with squall line 3. Figures 4.21-23 show that all three propagated into an environment of strong low-level wind shear which was confined mostly to the lowest 2-2.5 km. The average magnitude of the pressure-weighted vertical wind shear vector was 3.5 X 10^{-3} s^{-1} from the surface to the LCL and 1.1 X 10^{-3} s^{-1} from the LCL to 20 kPa. Thorpe et al. (1982) and Rotunno et al. (1988) found this type of environment favored long-lived systems. The magnitude of the low-level inflow was estimated by computing the wind component parallel to the direction of motion of each squall line and adding the average propagation velocity of 12 m s^{-1}. The relative inflow in the lowest kilometer above Tucson was 16-17 m s^{-1} (an average of the University of Arizona and Tucson WSO winds was used in the calculation for squall line 3). These estimates are analogous to the 10-18 m s^{-1} values computed by Mansfield (1977), Fortune (1980), Barnes and Sieckman (1984), Betts et al. (1976), and Chong et al. (1987) for tropical squall lines in other areas.

Lapse rates ahead of the squall lines were close to normal pre-thunderstorm 0000 UTC monsoon conditions which are: an almost dry adiabatic lapse rate in a well-mixed boundary layer (up to 75-70 kPa), more stable lapse rate above, and a near moist adiabatic rate from about 55 kPa to

the upper troposphere. However, the moisture profiles shown in Figs. 4.21-23 were far different from that of a typical monsoon sounding. A significant fraction of the midtroposphere was so dry (dewpoint depression ≥ 30°C) the radiosondes could not detect any moisture. Dewpoint depressions during the monsoon period usually are from 5-10°C in the 70-30 kPa layer. In addition, mixing ratios in the boundary layer were notably higher than normal, 12-14 vs. 10-12 g kg^{-1}, prior to squall lines 1 and 2. Thus, each squall line formed in a region where extremely dry, potentially cold air overlay moist air. The dry over moist stratification has commonly been associated with the development of severe thunderstorms in the central United States.

The level of free convection (LFC) estimated for each of the soundings in Figs. 4.21-23 ranged from 2.7 to 3.9 km (67-59 kPa) above Tucson. On the other hand, Chong et al. (1987) determined the LFC for their storms was only 1.2 km above the ground while Barnes and Sieckman (1984) reported it was on average just 0.47 km above the surface. The very high LFCs over southeast Arizona are due to the combination of low relative humidities near the ground and the presence of a relatively deep, well-mixed (i.e., near dry adiabatic) boundary layer which arises from strong heating of the

southern Rocky Mountains. The high LFCs also indicate a significant amount of lifting was required to initiate thunderstorms. The mean CAPE of the soundings shown in Figs. 4.21-23 is 2160 m^2 s^{-2} despite the relatively high LFCs. This is slightly less than the average CAPE, 2260 m^2 s^{-2}, computed for four different types of Oklahoma squall lines by Bluestein and Jain (1985).

Conventional indicators of instability such as the lifted index, -3 to -4 at both 50 and 20 kPa, and the total-totals index, 49 to 51, suggested presquall line conditions were favorable for the development of thunderstorms. The convective instability was estimated by determining the vertical distribution of θ_e which was calculated using the formulas in Bolton (1980). The average θ_e in the lowest 5 kPa varied from 351-357°K and is similar to that reported for other tropical squall lines, 348-353°K by Zipser (1969), Betts et al. (1976), Barnes and Sieckman (1984), Fortune (1980), and Chong et al. (1987). The minimum θ_e above Tucson ranged from 324-329°K at around 50 kPa. Between the surface and midtropospheric minimums there was a layer in which θ_e increased with height. Consequently, the presquall line environments were potentially unstable because in general θ_e decreased with height.

The composite θ_e profile derived from the three RAOBs of

Figs. 4.21-23 is the solid curve of Fig. 4.24 while the dashed curve is the average θ_e profile for all 0000 UTC July 1984 Tucson WSO soundings. Comparison of the two curves reveals several important differences. One is the noticeably lower θ_e in the midtroposphere of the squall line composite. Barnes and Sieckman (1984) reported the squall line environment had lower θ_e aloft than the nonsquall environment and Maddox et al. (1987) found high-wind producing MCCs had very low θ_e at middle levels. Another dissimilarity lies in the boundary layer where the θ_e of the squall line composite is notably higher, especially at the surface and in the upper half. A final noteworthy difference is the convection restraining stable layer found in the upper part of the boundary layer of the squall line composite but not in the July average.

The other two curves in Fig. 4.24 are θ_e profiles ahead of a West African squall line, dash-dot, from Fortune (1980, Fig. 10a) and an average before several Venezuelan squall lines, dash-three dots, from Betts et al. (1976, Fig. 3). All three curves are alike and show relatively high θ_e (potentially warm air) at the surface; a stable layer above, albeit a weak one in the Venezuelan case; and low θ_e (potentially cool air) at higher altitudes. The differences between the surface θ_e and the minimums aloft

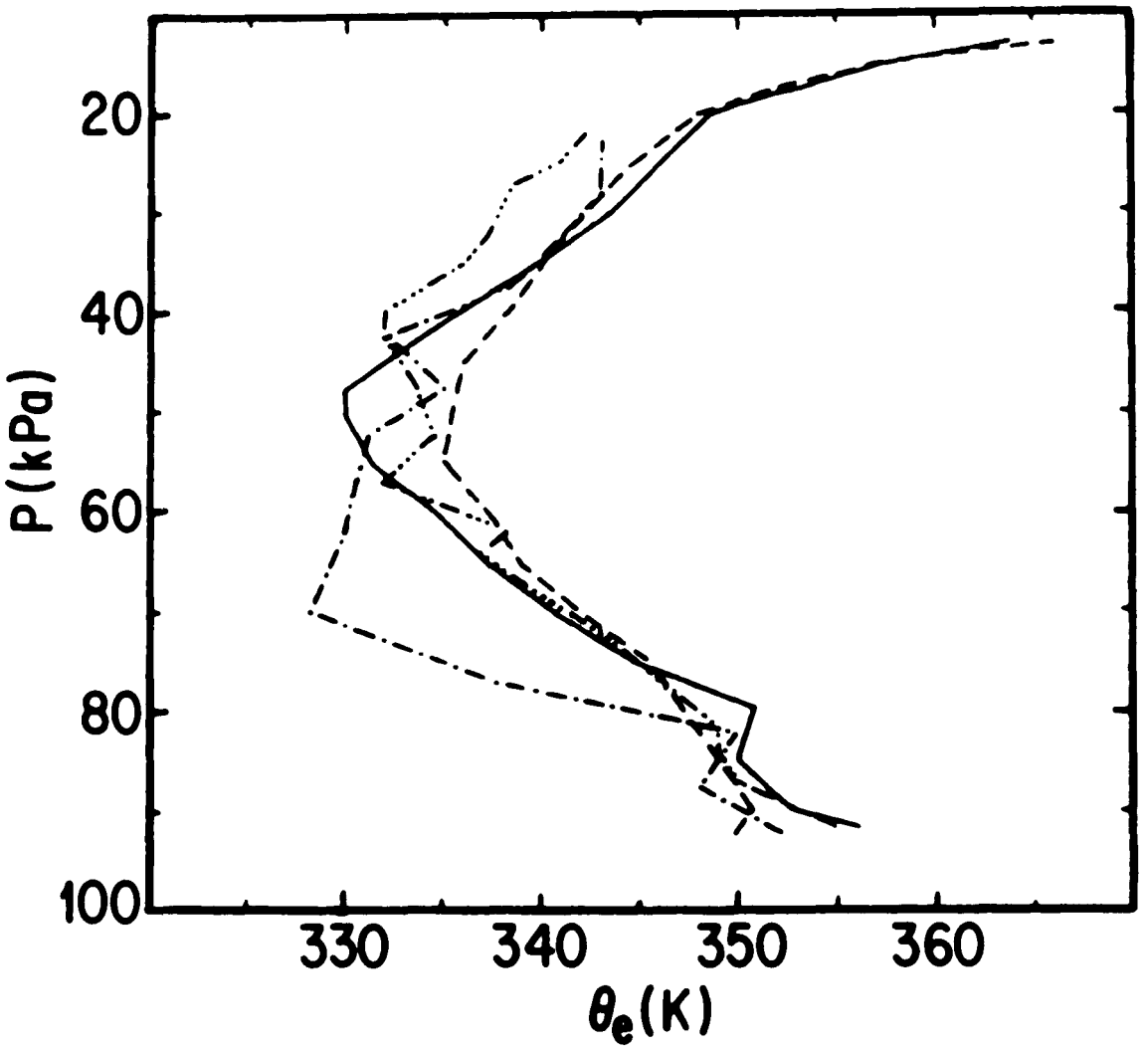

Figure 4.24 θ_e vs. pressure plots with the dashed line a composite sounding of 0000 UTC July 1984 Tucson WSO data and the solid line a composite of the three soundings shown in Figures 4.21 through 4.23. The dash-dotted line is from figure 10a of Fortune (1980) while the dash-three dotted line is from figure 3 of Betts et al. (1976). The latter two curves have been moved upward 7.5 kPa to facilitate comparison with the Tucson WSO data which begins at about 92.5 kPa.

also were practically identical. The difference was approximately 26°K in the Arizona composite (individually 23-33°K), 25°K in West Africa, and about 24°K in the Venezuelan average. Chong et al. (1987) stated the average decrease of θ_e between the surface and the midtropospheric minimum was 20-30°K in the African squall lines they studied while Barnes and Sieckman (1984) reported an average 20°K decline and Zipser (1969) a more than 24°K decrease. Maddox (1983) found the difference to be 23°K at the southwest corner of the composite central United States MCC.

4.5 VAS derived Moisture Fields

Dry, low θ_e, midtropospheric air can be identified with VAS 6.7 μm band imagery when not obscured by a thin layer of moisture or clouds in the upper troposphere (Petersen et al. 1984). The VAS 6.7 μm channel detects radiation emitted by water vapor which is a function of both the amount and temperature of the water vapor and utilizes a weighting function that extends from about 80 to 20 kPa and peaks at 40 kPa (Petersen and Mostek 1982). This imagery (Figs. 4.25-28) revealed that the extremely dry air indicated in Figs. 4.21-23 was not confined to just the Tucson vicinity and that the location of the dry air aloft may have determined where the squall lines were likely to develop. The white areas in Figs. 4.25-28 are high, thick clouds.

Figure 4.25 VAS 6.7 μm image showing the middle and upper tropospheric moisture field associated with squall line 1 at 1615 UTC 16 July 1984. The resolution is 4 km, high thick clouds are white, and dry midtropospheric air is dark gray (the darker the shading the drier the air).

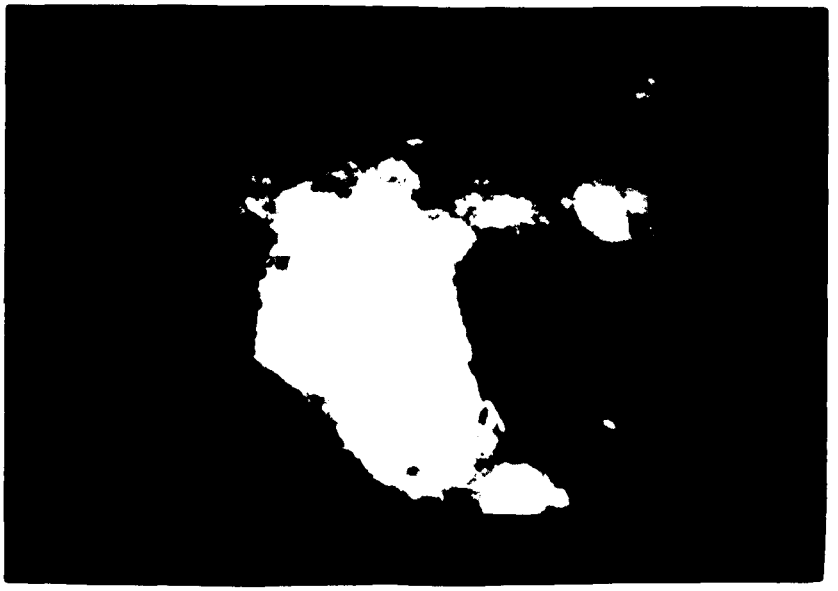

Figure 4.26 As in Figure 4.25 but from 0515 UTC 17 July 1984.

Figure 4.27 As in Figure 4.25 but from 1115 UTC 17 July 1984.

Figure 4.28 As in Figure 4.25 but from 1615 UTC 17 July 1984.

Light shading indicates the radiation received by VAS was emitted by water vapor at relatively low temperature and high altitude and suggests moist upper tropospheric air. On the other hand, dark shading indicates water vapor at relatively high temperature and low altitude or the surface was the source of the radiation and implies comparatively dry middle- and upper-tropospheric air (Petersen et al. 1983).

At 1615 UTC 16 July 1984 (Fig. 4.25) an approximately 600 km wide east-west band of extremely dry middle and upper tropospheric air extended from central Texas westward to the Gulf of California. The precipitable water field derived from the VAS data of 1248-1318 UTC 16 July (Fig. 4.29) showed a pronounced west-east gradient separating 45-50 mm amounts over the Gulf of California from 15-20 mm amounts to the east of the Continental Divide. The western end of extremely dry air subsequently moved further west and was located over the Pacific coast at 0515 UTC 17 July (Fig. 4.26). Between 1615 UTC 16 and 0515 UTC 17 July squall line 1 formed over southeast Arizona and northeast Sonora under the extremely dry air to the east of the western boundary of dry air and propagated almost to the Gulf of California. The sharp contrast in shading seen at the eastern side of the anvil cloud (refer to Fig. 4.4)

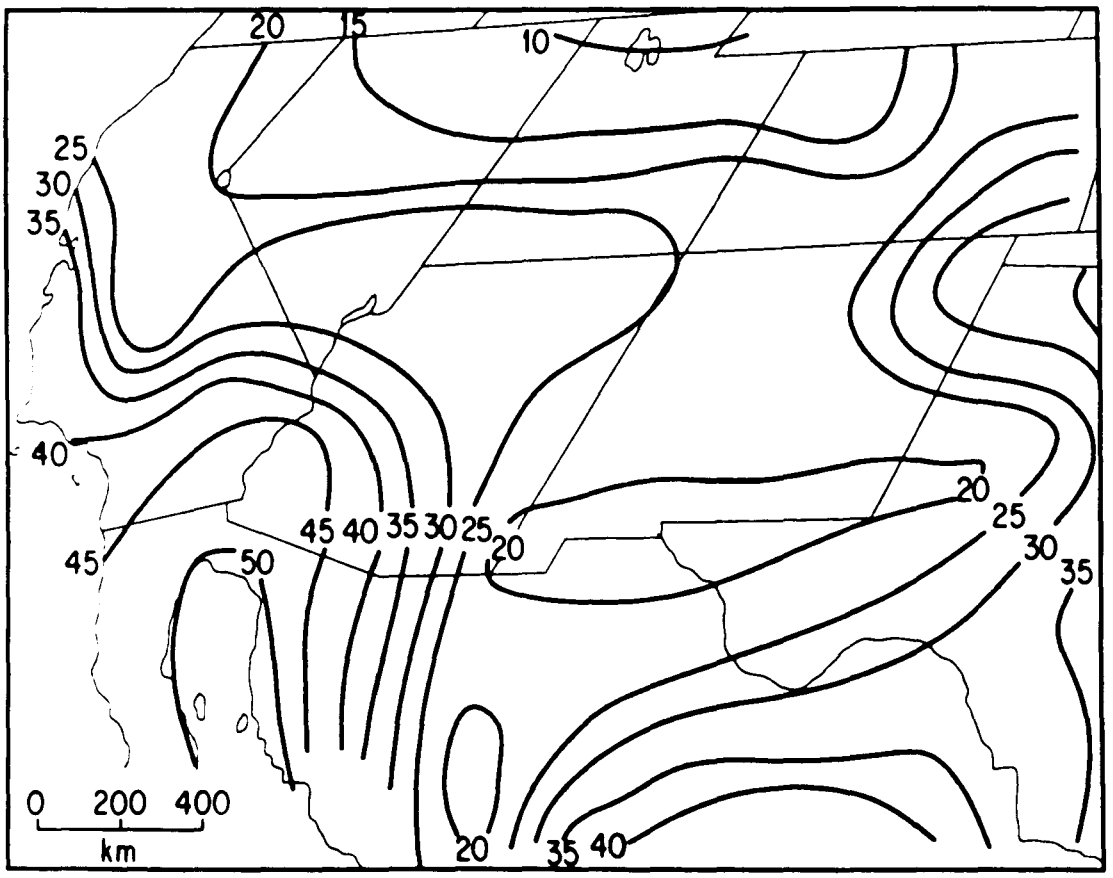

Figure 4.29 Precipitable water field derived from the VAS sounding of 1248-1318 UTC 16 July 1984. The contour interval is 5 mm.

indicates the middle and upper troposphere remained very dry upstream from the system. Elsewhere, the scattered thunderstorms that formed under the moist air aloft (compare Figs. 4.1 and 4.25) over the mountains of northern Arizona and New Mexico had dissipated.

The squall line system had essentially died by 1115 UTC 17 July (Fig. 4.27). Inspection of Figs. 4.26 and 4.27 indicates the dry air upstream from the squall line system spread and/or developed westward between 0515 and 1115 UTC. By 1615 UTC 17 July (Fig. 4.28) the western limit of extremely dry air had been advected and/or had redeveloped slightly to the west of its position of six hours earlier. VAS data from 1618-1648 UTC 17 July indicated a weaker west-east gradient existed in the precipitable water field as 45-50 mm amounts over the Gulf of California separated 25-30 mm values to the east of the Continental Divide. Later VAS 6.7 μm images showed that squall line 2 also formed under the dry air aloft and to the east of its western boundary (see Fig. 4.5). In addition, these images showed the scattered thunderstorms over the mountains of northern Arizona and New Mexico formed under moist, upper tropospheric air. All three squall lines developed where extremely dry, low θ_e, potentially cool midtropospheric air overlay hot, moist air. In addition, thunderstorms origi-

nated under the moist midlevel air over the mountains of northern Arizona and New Mexico but formed earlier in the day, were weaker, disorganized, and dissipated rapidly as the sun set. Those connected with the dry air developed later in the day, were stronger, became organized into squall lines, and persisted long after sunset. The initial thunderstorms of the squall lines arose over the mountains of southeast Arizona and northeast Sonora. Similarly, Aspliden et al. (1976) found that many west African squall lines also originated with convection over mountains. The initial thunderstorms did not develop at either the leading edge of a band of dry air or over surface fronts as Petersen et al. (1984) and Mostek et al. (1986) found in the central United States. The mountains of southeast Arizona and northwest Mexico, which are nearly perpendicular to easterly winds, apparently help organize the convection just as short waves and surface fronts do in the Midwest.

Comparison of Figs. 4.18 and 4.19 with 4.25 and 4.28 suggests the length of each squall line may have been determined by the width of the dry air bands above the Continental Divide. VAS imagery also showed the southern parts of squall lines 1 and 2 dissipated as they approached and moved offshore over the Gulf of California well to the east of the western limit of dry air. This implies the

termination of the squall lines was not caused by either the lack of low level moisture or disappearance of potentially cool air aloft. The loss of very high temperature (35-45°C) boundary layer air normally found over the Sonora desert during the day in July and August and a large decrease in the low-level wind shear probably were responsible for the demise of the squall lines.

VAS 6.7 μm imagery used in conjunction with upper air and surface observations showed that a majority of the MCSs seen over southern Arizona and/or northwestern Mexico during the 1984-88 period formed where dry air in the midtroposphere overlay moist air near the surface. However, most of these MCSs did not originate as squall lines but instead developed from scattered thunderstorms which eventually merged. Squall lines formed only when there was a dry over moist stratification and significant low-level wind shear.

4.6 Synoptic-Scale Circulation

The large-scale circulation patterns over North America and the adjacent eastern Pacific were very similar on 16-17 and 17-18 July 1984 and 2-3 August 1986. At 85 kPa, strong ridges centered near 40°N, 135°W dominated the eastern north Pacific, deep troughs covered the Great Lakes region, heights were relatively low over the Continental Divide, and were relatively high along the Pacific coast and over

the central United States and Gulf of Mexico. Troughing over the mountains was much more prominent in the late afternoon (0000 UTC) as a result of intense heating of the elevated terrain than in the early morning (1200 UTC). Temperatures were abnormally high over the Great Basin, most of California, and the Continental Divide due to the anomalous circulation over North America shown in Fig. 4.30, a composite of 50 kPa heights from 0000 UTC 17 and 18 July 1984 and 3 August 1986. The squall lines all developed to the south-southeast or south of large, high amplitude 50 kPa ridges that covered the western one-third of the United States. The typical flow at 50 kPa during monsoon conditions in Arizona is presented in Fig. 4.31, an average of 0000 UTC heights from July-August of 1984 and 1986, and Fig. 4.32 shows the difference between the squall line pattern and the "normal" monsoon circulation.

The displacement of the midtropospheric ridge from central New Mexico or the southern Great Plains to the Nevada-Utah border had several important effects. One effect was to produce an abnormally warm lower troposphere over the intermountain West and Continental Divide and anomalously low 85 kPa heights. The 85 kPa height gradient established between the relatively high values over the Pacific coast and abnormally low values over the mountains

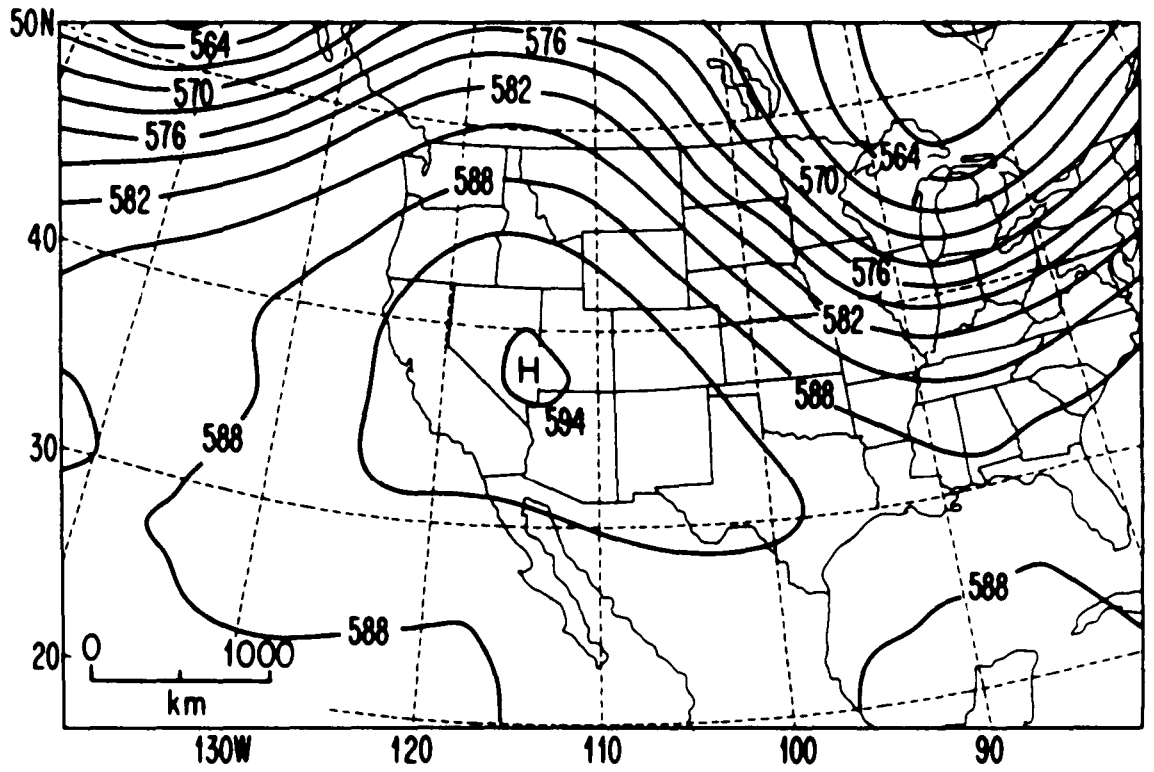

Figure 4.30 50 kPa heights (dm) for a composite of 0000 UTC data from 17 and 18 July 1984 and 3 August 1986. Ridges are marked with an H and troughs by an L.

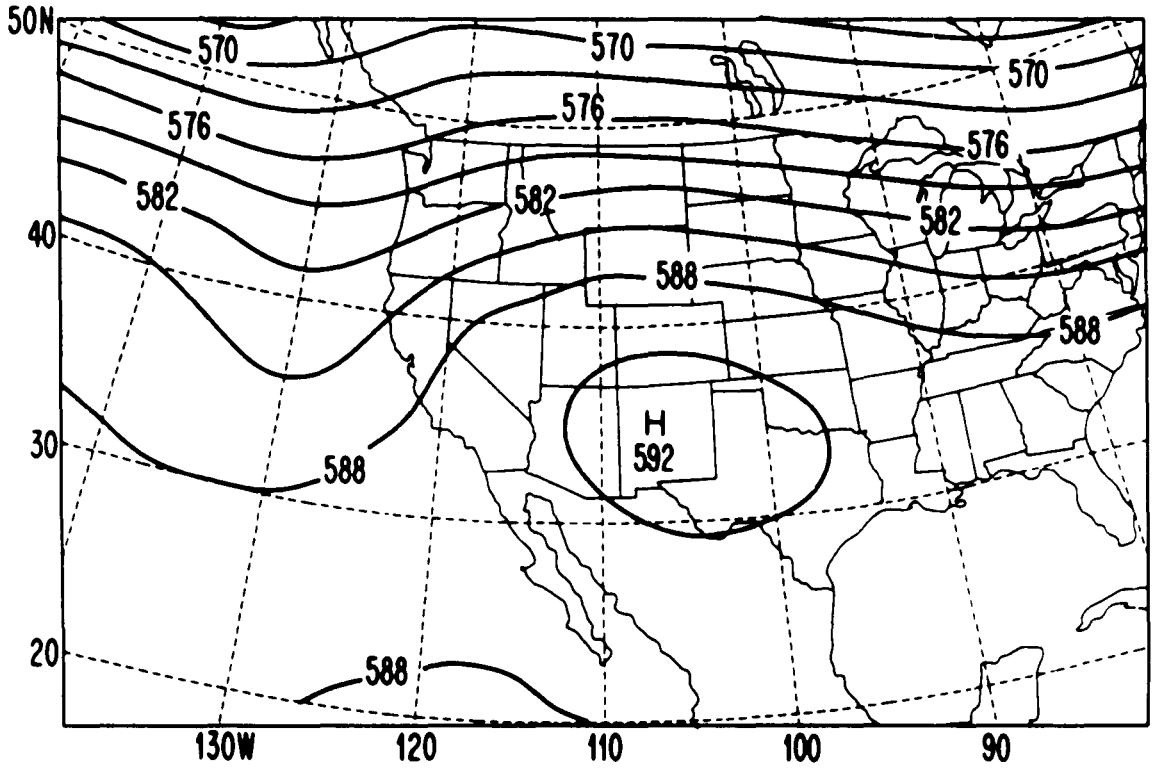

Figure 4.31 50 kPa heights (dm) for an average of 0000 UTC data from July through August of 1984 and 1986. Ridges are marked with an H and troughs by an L.

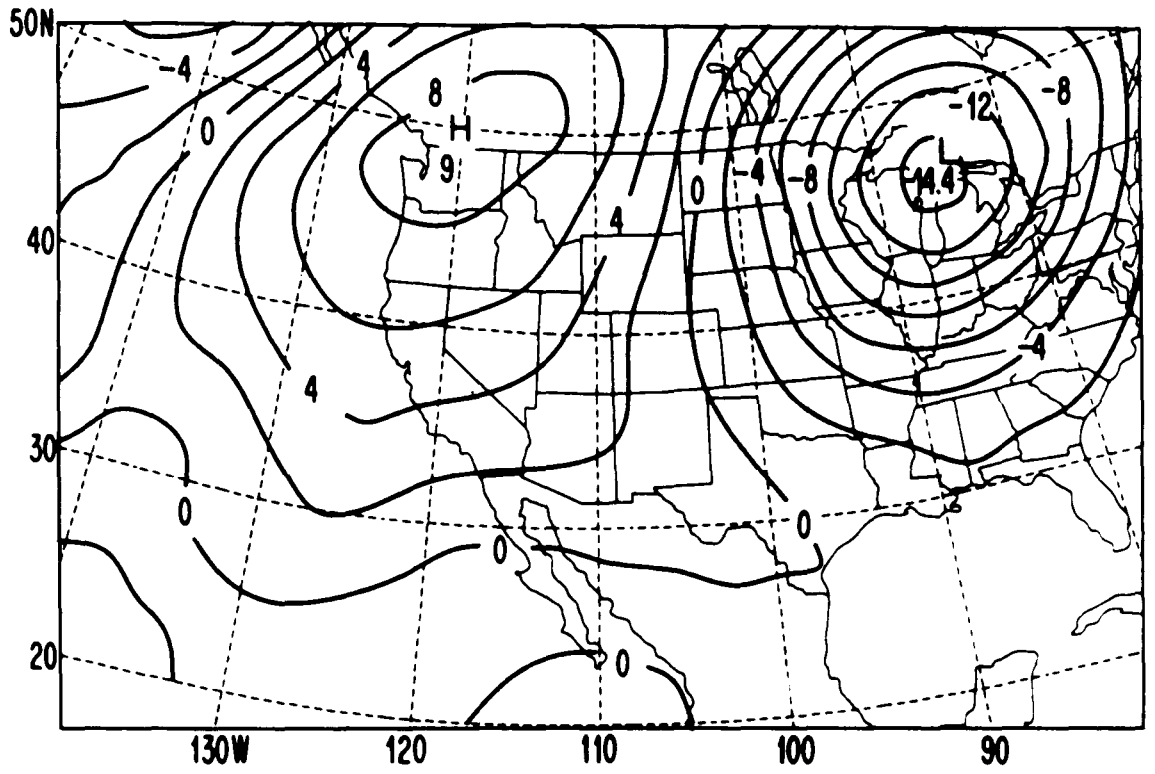

Figure 4.32 The difference in heights (dm) between Figures 4.30 and 4.31.

together with the intensification of the local mountain-valley wind circulation probably was responsible for the formation of an unusually deep layer of anomalously strong west to northwest winds. These abnormally strong winds in turn produced much greater than normal low-level wind shear. This phenomenon may be the most intense representation of what Tang and Reiter (1984) and Reiter and Tang (1984) termed the plateau monsoon of North America where heating of the elevated plateau leads to relatively low 85 kPa heights in the intermountain West. The lower tropospheric temperatures should be unusually high with the anomalously strong 50 kPa ridge and 85 kPa heights unusually low. This abnormally deep low in the lower troposphere was intense enough prior to squall line 1 that Tucson, which usually has a pronounced mountain-valley wind circulation, reported upslope west-northwest winds at 1200 UTC when downslope southeast winds normally dominate.

Another important effect the shift of the ridge to the Nevada-Utah border had on southern Arizona and northern Sonora was to change the winds aloft from southeasterly to easterly and to produce a net drying of the midtroposphere. This drying appeared to have been caused by both the advection of relatively dry air from the central United States and subsidence. In addition, the shift allowed a baro-

tropic tropical air mass with very little vertical wind shear to move over Arizona. When combined with the intense heating of the elevated plateau this gave rise to an air mass in which nearly all the vertical wind shear was confined to the lowest 2.5 km, i.e., the boundary layer; the situation Thorpe et al. (1982) and Rotunno et al. (1988) found to favor the existence of long-lived squall lines. The movement of the ridge also displaced the westerlies far to the north so that the nearest fronts or short waves were to the north and northeast of Arizona moving toward the longwave trough position over the eastern United States.

If the vorticity advection just above the surface was very small or positive, then differential vorticity advection probably did not aid the development of the squall lines because there was no synoptic-scale positive vorticity advection (PVA) at 50 kPa over the area of interest. The vorticity fields analyzed from the 0000 UTC RAOBs of 17 and 18 July 1984 showed no vorticity advection and negative vorticity advection (NVA) at 50 kPa, respectively. Missing RAOBs from 0000 UTC 3 August 1986 precluded the construction of reliable vorticity contours but forecasts of the vorticity field by the National Meteorological Center's Nested Grid Model implied NVA. In contrast, 20 kPa divergence of approximately 2.0×10^{-5} s^{-1} at 0000 UTC 17 and

3.0×10^{-5} s^{-1} at 0000 UTC 18 July 1984 was centered over the Arizona-New Mexico-Mexico border and might have assisted the development of squall lines 1 and 2, assuming the divergence existed prior to the development of the strong thunderstorms that were occurring just to the west of this area (see Figs. 4.2 and 4.5).

CHAPTER 5

DESCRIPTION OF THE MODEL

5.1 Basic Model

All three simulations to be discussed in chapter 6 used a 2D version (east-west cross section) of the numerical model developed by T. L. Clark and colleagues (see Clark 1977, 1979; Clark and Gall 1982; and Clark et al. 1987). Sound waves are filtered from the model by setting the local time derivative of density to zero and this particular version employs an anelastic approximation for density similar to that of Dutton and Fichtl (1969). The base state of the model atmosphere is at hydrostatic equilibrium and has a constant static stability, S, where:

$$S = \frac{d\ell n\bar{\theta}}{dz} \qquad 5.1$$

When S = 0, this reduces to the form of the anelastic approximation used by Ogura and Phillips (1962) and in early versions of the model (Clark 1977).

The anelastic approximation requires that the thermodynamic variables; potential temperature (θ), absolute temperature (T), pressure (P), density (ρ), and water vapor mixing ratio (q_v); be written in perturbation form:

$$\theta = \bar{\theta}(z) + \theta'(z) + \theta''(x,y,z,t) = \bar{\theta}(z)(1 + \theta^*) \qquad 5.2a$$

$$T = \bar{T}(z) + T'(z) + T''(x,y,z,t) \qquad 5.2b$$

$$P = \bar{P}(z) + P'(z) + P''(x,y,z,t) \qquad 5.2c$$

$$\rho = \bar{\rho}(z) + \rho'(z) + \rho''(x,y,z,t) \qquad 5.2d$$

$$qv = qv'(z) + qv''(x,y,z,t) \qquad 5.2e$$

where the overbar terms represent the base state that is in hydrostatic and geostrophic balance and the prime terms the deviations of the input profiles from the base state. The overbar plus single prime terms thus represent the initial state which is horizontally uniform and also is at hydrostatic equilibrium. The double prime terms are the time dependent perturbations which drive the motions in the model.

The model equations will be described in Cartesian (x,y,z) coordinates but in the model they are solved in a transformed nonorthogonal coordinate system (x,y,η) in order to accommodate irregular topography, where:

$$\eta = H(z - h)/(H - h) \qquad 5.3$$

and h is the height (m) of the topography above some base level and H (m) is the fixed height of the model "lid" (Clark 1977).

The momentum equation is:

$$\bar{\rho}DV/Dt = -\nabla P'' + k\bar{\rho}g(\theta''/\bar{\theta} - P''/\gamma\bar{P} + \epsilon_0 q_v - q_c - q_r - q_i) + \nabla\cdot\tau - \bar{\rho}\lambda V \qquad 5.4$$

where k is the unit vector in the vertical direction, V is the three-dimensional wind vector, $\gamma = C_p/C_v$, $\epsilon_0 = R_v/R_d - 1$, q_c is the cloud water mixing ratio, q_r is the rain water mixing ratio, and q_i is the ice mixing ratio. The last term on the right is a frictional term, the Rayleigh absorber, which is employed near the top of the model to limit the reflection of vertically propagating gravity waves from the model lid.

The third term on the right is the divergence of the turbulent stress energy tensor, τ. The model uses a parameterization based on the first-order theory of Lilly (1962) and Smagorinsky (1963). τ is approximated as:

$$\tau_{ij} = \bar{\rho} Km D_{ij} \qquad 5.5$$

where D_{ij} is the deformation tensor:

$$D_{ij} = \partial u_i/\partial x_j + \partial u_j/\partial x_i - 2/3\delta_{ij}\partial u_k/\partial x_k \qquad 5.6$$

and δ_{ij} is the Kronecker delta function and the total deformation, Def, is defined as:

$$Def^2 = \tfrac{1}{4}\sum_{ij}\sum D_{ij}^2 \qquad 5.7$$

Km is the eddy mixing coefficient:

$$Km = \begin{cases} (C\Delta)^2 |Def| \left[1 - \frac{Kh}{Km} Ri\right]^{\frac{1}{2}} & \text{if } \frac{Kh}{Km} Ri < 0 \\ 0, & \text{otherwise.} \end{cases} \qquad 5.8$$

with C a specified constant; Kh the eddy mixing coefficient for heat and moisture with the eddy Prandtl number, Kh/Km,

assumed to equal one in the model; Δ an effective grid scale which is equal to $(\Delta x \cdot \Delta y \cdot \Delta z)^{1/3}$ where Δx, Δy, and Δz are the model's grid increments in the x, y, and z directions; and Ri the local Richardson number:

$$Ri = g\frac{\partial}{\partial z}(\theta^* + \epsilon_0 q_v - q_c - q_r - q_i)/Def^2 \qquad 5.9$$

The turbulent heat flux, H, and the first law of thermodynamics (neglecting ice) are represented by the following equations:

$$H = \bar{\rho} Kh \nabla \theta \qquad 5.10$$

$$\bar{\rho}\frac{D\theta}{Dt} = \frac{\bar{\rho} L \theta'}{C_p T'}(C_{d1} + C_{d2}) + \nabla \cdot (\bar{\rho} Kh \nabla \theta) \qquad 5.11$$

where $\theta' = \bar{\theta} + \theta'$ and $T' = \bar{T} + T'$ are the environmental values, C_{d1} is the condensation rate of water vapor into cloud droplets due to diffusional growth, and C_{d2} is the rate at which water vapor is deposited on raindrops.

In the model, the mass continuity equation and conservation equations for water vapor (q_v), cloud water (q_c), and rain water (q_r) are, respectively:

$$\nabla \cdot (\bar{\rho} V) = 0 \qquad 5.12$$

$$\bar{\rho}\frac{Dq_v}{Dt} = -\bar{\rho}(C_{d1} + C_{d2}) + \nabla \cdot (\bar{\rho} Kh \nabla q_v) \qquad 5.13$$

$$\bar{\rho}\frac{Dq_c}{Dt} = \bar{\rho} C_{d1} - S_{ac} - S_c + \nabla \cdot (\bar{\rho} Kh \nabla q_c) \qquad 5.14$$

$$\bar{\rho}\frac{Dq_r}{Dt} + \frac{\partial}{\partial z}(\overline{\rho V_T} q_r) = \bar{\rho} C_{d2} + S_{ac} + S_c + \nabla \cdot (\bar{\rho} Kh \nabla q_r) \qquad 5.15$$

where S_{ac} is the autoconversion rate of cloud water to rain

water, S_C is the collection rate of cloud droplets by raindrops, and V_T is the mass-weighted average terminal velocity of the raindrops.

The cloud physics parameterization is based on the work of Kessler (1969) and a detailed discussion of how Kessler's scheme, which only considers liquid water, has been implemented in the model can be found in Clark et al. (1987). In this scheme, liquid water is subdivided into cloud water and rain water. Raindrops are assumed to exist in a Marshall-Palmer distribution (Marshall and Palmer 1948) and fall with their mass-weighted mean terminal velocity. In addition, a threshold cloud water content must exist before autoconversion of cloud water to rain water can take place.

The ice physics parameterization closely follows the work of Koenig and Murray (1976). Detailed descriptions of how the ice physics is implemented in the model can be found in Hall (1980) and Clark et al. (1987). Briefly, two types of ice particles, A and B, are considered in the model. Type A particles are initially small and are formed by either heterogeneous ice nucleation processes or ice splinter resulting from rime processes. The latter particles are initially larger and are created by the freezing of rain. Homogeneous nucleation of liquid water to ice is

not included in this version of the model.

The staggered grid of Harlow and Welch (1965) is utilized to represent the fields in finite difference space (Clark 1977). The definitions of x, y, and η are:

$x = (i - 3/2)\Delta x$ for i = 1, 2, ..., NX. 5.16a

$y = (j - 3/2)\Delta y$ for j = 1, 2, ..., NY. 5.16b

$\eta = (k - 3/2)\Delta z$ for k = 1, 2, ..., NZ. 5.16c

Δx, Δy, and Δz are the respective constant grid increments and NX, NY, and NZ the total number of grid points in the respective directions. The 3/2 enters into these equations because the boundary conditions are explicitly treated which means the first and last grid points are outside the domain of integration. Therefore:

$u = u(i\pm\frac{1}{2}, j, k)$ 5.17a

$v = v(1, j\pm\frac{1}{2}, k)$ 5.17b

$w, \omega = w, \omega(i, j, k\pm\frac{1}{2})$ 5.17c

$\phi = \phi(i, j, k)$ 5.17d

where ω is the vertical velocity in the transformed coordinate system and ϕ represents any of the scalars T, θ, ρ, P, Def, Kh, τ_{11}, τ_{22}, τ_{33}. The grid locations of the remaining variables are:

$\tau_{12} = \tau_{12}(i\pm\frac{1}{2}, j\pm\frac{1}{2}, k)$ 5.18a

$\tau_{13} = \tau_{13}(i\pm\frac{1}{2}, j, k\pm\frac{1}{2})$ 5.18b

$\tau_{23} = \tau_{23}(i, j\pm\frac{1}{2}, k\pm\frac{1}{2})$ 5.18c

$$H_1 = H_1(i\pm\tfrac{1}{2}, j, k) \qquad 5.18d$$

$$H_2 = H_2(i, j\pm\tfrac{1}{2}, k) \qquad 5.18e$$

$$H_3 = H_3(i, j, k\pm\tfrac{1}{2}) \qquad 5.18f$$

$$h = h(i, j) \qquad 5.18g$$

$$\eta = \eta(k\pm\tfrac{1}{2}) \qquad 5.18h$$

All thermodynamic variables are advected using the multidimensional, positive definite, advection transport algorithm described in Smolarkiewicz (1982, 1983, 1984) and Smolarkiewicz and Clark (1986).

The solar flux incident at the surface, S, is calculated using a solar constant, S_0, equal to 1395 W m^{-2} and accounts for sloping terrain (Clark and Gall 1982 and Smolarkiewicz and Clark 1985). The solar flux routine implemented in this version of the model ignores clouds and assumes half the incident short wave energy flux is converted to a sensible heat flux. Thus:

$$S = SF_c(0.5S_0)[\cos Z - h_x\cos\delta\sin\phi_r - h_y(\sin\psi\cos\delta\cos\phi_r - \cos\psi\sin\delta)]/(1+h_x^2+h_y^2)^{\frac{1}{2}} \qquad 5.19$$

where the sun's zenith angle is Z and:

$$\cos Z = \sin\psi\sin\delta + \cos\psi\cos\delta\cos\phi_r \qquad 5.20$$

and ψ is the latitude, δ is the sun's declination angle, h_x and h_y are the slope of the topography in the x (east) and

y (north) directions respectively[1], and SF_c is the solar flux coefficient which is employed to limit the temperature increase over the "oceans" (z = 0 km) to reasonable values. The hour angle is:

$$\phi_r = \pi(12 - t_w)/12 \qquad 5.21$$

with t_w the local time in hours. The local time is not a function of longitude thus all grid points in the domain have an identical ϕ_r.

The longwave cooling scheme used in the model is based upon the work of Sommeria (1976) and is described in Clark et al. (1987). This scheme is known to produce erroneous cooling and heating rates at night in the free atmosphere and has been revised in the latest version of the model (Redelsperger and Clark, 1989). Radiative cooling is not allowed in dry runs of this version of Clark's model.

The boundary conditions in the model are as follows. The velocity gradients normal to the lower and upper boundaries, η = 0.0 and H, are assumed to equal zero. $\partial\theta/\partial z$ is set equal to zero at the lower boundary and $\partial^2\theta/\partial z^2$ is set equal to zero at the upper (Klaassen and Clark 1985).

---

[1] The solar flux was incorrectly calculated in all three simulations because h_x and h_y were inadvertently switched. The solar flux should have been higher before noon and lower afterwards on the eastern slope and vice versa on the western slope. The largest errors occurred just before dawn and before sunset with very little error at midday. The maximum error was less than 3.5 W m^{-2} on the eastern slope and less than 4.5 W m^{-2} on the western.

At the surface, τ_{13} and τ_{23} are computed from the drag law formulation in Clark and Farley (1984) while at the model lid, $\tau_{13} = \tau_{23} = 0$. The sensible heat flux at $\eta = H$ is calculated so there is no vertical divergence or convergence of heat near the top of the model. A region of Rayleigh friction is employed near the top of the model to absorb vertically propagating gravity waves (the last term on the right hand side of equation 5.4). This is accomplished by letting the inverse of the Rayleigh friction time constant vary linearly with height starting from zero at the bottom of the absorber region. This absorber is applied to u', v', w', and θ' so that u, v, w, and θ are continually relaxed to environmental values. Cyclic lateral boundary conditions were utilized in these simulations because the pressure solution proved to be unstable when they were not.

The potential flow adjustment scheme described in Clark et al. (1987) was used to initialize the model. After initialization, the equations are solved using the second order finite difference operations of Lilly (1965) and Arakawa (1966) for the spatial terms and a second order leapfrog scheme for the time derivatives. Additional information on the numerical methods can be found in Clark (1977, 1979). The filter of Robert (1966) and Asselin

(1972) is applied to u, v, and w to prevent the development of the computational mode caused by the centered-in-time leapfrog differencing scheme. In addition, a ∇_H^6 horizontal spatial filter is applied to $\bar{\rho}_x u'$, $\bar{\rho}_y v'$, and $\bar{\rho}_z w'$ in the interior of the domain to damp the highest frequency modes where u′, v′, and w′ are the deviations of the respective variables from their assumed environmental profiles.

5.2 Modifications of the Basic Model

5.2.1 Dry Run

Clark's model has been employed on numerous occasions to simulate airflow over mountainous topography. The non-orthogonal, terrain-following coordinate system (x,y,η) described earlier (see equation 5.3) was incorporated into the model for precisely this reason. The model domain and topographic profile employed in all three simulations are shown in Fig. 5.1. The domain extends from sea level to approximately 20.0 km, i.e., into the lower stratosphere, so that any deep convection which develops in the model will be contained well within the domain. The lateral boundaries are set 2000 km from the Continental Divide to reduce the effects of the boundaries on the interior of the domain.

The topographic profile in Fig. 5.1 is an idealized and highly smoothed representation of the topography of

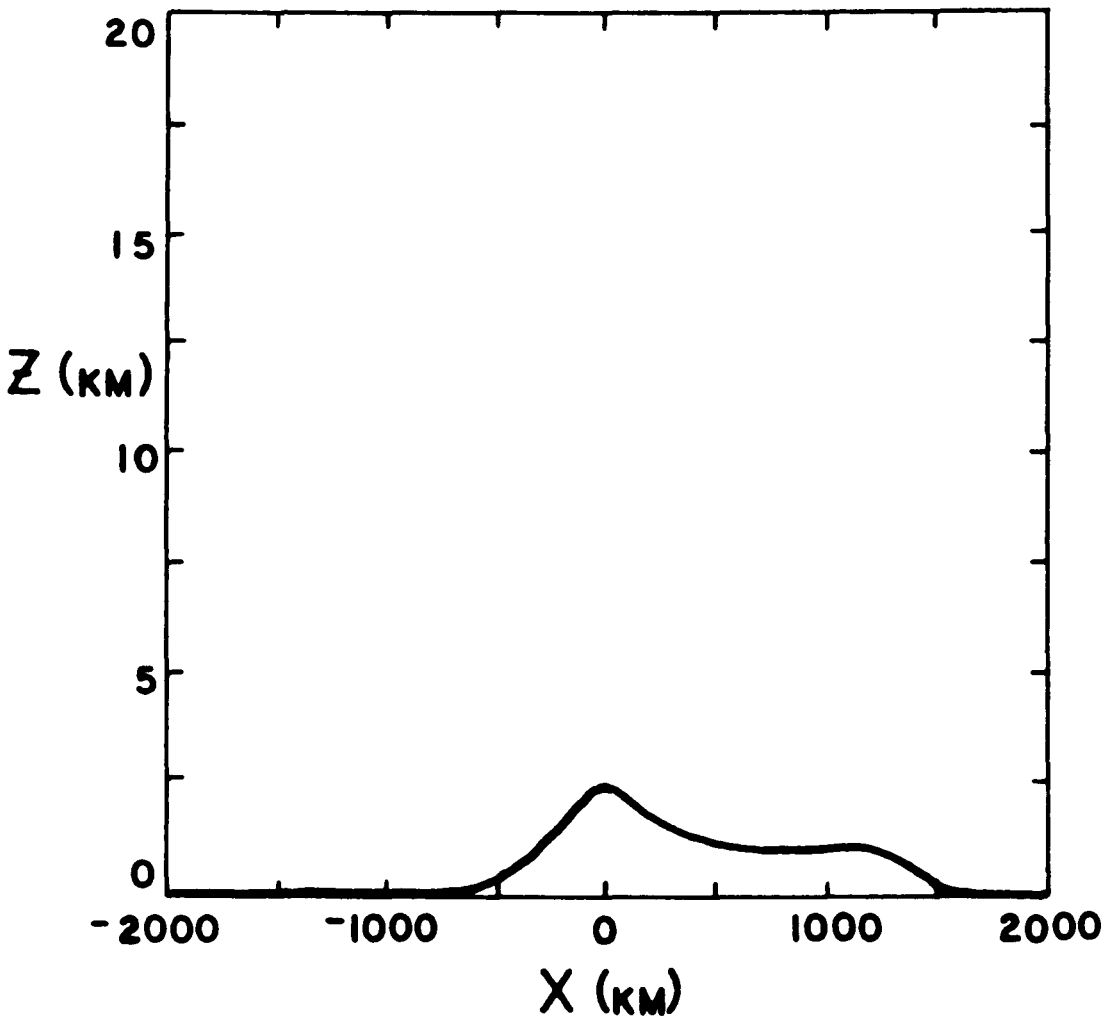

Figure 5.1 Domain (4000 X 20 km) and topographic profile (thick solid line) of the model. The highest elevation is 2.4 km at x = 0.0 km.

northern Mexico. The Gulf of California/eastern north Pacific ocean minus Baja California is depicted by the area at z = 0.0 km to the left (west) of the Continental Divide which is at x = 0.0 km and is 2.4 km high. Baja California was not included in order to keep the topographic profile as simple as possible. The Chihuahua desert is represented by the plateau at an elevation of 1.0 km immediately to the right (east) of the peak and the Gulf of Mexico is shown as the area at z = 0.0 km at the eastern boundary of the domain.

The single vertical sounding used to initialize the model is listed in Table 5.1 and plotted in Fig. 5.2. The sounding was calculated by computing a mean sounding for Tucson and Guaymus, Sonora from the respective 1200 UTC 16 and 17 July 1984 and 2 August 1986 RAOBs and using the mean Tucson sounding for $P \geq 92.5$ kPa and the mean Guaymus sounding for $P < 92.5$ kPa. The data in the vicinity of 92.5 kPa were smoothed to provide a realistic transition across this level. The composite sounding was then modified by setting the winds equal to zero at $z \leq 2.27$ km. This was done primarily to decrease the magnitude of the waves caused by initialization of the model. The wind profile in Fig. 5.1 closely resembles the unicell tropical squall line wind profiles of Dudhia et al. (1987), Nicholls et al. (1988),

TABLE 5.1 Sounding used for Initialization of the Model.

P (kPa)	z (m)	T (°C)	W (g kg^{-1})	Wind Dir. (deg.)	Speed (m s^{-1})	θ (°K)	θ_e (°K)
101.23	0	25.1	18.20	——	0.0	299.7	350.1
101.10	12	25.1	18.20	——	0.0	299.8	350.3
100.00	108	24.8	17.80	——	0.0	300.4	349.8
97.50	333	24.3	16.50	——	0.0	301.9	348.0
95.00	561	23.8	15.00	——	0.0	303.4	345.8
92.50	791	23.3	13.70	——	0.0	305.0	344.0
90.00	1030	22.8	13.20	——	0.0	306.8	344.7
87.50	1275	22.1	12.30	——	0.0	308.4	344.0
85.00	1528	21.0	11.80	——	0.0	309.8	344.2
82.50	1786	19.8	11.00	——	0.0	311.0	343.3
80.00	2052	18.7	10.40	——	0.0	312.5	343.3
77.50	2326	17.4	9.60	90.0	0.1	313.8	342.5
75.00	2605	15.9	8.80	90.0	0.8	315.1	341.5
72.50	2892	14.5	8.00	90.0	1.9	316.5	340.7
70.00	3188	12.3	7.40	90.0	3.4	317.1	339.7
67.50	3493	10.0	6.70	90.0	4.6	317.7	338.4
65.00	3806	7.6	5.70	90.0	5.6	318.3	336.0
62.50	4128	4.9	4.80	90.0	6.5	318.7	333.7
60.00	4459	2.2	4.30	90.0	7.3	319.2	332.8
57.50	4802	0.0	3.00	90.0	8.0	320.3	330.0
55.00	5157	-2.5	2.00	90.0	8.6	321.3	327.9
52.50	5525	-4.4	1.40	90.0	9.0	323.2	328.0
50.00	5907	-6.8	0.35	90.0	8.8	324.7	326.0
47.50	6306	-8.9	0.25	90.0	8.4	326.8	327.8
45.00	6723	-11.3	0.20	90.0	8.1	328.9	329.7
42.50	7161	-13.8	0.15	90.0	7.6	331.1	331.7
40.00	7620	-17.1	0.10	90.0	7.2	332.6	333.0
37.50	8101	-20.6	0.05	90.0	6.9	334.1	334.4
35.00	8608	-24.4	0.05	90.0	6.7	335.7	335.9
32.50	9142	-28.9	0.05	90.0	6.5	336.6	336.9
30.00	9709	-33.4	0.05	90.0	6.4	338.1	338.3
27.50	10318	-37.1	0.05	90.0	6.3	341.2	341.4
25.00	10971	-42.5	0.00	90.0	6.3	342.6	342.6
22.50	11673	-47.5	0.00	90.0	6.4	345.4	345.4
20.00	12438	-54.4	0.00	90.0	6.7	346.3	346.3
17.50	13283	-60.1	0.00	90.0	7.1	350.4	350.4
15.00	14231	-66.3	0.00	90.0	7.7	355.5	355.5
12.50	15321	-71.7	0.00	90.0	8.4	364.7	364.7
10.00	16627	-75.1	0.00	90.0	9.3	382.1	382.1

TABLE 5.1 continued

P (kPa)	z (m)	T (°C)	W (g kg^{-1})	Wind Dir. (deg.)	Speed (m s^{-1})	θ (°K)	θ_e (°K)
9.00	17245	-71.7	0.00	90.0	9.5	400.5	400.5
8.00	17948	-68.3	0.00	90.0	9.8	421.2	421.2
7.00	18755	-65.6	0.00	90.0	9.9	443.4	443.5
6.00	19698	-63.6	0.00	90.0	10.0	467.8	467.8
5.00	20821	-59.1	0.00	90.0	10.0	503.3	503.3
4.00	22233	-57.1	0.00	90.0	10.0	541.4	541.4

——— = no wind.

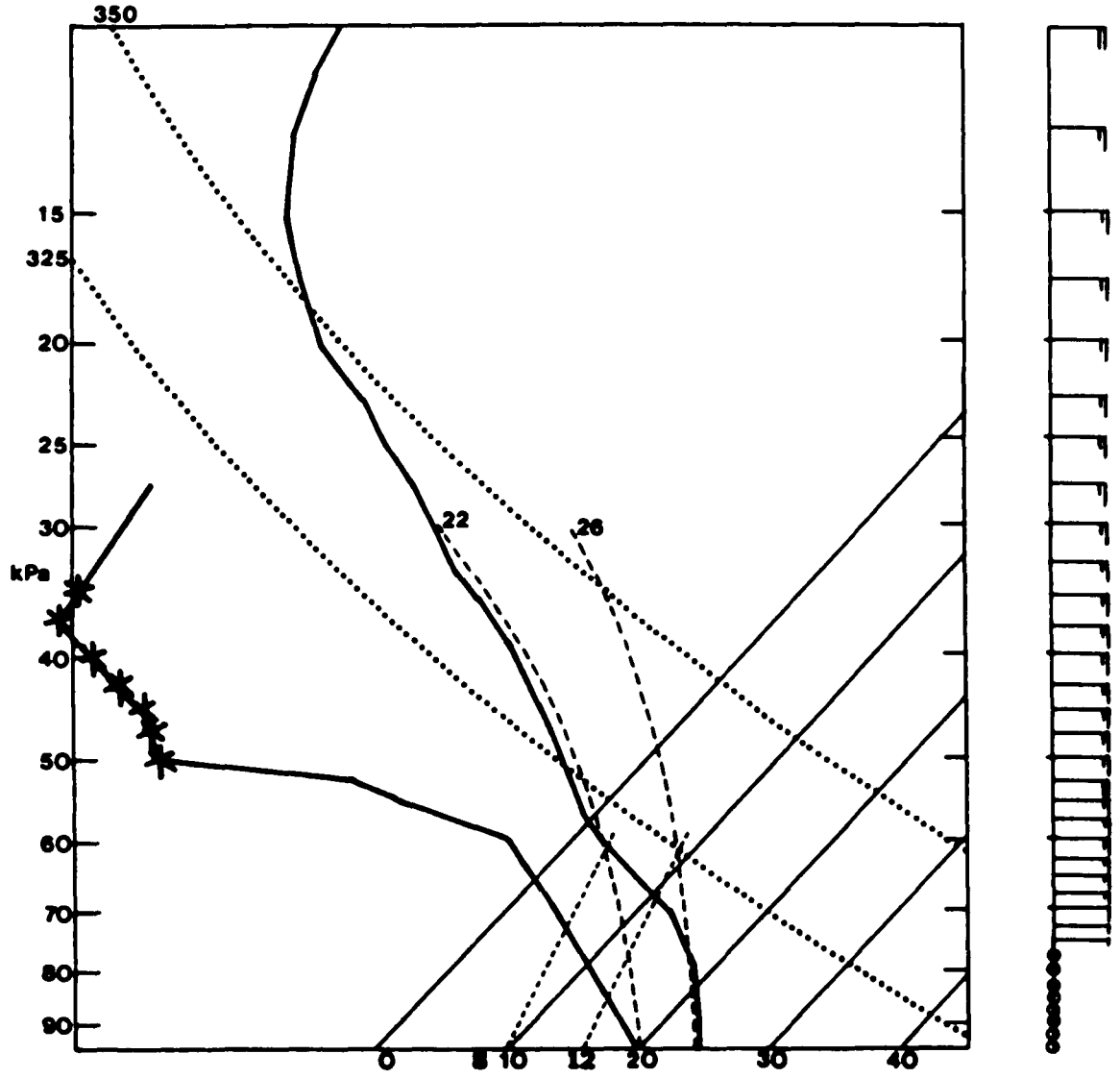

Figure 5.2 Skew T-log P plot of the sounding used for initialization of the model. Isotherms and moist adiabats are in °C, dry adiabats in °K, saturation mixing ratio in g kg^{-1}, pressure in kPa, and wind speed in m s^{-1} (long barb = 5 m s^{-1}, short barb = 2.5 m s^{-1}, o = no wind). Dewpoint depressions ≥ 30°C are indicated by an *.

and Lafore and Moncrieff (1989).

Features common to all three simulations are listed in Table 5.2 while those specific to the dry simulation are listed in Table 5.3. Some noteworthy points in these tables include the following. All three simulations were started at 5 am 22 July. The dry run lasted 1200 min and was terminated at 1 am 23 July. The temperature and pressure at z = 0.0 km shown in Table 5.2 were chosen to represent July conditions just above the surface of the Gulf of California and Gulf of Mexico. Due to the very small diurnal change in sea surface temperatures (SSTs) and the overlying air temperatures, the solar flux coefficient (SF_C) in equation 5.19 was set to zero at z = 0.0 km and was allowed to vary linearly with height until z = 0.5 km when it was set equal to one.

5.2.2 Moist Runs

The vertical distribution of water vapor employed to initialize the model is plotted in Fig. 5.2 and listed in Table 5.1. The mixing ratios also were derived from the mean Tucson and Guaymus soundings computed from the respective 1200 UTC RAOBs taken on 16 and 17 July 1984 and 2 August 1986. However, the mixing ratios in the 55.0-30.0 kPa layer were reduced so this layer would be as dry as the corresponding layers observed over Tucson at 0000 UTC 17

TABLE 5.2 Features Common to all the Simulations.

Dimensions:	2
Number of domains:	1
Size of domain (km):	4000 x 20
Latitude:	30°N
Coriolis terms:	off
Drag coefficient, C_D:	0.01
Constant in eddy mixing formulation, C:	0.2
Amplitude of ∇_H^6 horizontal filter:	0.4
Robert-Asselin time filter coefficient:	0.2
Minimum Rayleigh friction time constant for the upper level gravity wave absorber (s):	1000
Cyclic in the horizontal direction	
Pressure at z = 0 km (kPa):	101.23
Temperature at z = 0 km (°K):	298.30
Perturbation equations created about constant stability	
Initialization scheme:	Potential flow adjustment
Number of block iterations performed when solving for pressure:	3
Beginning of integration, t_0:	5 am 22 July
Attenuation length for sensible heat flux (km):	2.0
Output saved every:	10 min

TABLE 5.3 Dry Simulation.

θ is the only thermodynamic variable	
Grid intervals; Δx, Δz (km):	4.0, 0.5
Number of grid points; NX, NZ:	1002, 42
Time step, Δt (s):	30
Number of levels used to absorb gravity waves:	10
Radiative cooling:	off
Solar flux coefficient, SF_C:	
$z \leq 0.5$ km	$SF_C = 2z$
$z > 0.5$ km	$SF_C = 1$
End of integration, t_f:	1 am 23 July

and 18 July 1984 and 3 August 1986 (see Figs. 4.21-23).

Features specific to just the moist simulations are listed in Table 5.4. The horizontal grid distance, Δx, in these two simulations was halved from 4.0 to 2.0 km in order to resolve the clouds explicitly. Consequently, the total number of grid points, NX, was increased to 2002. Radiative cooling was switched on for both simulations but, as previously mentioned, the scheme in this version of the model is now known to produce erroneous results.

The solar flux coefficient was changed so that at z = 0 km SF_C = 0.33. This was done to allow the SSTs to increase slightly during the day and to reduce the magnitude of the upslope winds, which were significantly stronger than observed, that developed during the dry run.

Surface cooling was introduced into R and RI starting at 660 min (4 pm) because in the dry run and an early R simulation surface temperatures did not decrease as usually observed in the desert after the sun sets. The surface cooling was increased from zero to 70 W m^{-2} over one hour and maintained at 70 W m^{-2} until the end of the simulation[2].

---

[2] Based upon the work of Sellers (1965), 70 W m^{-2} appeared to be a reasonable value for a desert in the summer. In retrospect, this value may have been a little too high and 40 W m^{-2} might have been a more appropriate value.

TABLE 5.4 Moist Simulations.

Water vapor, liquid water, and ice also considered as potential thermodynamic variables	
Grid intervals; Δx, Δz (km):	2.0, 0.5
Number of grid points; NX, NZ:	2002, 42
Time step, Δt (s):	
R and RI ($t \leq 1020$ min)	30
RI ($t > 1020$ min)	15
Number of levels used to absorb gravity waves:	
R	10
RI	20
Radiative cooling:	on
Autoconversion rate of cloud water to rain (s^{-1}):	0.001
Threshold cloud water content required before autoconversion can occur (kg m^{-3}):	0.001
Ice nucleation rate constants (case 2 of Koenig and Murray, 1976):	$A_{06} = 464.16$, $A_{07} = 12.0$
Solar flux coefficient, SF_c:	
$z \leq 0.5$ km	$SF_c = 1.34z + .33$
$z > 0.5$ km	$SF_c = 1$
Specified surface cooling (W m^{-2}) for RI:	
$t < 600$ min	0
$600 \leq t \leq 660$ min	1.1667*(t-600)
$t > 660$ min	70
End of integration, t_f:	
R	1 am 23 July
RI	2 am 23 July

R = rain simulation; RI = rain and ice simulation.

The rain simulation was terminated at 1 am 23 July after running 1200 min. Since the first cloud in R formed after 560 min of integration, the ice physics for RI was turned on and the model restarted at 540 min (2 PM model time). RI was run until 2 am 23 July, a total of 1260 min. At around 1070 min of RI, the model blew up as the CFL (Courant-Friedrichs-Levy) condition for computational stability was exceeded. As a result, the model was restarted at 1020 min with Δt reduced from 30 to 15 s.

CHAPTER 6

RESULTS OF THE SIMULATIONS

6.1 Dry Run

Dry versions of Clark's model have been utilized to study the flow over 2D and 3D mountains (Clark 1977, 1979); the cause of severe downslope windstorms (Clark and Peltier 1977, Peltier and Clark 1979, Clark and Farley 1984); and the effect of surface heating on the airflow over 3D mountains in winter (Clark and Gall 1982). They also have been used to investigate the development of internal gravity waves forced by airflow over 2D and 3D mountains (Peltier and Clark 1983, Smolarkiewicz and Clark 1986). In addition, dry simulations have been employed to analyze the initiation and horizontal scale selection of 2D and 3D convection over gently sloping terrain caused by the interaction of convectively forced internal gravity waves in the free atmosphere with thermal convection in an unstable boundary layer (Redelsperger and Clark 1989).

The purpose of the dry run was to determine if solar heating of the elevated terrain alone could generate the conditions observed just prior to the development of the three tropical squall lines discussed in chapter 4. The two specific goals were to find out if solar heating would

produce upslope winds on both sides of the Continental Divide with pronounced low-level wind shear above the western slope and produce a convergence zone of sufficient strength near the summit that moist air parcels would be lifted to their LFC when moisture was added to the model.

After ten minutes of integration, insolation reached the surface and caused surface temperatures to start rising over the higher terrain of the model. Thereafter, boundary layer temperatures increased while the surface pressure decreased with the largest decrease located nearly on top of the Continental Divide. The low-level winds accelerated up both slopes and converged near the summit forming an area of relatively strong upward motion. Tripoli and Cotton (1989a) obtained a similar result when the central Rocky Mountains and western Great Plains were heated in their 2D model and the movement of warm air up mountain slopes during the day (valley wind) is a common occurrence in all mountainous areas. During the summer monsoon in Arizona, this causes the first thunderstorms of any given day to erupt over the mountains with development over the valleys typically occurring, if it takes place at all, several hours later. The pressure gradient force (PGF) was almost entirely responsible for the acceleration of the winds up the slopes toward the summit. The nonlinear

advection term (NL) in the momentum equation was unimportant except at the convergence zone where it commonly was about 10% of the magnitude of the PGF.

Comparison of Figs. 6.1 and 6.2 reveals the winds moving up the western slope increased from approximately 3.0 m s^{-1} at 380 min to almost 7.5 m s^{-1} four hours later in response to strong heating of the surface. During the same period, the maximum upward velocity rose from only 0.044 m s^{-1} (Fig. 6.3) to 1.1 m s^{-1} (Fig. 6.4) with most of the rise coming in the last two hours. The large increase in upward motion was due to a dramatic increase in the convergence over the peak which was caused by the continued acceleration of the low-level winds up both sides of the Continental Divide caused primarily by the PGF. However, the velocity gradients became large enough in the vicinity of the convergence zone that NL occasionally reached a magnitude almost half that of the PGF. Working together these two terms caused the convergence zone to shrink from a broad area of low velocity upward motion early in the simulation (see Figs. 6.1 and 6.3) to an approximately 5 km wide band of relatively high velocity upward motion later on (see Figs. 6.2 and 6.4).

In response to the changes near the surface, the pressure rose aloft with the maximum rise located at an

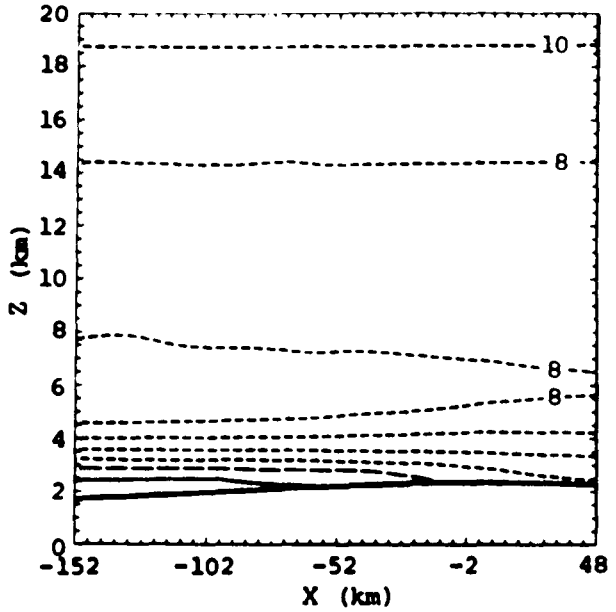

Figure 6.1 Horizontal velocity at 380 min of the dry run. The contour interval is 2 m s^{-1}, the solid lines are west winds, the short-dashed lines east winds, and the long-dashed lines the zero velocity contour.

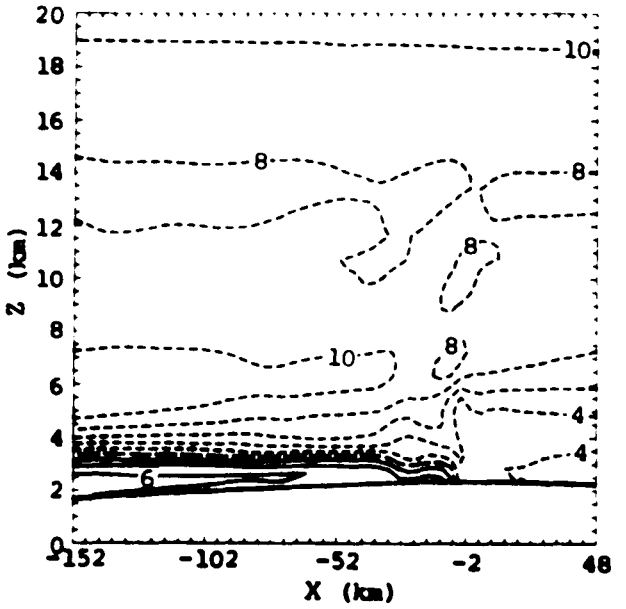

Figure 6.2 As in Figure 6.1 but for 620 min.

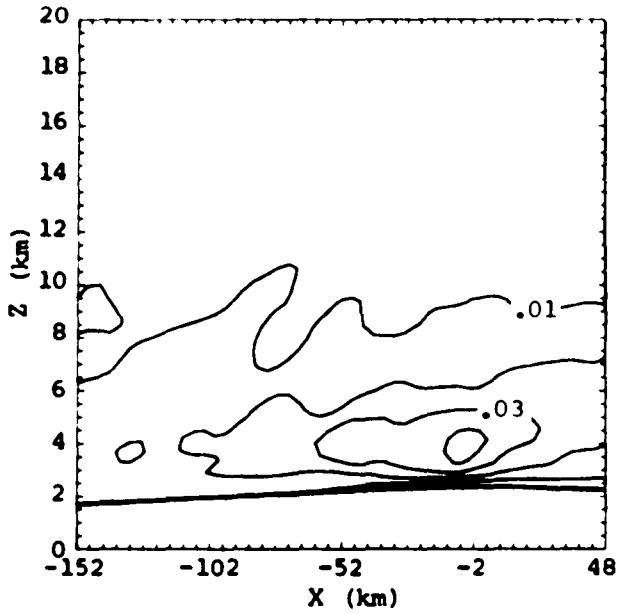

Figure 6.3 Vertical velocity at 380 min of the dry run. The contour interval is 0.01 m s^{-1} and the solid lines indicate upward motion.

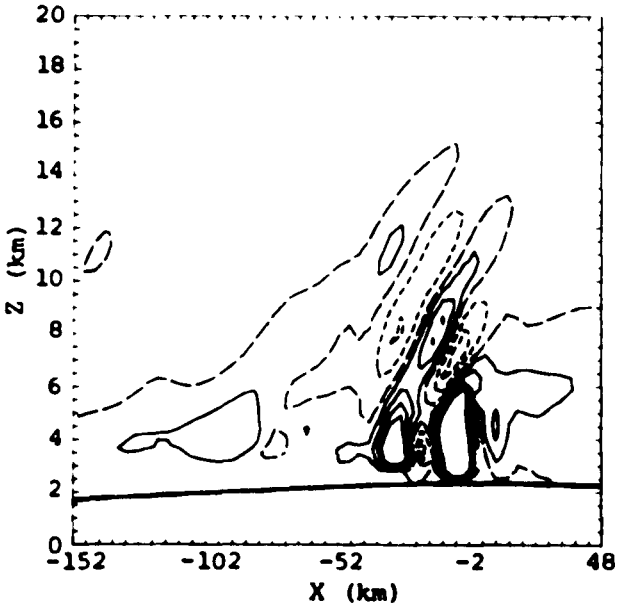

Figure 6.4 Vertical velocity at 620 min of the dry run. The contour interval is 0.05 m s^{-1}. Contours are drawn for $|w| \leq 0.2$ m s^{-1} with the solid lines showing upward motion, the short-dashed lines downward motion, and the long-dashed lines no velocity.

altitude of 6.0 km just upwind of the summit. The pressure rise aloft served to increase the speed of the midlevel easterly winds above the western slope and decrease the speed of the easterly winds over the eastern slope. This can be seen in Figs. 6.1 and 6.2 which show that in four hours the easterly wind speeds at z = 6.0 km above the western slope increased about 2.0 m s^{-1} while they decreased from 1.0-3.0 m s^{-1} at the same level above the eastern slope. The result of the acceleration of the low-level winds up the slopes and the aforementioned acceleration and deceleration of the midlevel easterly winds was the creation of a relatively strong thermally direct circulation (see Figs. 6.5 and 6.6) and pronounced low-level wind shear over the western slope, which Thorpe et al. (1982) and Rotunno et al. (1988) found favored long-lived squall lines, and a weakening of the low-level wind shear over the eastern slope. For example, Figs. 6.1 and 6.2 indicate the magnitude of the wind shear between two and six kilometers at x = -100 km increased from 2.9 X 10^{-3} s^{-1} to 4.4 X 10^{-3} s^{-1} while at x = 50 km it decreased from 1.5 X 10^{-3} s^{-1} to 0.5 X 10^{-3} s^{-1}.

Examination of the θ fields at 380 and 620 min, Figs. 6.7 and 6.8, shows that by the latter time a deep boundary layer had formed due to the combined effects of in situ

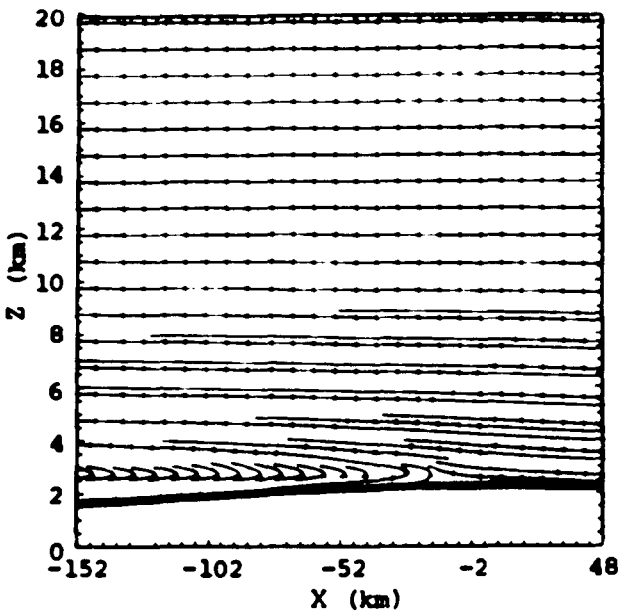

Figure 6.5 Streamlines at 380 min of the dry run.

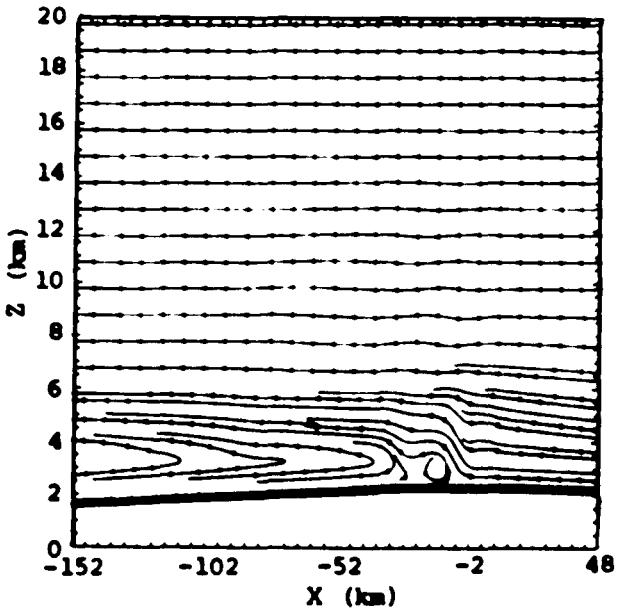

Figure 6.6 Streamlines at 620 min of the dry run.

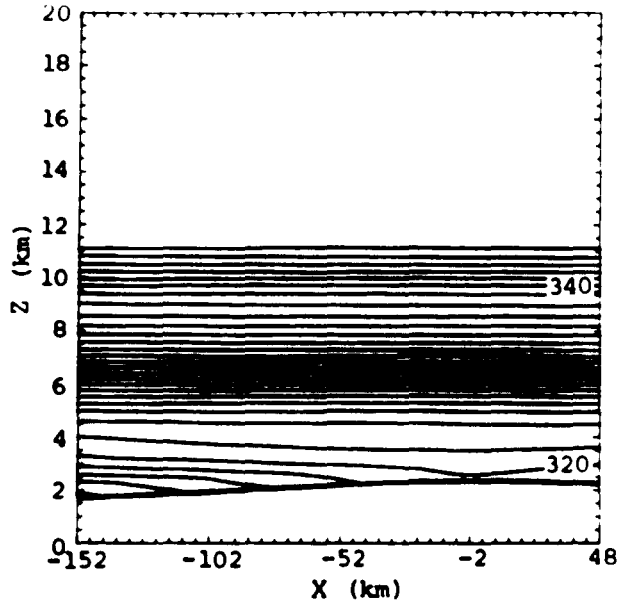

Figure 6.7 Potential temperature at 380 min of the dry run. The contour interval is 1°K and only the first 30 contours are plotted.

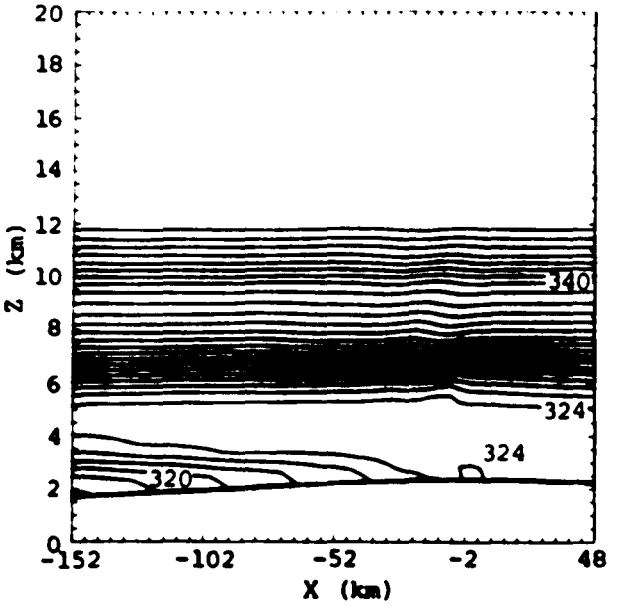

Figure 6.8 As in Figure 6.7 but for 620 min.

solar heating and warm air advection by the valley winds. This eventually lead to the establishment of a superadiabatic lapse rate and dry convection (see Fig. 6.8) in the convergence zone over the Continental Divide. The maximum upward velocity recorded in the convergence zone was more than 2.8 m s^{-1} at around 780 min, i.e., 6:00 PM model time. The average upward velocity at the center of the convergence zone remained above 1.5 m s^{-1} from approximately 720 to 920 min. It will be shown in the following sections that upward velocities of this magnitude are significantly higher those required to lift moist air parcels over the peak to their LFC and thereby initiate deep convection.

The boundary layer convection launched vertically propagating, horizontally stationary, internal gravity waves with a horizontal wavelength around 24 ± 2 km and a vertical wavelength between 5.5 and 7.5 km into the stable air above. These waves can be seen tilting into the easterly winds aloft in Fig. 6.4. These waves did not appear downstream of the convection forcing them and therefore are nondispersive hydrostatic waves.

The thermally direct circulation above the western slope kept increasing in strength during this simulation until the upslope westerly winds reached unrealistically high speeds, more than 12 m s^{-1} over a large portion of the

western slope. They stayed anomalously high even after the solar flux declined to zero. This probably was caused by the lack of longwave cooling which is not allowed in dry runs of this version of Clark's model. Consequently, the boundary layer temperatures remained abnormally high and the pressure abnormally low over the elevated terrain and, as a result, the valley winds stayed unusually strong throughout the remainder of the simulation which was terminated at 1:00 AM model time.

Solar heating of the higher topography in the dry run caused the upslope valley winds to develop on both sides of the peak which in turn met near the summit to form a strong low-level convergence zone that was only about 5 km wide. These findings are analogous to those of Tripoli and Cotton (1989a). The results obtained here imply heating of the southern Rocky Mountains and Sierra Madre Occidental may lead to the formation of a convergence zone over the Continental Divide. In addition, they suggest the relatively strong low-level wind shear observed in southern Arizona prior to the formation of these squall lines could have resulted entirely from intense heating of the southern Rocky Mountains in the presence of easterly winds aloft.

6.2 Moist Runs

With the addition of moisture, various renditions of Clark's model have been employed to simulate and/or investigate the evolution of a 3D multicellular severe storm (Clark 1979); the growth and development of 2D and 3D cumulus clouds in various environments (Hall 1980; Smolarkiewicz and Clark 1985, 1986; Klaassen and Clark 1985; Clark and Hauf 1986; Hauf and Clark 1989); and the interaction of convectively forced internal gravity waves in the free atmosphere with thermal convection in an unstable boundary layer (Clark et al. 1986). Moist versions also have been utilized to study the organization and interaction of the convective and stratiform regions of tropical squall lines (Lafore and Moncrieff 1989); the initiation and horizontal scale selection of convection over gently sloping terrain (Redelsperger and Clark 1989); and more importantly for this research, the development of cumulonimbus from local convection in an unstable boundary layer produced by solar heating of the surface (Balaji and Clark 1988).

The purpose of the rain simulation (R) was to ascertain if moist convection would develop at the convergence zone near the peak and form a squall line which would closely resemble the tropical squall lines reviewed in chapter 4. On the other hand, the most important goal of the rain and

ice simulation (RI) was to determine whether or not the addition of the ice phase would produce a more realistic tropical squall line than R.

6.2.1 Rain Simulation

There were no major differences between the dry run and R until moist convection began and the first cloud formed in the convergence zone above the peak after approximately 560 min of integration. The most notable discrepancy was that the boundary layer temperatures did not get as high and the upslope winds did not get as strong as they had in the dry run. The most important reason for this probably is that longwave cooling was turned on in R.

Four significant cloud systems and many small clouds formed in the last 640 min of the rain simulation. The first system (RCS1) evolved from the first cloud in the run and was the largest cloud mass in the domain until the fourth (RCS4), the squall line, surpassed it in size at about 900 min. RCS1 was a collection of cells which developed in front, in back, and sometimes underneath the main cloud. The strongest recorded surface winds associated with RCS1 were around 6 m s^{-1} and a rear inflow jet (RIJ) did not form under this cloud mass as it moved westward away from the Continental Divide. This system increased the humidity aloft so that subsequent convection developed

under relatively moist midtropospheric air. RCS1 was advected nearly 200 km to the west before beginning to dissipate and small scattered remnants were present ahead of the squall line throughout the remainder of the simulation.

The second relatively large cloud (RCS2) started forming in the convergence zone above the peak only ten minutes after RCS1. However, RCS2 was always much smaller than its predecessor and was incorporated into the rear of RCS1 at 820 min. Cloud system three (RCS3) also began developing over the convergence zone at around 750 min and never became as large as the first. RCS3 was advected west about 80 km before weakening, which appeared to be hastened by the upstream growth of the squall line, and its remains were still evident west of the squall line at the end of the run.

The squall line in R evolved from a cloud which formed after 810 min., 6:30 PM model time, in the convergence zone over the Continental Divide. Tripoli and Cotton (1989a) obtained a similar result in their 2D simulation of the initiation of a squall line by the Rocky Mountains in Colorado. In addition, many GATE squall lines were seen to form over mountainous terrain in Africa (Bolton 1984).

After a period of rapid growth from 870-880 min, RCS4 began to resemble a squall line and gradually acquired more characteristics of a tropical squall line as the integration continued. The squall line propagated west at about 10.0 m s^{-1} for the rest of the simulation. This speed was slightly faster than the wind speeds immediately ahead of the main cloud which averaged about 8-10 m s^{-1} but less than the 12-14 m s^{-1} winds in the RIJ (see Fig. 6.9) that developed in conjunction with the squall line. The mean propagation velocity of 10.0 m s^{-1} was substantially higher than the typical 4-6 m s^{-1} maximum wind velocity in the surface outflow. The highest wind velocity noted in the gust front was only about 10 m s^{-1} at 1130 min.

A well-developed density current did not form in the rain simulation. The average change in temperature and pressure across the gust front typically ranged from 0.25-1°C and 0.05-0.1 kPa. The strongest temperature and pressure gradients were only about 1°C and 0.1 kPa in 10 km at 1020 min and are considerably less than the gradients observed in Tucson following the arrival of the three gust fronts described in chapter 4.2.

The squall line moved through a combination of translation, wherein the main cell of the squall line was simply advected westward with new a cell occasionally developing

directly under an older decaying one, and discrete propagation, wherein a new cell would form out ahead of the deep convection and cause the entire squall line to move discontinuously west. Discrete propagation occurred three times; at 1000, 1050, and at 1100 min; when the system redeveloped nearly 10, 10, and 15 km to the west of its former position, respectively. Thus, discrete propagation was responsible for 20% of the total distance, 180.5 km, traveled by the squall line. Translation accounted for the remainder with the cells advected west at an average speed of 8.1 m s^{-1}. In contrast, Srivastava et al. (1986) found that 75% of the forward motion of the midlatitude squall line they studied was caused by discrete propagation with new thunderstorms developing up to 20 km ahead of the line and that only 25% was due to translation of the individual cells.

Propagating internal gravity waves generated by the deep convection appeared to initiate episodes of discrete propagation when they moved downstream away from the squall line and caused small clouds to form near the top of the boundary layer. Deep convection seemed to occur when upward motion in the boundary layer caused by the valley wind/gust front convergence zone and/or possibly westward propagating gravity waves moved underneath these small

clouds and in phase with the preexisting upward motion. Similarly, Balaji and Clark (1988) noted deep convection occurred when the upward motion associated with free tropospheric gravity waves and the underlying boundary layer eddies came into phase and observed that convection was suppressed when the upward motion in the gravity waves and eddies was out of phase.

Although a squall line was generated in R, a more realistic looking tropical squall line was obtained with the ice physics switched on. This can be seen when comparing the squall lines created by R and RI at 1180 min, 12:40 AM model time. For instance, the gust fronts of squall lines 1-3 produced maximum recorded winds of 20-30 m s^{-1} as they blew across southern Arizona. Close examination of Figs. 6.9 and 6.10 reveals the RI squall line generated much higher wind speeds than the one in R, 16 vs. 4 m s^{-1}, respectively. This was true throughout the entire simulation. Furthermore, the streamline plots, Figs. 6.11 and 6.12, indicate a stronger circulation existed in the surface outflow of RI.

Figures 6.9 and 6.10 also show the easterly winds ahead of and aloft behind the RI squall line are weaker than those of R and thus in better agreement with the satellite derived data presented in chapter 4.1. These and other

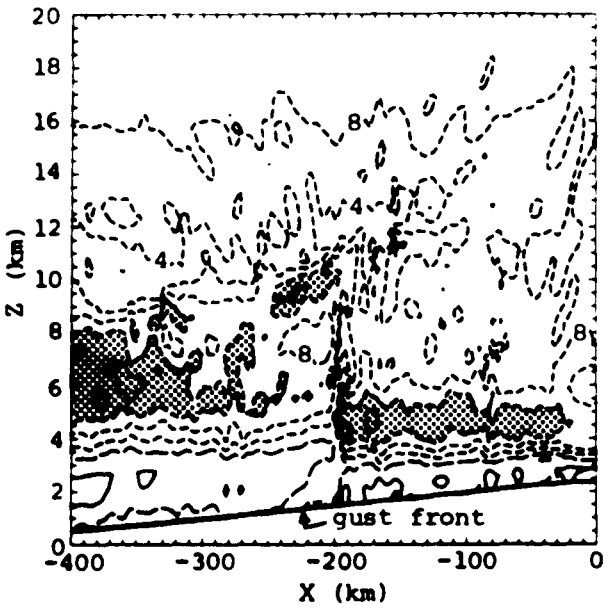

Figure 6.9 Horizontal velocity at 1180 min of the rain simulation. The contour interval is 4 m s^{-1}, the solid lines are west winds, the short-dashed lines east winds, and the long-dashed lines the zero velocity contour. The dotted areas show east winds ≥ 12 m s^{-1}. The maximum wind speed in the gust front is approximately 4 m s^{-1}.

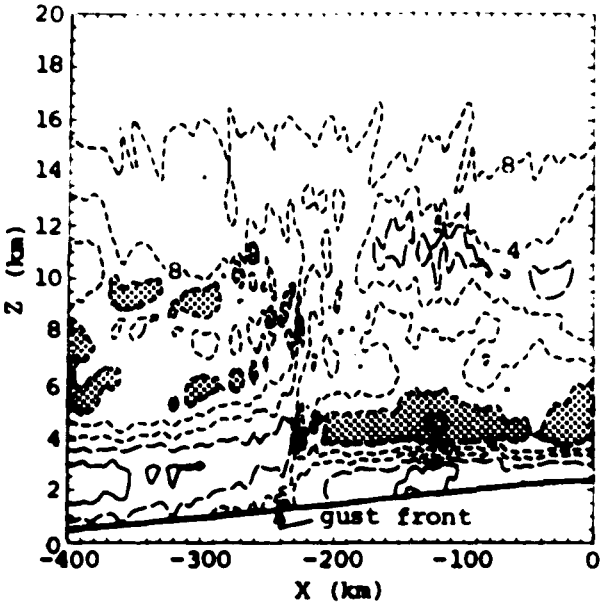

Figure 6.10 As in Figure 6.9 but for the rain and ice simulation. The maximum wind speed in the gust front is approximately 16 m s^{-1}.

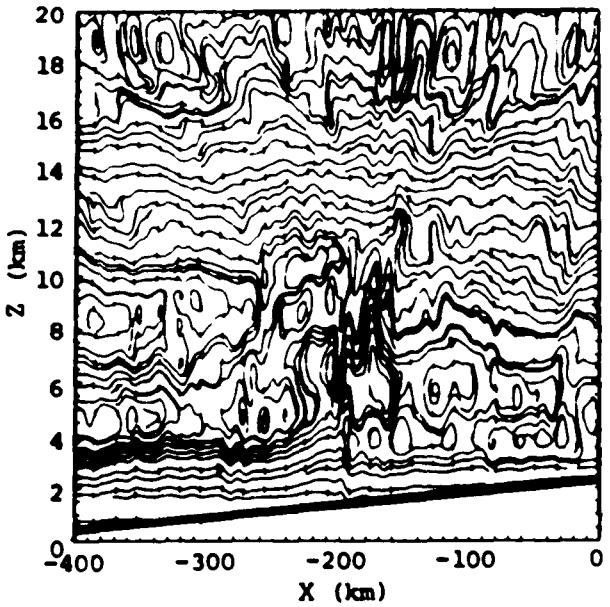

Figure 6.11 Streamlines in the frame of reference moving at the average propagation velocity of the rain squall line, 10 m s^{-1} to the west, at 1180 min of the rain simulation.

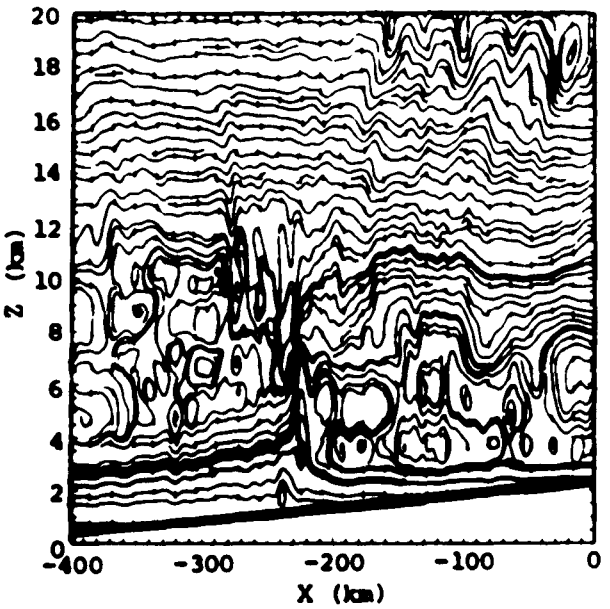

Figure 6.12 Streamlines in the frame of reference moving at the average propagation velocity of the rain and ice squall line, 10.5 m s^{-1} to the west, at 1180 min of the rain and ice simulation.

images revealed the eastern edge of the anvil clouds either were stationary over or spread a little upstream of the Continental Divide as the squall lines moved west across the desert. The winds in part of the trailing anvil of RI have actually reversed direction and become westerly (the areas enclosed by the long-dashed lines in Fig. 6.10).

In addition, the tops of the anvil clouds generally reached altitudes of 14-16 km over southern Arizona and northwestern Mexico. The anvil generated in the rain simulation (Fig. 6.13) is almost three kilometers below that of the rain and ice simulation (Fig. 6.14) which lies in the middle of the aforementioned range. This same result was noted by Nicholls (1987) who found the cloud tops in his modelled tropical squall line were three kilometers higher when the ice physics was included. Comparison of these two figures also shows fewer small clouds ahead of the RI squall line and that the RI anvil is much larger and extends about 70 km further behind the squall line which again is in closer agreement with observations. Lafore and Moncrieff (1989) also noted inclusion of the ice physics in Clark's model created a more realistic trailing anvil in their simulations of West African tropical squall lines.

For these reasons, RI was judged to have produced a squall line which more closely resembled the tropical

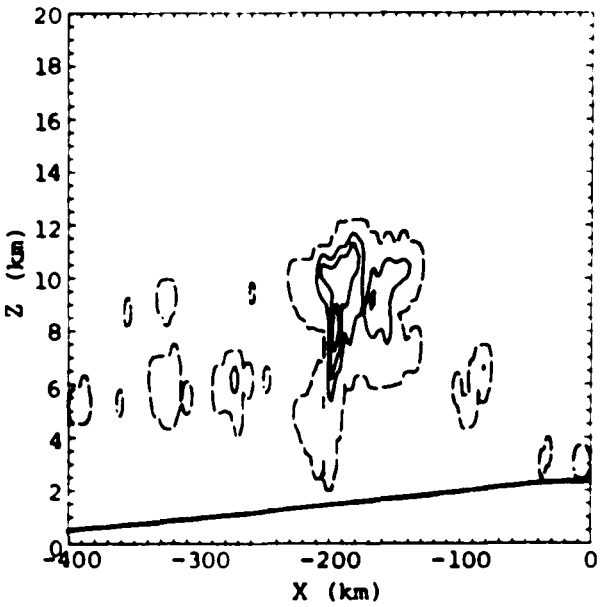

Figure 6.13 Cloud water mixing ratio at 1180 min of the rain simulation. The contour interval is 1 g kg^{-1}. The long-dashed lines are the 0.01 g kg^{-1} contours and show the extent of the clouds.

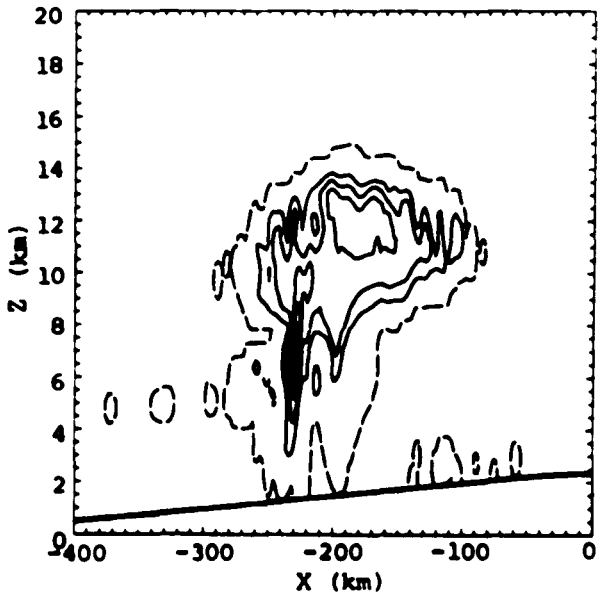

Figure 6.14 As in Figure 6.13 but this plot shows the combined cloud water and cloud ice mixing ratio fields and is for the rain and ice simulation.

squall lines seen during the summer monsoon over Arizona and northwestern Mexico. As a result, a detailed discussion of the model squall line will be made using output from the rain and ice simulation.

6.2.2 Rain and Ice Simulation

Moist convection including the ice phase began after 560 min of integration and for the next several hours there were very few noteworthy differences with R. The contrast between R and RI became larger and more significant with time. One major discrepancy was that noticeably fewer small clouds developed in this case. However, four relatively large cloud systems (CS1-4) formed and the first three were very similar to their counterparts in R.

The initial cloud which developed in the convergence zone over the peak became the first large cloud mass and was the biggest until the fourth, the squall line, surpassed in size about five hours later. Like its counterpart in R; CS1 was advected west with new convection sometimes developing ahead, under, and behind the main cloud mass; produced a gust front with a maximum recorded wind speed less than 6 m s^{-1}; and increased the humidity aloft for the succeeding cloud systems. CS1 began dissipating rapidly after 890 min, shortly after CS4 became a squall line. The second cloud system also originated over the

summit ten minutes after the first and was incorporated into the rear of CS1 a few hours later. The deep convection that grew into CS3 began above the convergence zone at approximately 750 min. CS3 never was anywhere near as large as CS1 and was totally insignificant compared to CS4. At around 860 min the upper level outflow of CS4 was advected into the rear of this system which for all practical purposes was completely gone an hour and a half later.

The squall line of the rain and ice simulation developed from the cloud first seen above the convergence zone just west of the summit at 780 min, i.e., 6:00 PM model time. This cloud remained nearly stationary for the next forty minutes while growing very slowly. More rapid growth followed as the cloud drifted westward at approximately 8 m s^{-1}. Surface outflow with winds less than 4.0 m s^{-1} was observed after one hour.

A period of intense convection and rapid growth which occurred from 866-884 min marked the beginning of the squall line. During this time, the low-level westerly winds feeding the main squall line updraft accelerated to more than 12 m s^{-1}, pronounced horizontal divergence (DIV = $\Delta u/\Delta x$) developed near the top of the cloud where the maximum DIV exceeded 7 x 10^{-3} s^{-1}, and a RIJ (defined as the area with easterly winds > 12 m s^{-1}) became established at

altitudes of 4-6 km behind the squall line (Fig. 6.15).

The streamlines shown in Fig. 6.16 and in the other figures of this chapter are plotted in a frame of reference moving at 10.5 m s^{-1} to the west (the average propagation velocity of the RI squall line). Figure 6.16 indicates a very strong counterclockwise circulation was just ahead of the squall line and formed the western part of the squall line updraft seen at x = -37.5 km in Fig. 6.17. This circulation existed at low levels prior to the initiation of the squall line but the deep convection generated positive vorticity ($\zeta = \partial w/\partial x - \partial u/\partial z$) which noticeably strengthened the circulation immediately downstream and created negative ζ at midlevels just to the rear which produced a weaker clockwise circulation.

An examination of the various components of the vorticity tendency equation shows which terms probably were responsible for the production of the aforementioned vorticity field. After taking $-\partial/\partial z$ of the horizontal component and $\partial/\partial x$ of the vertical component of the momentum equation (equation 5.4), adding the two resulting equation together, and rearranging one obtains the vorticity tendency equation for the xz plane (neglecting the Rayleigh friction term):

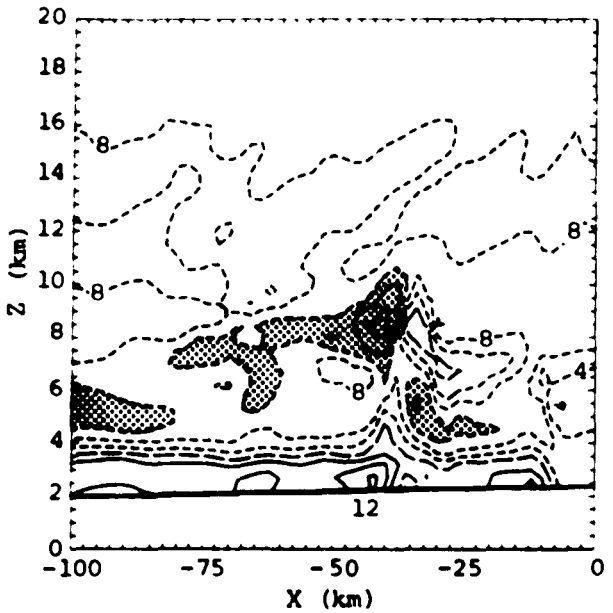

Figure 6.15 Horizontal velocity at 870 min of the rain and ice simulation. The contour interval is 4 m s^{-1}, the solid lines are west winds, the short-dashed lines east winds, and the long-dashed lines the zero velocity contour. The dotted areas show east winds ≥ 12 m s^{-1}.

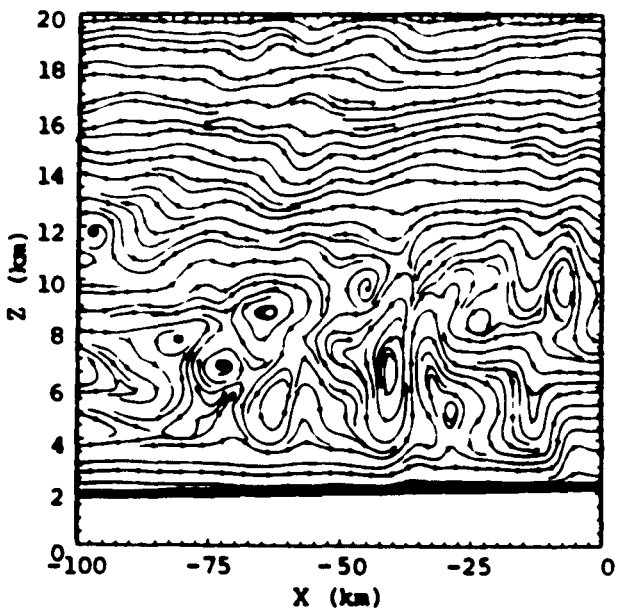

Figure 6.16 As in Figure 6.12 but at 870 min of the rain and ice simulation.

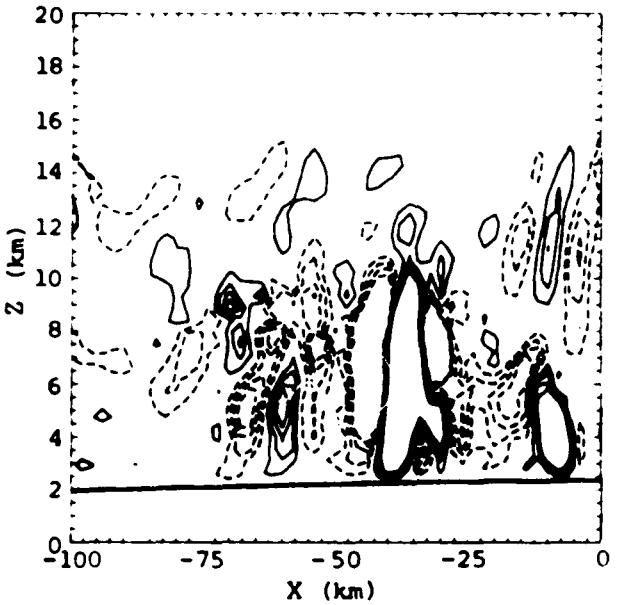

Figure 6.17 Vertical velocity at 870 min of the rain and ice simulation. The contour interval is 0.25 m s^{-1}. Contours are drawn for $|w| \leq 1$ m s^{-1} with the solid lines showing upward motion and the short-dashed lines downward motion.

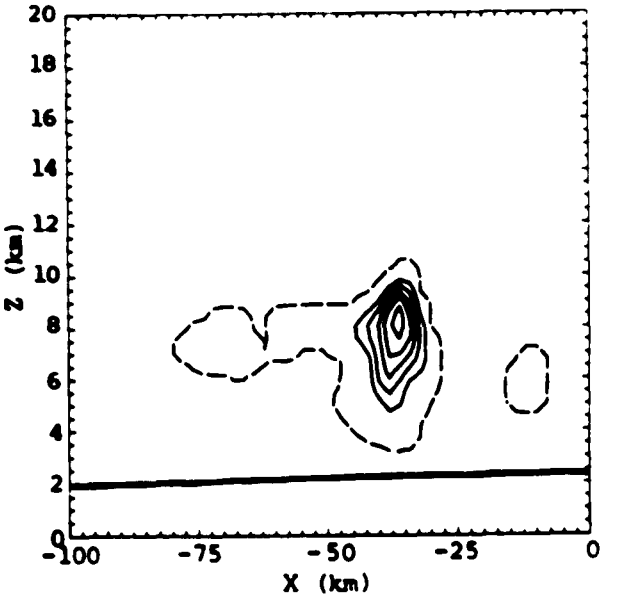

Figure 6.18 As in Figure 6.14 but for 870 min.

$$\partial\zeta/\partial t = \underset{1}{-u\partial\zeta/\partial x} \underset{2}{- w\partial\zeta/\partial z} \underset{3}{- (\partial u/\partial x + \partial w/\partial z)\zeta} +$$

$$\underset{4}{(\partial F/\partial x - \partial F/\partial z)} + \bar{\rho}^{-2}\underset{5}{\left[\frac{\partial\bar{\rho}}{\partial x}\frac{\partial P'}{\partial z} - \frac{\partial\bar{\rho}}{\partial z}\frac{\partial P'}{\partial x}\right]} +$$

$$g\partial/\partial x(\theta'/\bar{\theta} - P'/(\gamma\bar{P}) \underset{6}{+ \epsilon_0 qv - qc - qr - qi}) \qquad 6.1$$

where $F = \nabla \cdot \tau$ and the terms on the right hand side of the equation are:

1. the advection of horizontal ζ gradients by u, the horizontal advection term;
2. the advection of vertical ζ gradients by w, the vertical advection term;
3. the tendency due to divergence;
4. the tendency due to stress;
5. the solenoidal term;
6. and the tendency created by horizontal gradients of buoyancy caused by variations in θ, P, q_v, q_c, q_r, and q_i, respectively.

The circulations adjacent to the squall line updraft appeared to result mostly from the creation of horizontal θ gradients associated with the squall line updraft itself, which had a higher θ than the surrounding environmental air and the horizontal and vertical advection of preexisting ζ gradients. The other terms in the ζ tendency equation (the stress term was neglected) were far less important. The

strong divergence aloft also seemed to have been caused mostly by these three terms. The θ term was especially important near the equilibrium level where the change from positive to negative buoyancy in the squall line updraft produced a negative over positive ζ tendency to the west of the updraft and a positive over negative tendency to the east. Consequently, as seen in Fig. 6.15, the easterly wind speeds aloft increased to more than 21 m s^{-1} west of the deep convection while to the east they decreased to zero and became westerly.

The creation of horizontal θ gradients by the mesoγ-scale updrafts and downdrafts of the deep convection and the horizontal and vertical advection of ζ gradients by u and w appeared to be the dominant processes involved in the creation of the ζ field associated with the RIJ. The other terms in the vorticity tendency equation were of lesser importance. This result is similar to that obtained by Lafore and Moncrieff (1989) who found their simulated RIJ was created by horizontal θ gradients generated through latent heat release in the deep convection and unsaturated mesoscale descent beneath the trailing anvil. Initially, the vertical advection term was important only at the convergence zone over the peak where the upward advection of the negative ζ gradient generated over the eastern slope

combined with the positive θ gradient across the convergence zone to produce a positive tendency. This eventually caused the eastern end of the RIJ to become established over the convergence zone. Later in the simulation, the vertical advection term became almost as important as the θ term.

The vertical motions in the vicinity of the squall line at 870 min are presented in Fig. 6.17. This figure shows the main squall line updraft with w_{max} = 13 m s^{-1}, vertically propagating gravity waves in the upper troposphere above the upward motion in the convergence zone at x = -8 km, downward velocities at x = -33 km which are associated with a small amount of precipitation reaching the surface, and strong subsidence which extends about seven kilometers west of the squall line. A propagating gravity wave (+w at -60 km and -w -67 km) generated by earlier convection and moving west at 14.5 m s^{-1} relative to the ground also can be seen in Fig. 6.17. The maximum upward velocity, 18.3 m s^{-1}, recorded in this project (the maximum and minimum velocities were printed out every 4 time steps) occurred at 874 min.

The cloud water and ice mixing ratio, q_{ci}, presented in Fig. 6.18 reveals the upper level outflow ahead of CS4 already had been advected into the rear of dissipating CS3

near x = -62 km by 870 min. In addition, the figure shows a small cloud above the convergence zone and a cloud top near 10.5 km with no anvil trailing the developing squall line. Thus, the RIJ formed before a trailing anvil evolved just as Rutledge et al. (1988) observed in their study of a midlatitude MCS.

After the squall line had been advected west approximately 30 km in the following hour, discrete propagation occurred twice within the next forty minutes and caused the squall line to discontinuously move about 10 km further west each time. In the first case, a new cumulonimbus developed ahead of the squall line because of the strong convergence between the valley wind and either the gust front and/or the RIJ while in the second, a westward propagating gravity wave seemed to initiate a new cloud which appeared to become a thunderstorm when the valley wind/gust front induced convergence zone moved underneath.

A westward propagating gravity wave did cause convection to break out near x = -119 km at 950 min, more than 15 km west of the valley wind/gust front convergence zone. This cloud eventually reached an altitude of 9 km and produced a little rain and a weak gust front before weakening. The squall line did not redevelop westward to the site of this convection.

About one hour later, a new cell was initiated directly beneath the decaying cell of the squall line by the convergence of the valley wind with the gust front and RIJ at x = -120 km. The results of Lafore and Moncrieff (1989) also suggest the RIJ enhanced convergence at the squall line and helped generate new convection. Another episode of discrete propagation occurred from 1030-1060 min when two new cells formed ahead of the squall line in rapid succession and caused the system to redevelop about 10 km further west in both cases. The first cumulonimbus probably was generated in the same manner as the one at x = -120 km. On the other hand, the second appeared to have been forced solely by the valley wind/gust front induced convergence zone.

Several notable features of the simulated squall line are apparent in Fig. 6.19, a plot of the horizontal wind component at 1050 min. One noteworthy characteristic is the pronounced divergence aloft which has created strong outflow ahead of and behind the squall line at altitudes of 9-10.5 km. A second is the RIJ that is evident from z = 3.5-5 km and extends westward to the squall line. Another feature of note is the one kilometer deep surface outflow with maximum easterly winds > 18 m s^{-1}. The highest wind velocity observed in the gust front, 21.7 m s^{-1}, was recorded (output was saved every 10 min) just ten minutes

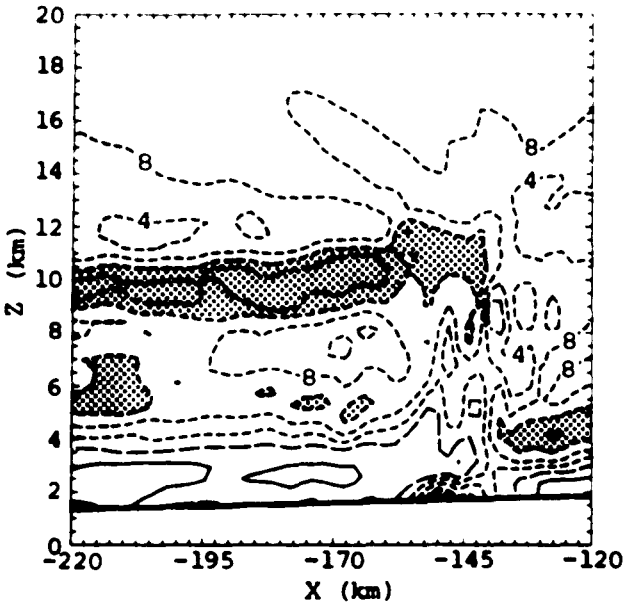

Figure 6.19 As in Figure 6.15 but for 1050 min of the rain and ice simulation.

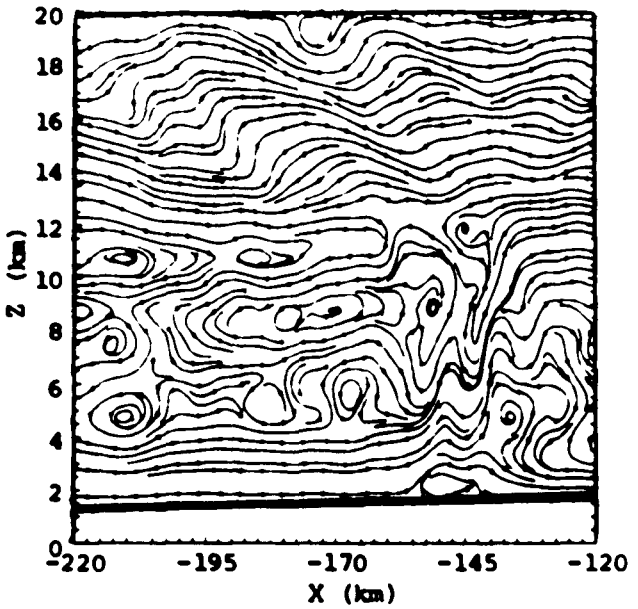

Figure 6.20 As in Figure 6.12 but at 1050 min of the rain and ice simulation.

earlier. The strong winds in the gust front can also be seen in the streamline plot (Fig. 6.20). Lastly, a weakening valley wind (compare Figs. 6.15 and 6.19) and an intensifying mountain wind; which has become established ahead of the squall line near x = -195, -173, and -163 km at this time (10:30 PM); are visible.

The squall line originally was located at x = -131 km (where the streamlines near z = 8 km in Fig. 6.20 jump upward), redeveloped west to x = -141 km, and now is becoming established at -150 km. Figures 6.21 and 6.22 reveal these three sites are comprised of the oldest cell which is weakening rapidly, the strongest cell that has a w_{max} > 11.0 m s^{-1}, and the newest cell whose maximum upward velocity and q_{ci} are still increasing. Downward motion extends from the surface to 6 km beneath the oldest convection and is associated with relatively heavy precipitation while the rain generated in the strongest convection is just beginning to reach the surface. These individual cells moved downstream at only 4-5 m s^{-1} before dissipating while the squall line propagated west at more than 10.2 m s^{-1}.

In addition to showing the vertical motions associated with the three cells discussed above, Fig. 6.21 shows eastward and westward propagating gravity waves in the upper troposphere and lower stratosphere that were produced by

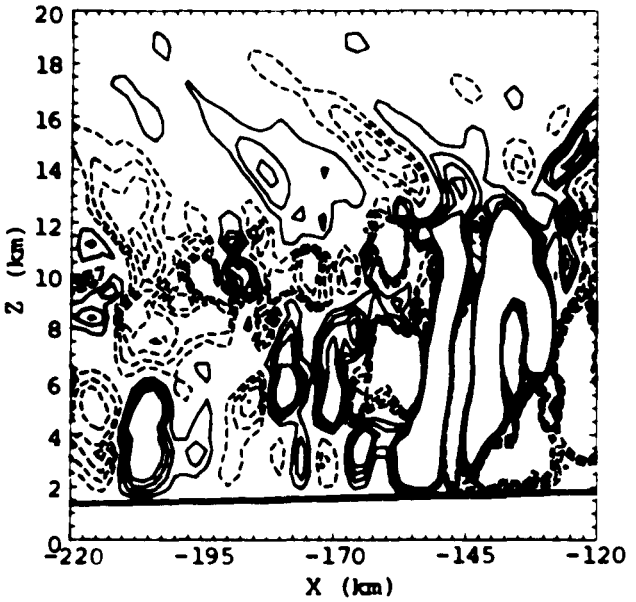

Figure 6.21 As in Figure 6.17 but at 1050 min. The contour interval is 0.125 m s^{-1} and contours are drawn for $|w| \leq 0.50$ m s^{-1}.

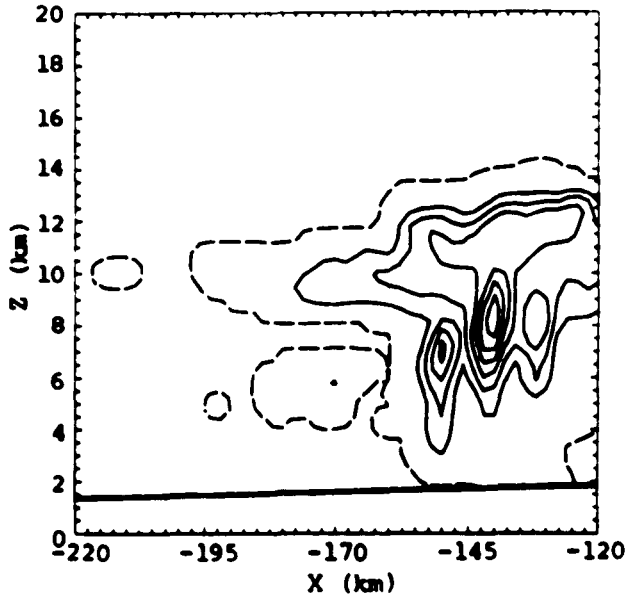

Figure 6.22 As in Figure 6.14 but for 1050 min.

the deep convection and westward propagating gravity waves in the boundary layer ahead of the squall line. The vertical motion field above the boundary layer appeared to result from the interaction of latent heat released in the clouds and propagating gravity waves generated by the squall line. Gravity (buoyancy) waves have been observed in the free troposphere over the Great Plains by Lu et al. (1984) who stated they probably were caused by distant thunderstorms over the Rocky Mountains. Clark and Hauf (1986), Clark et al. (1986), Hauf and Clark (1989), and Redelsperger and Clark (1989) believe that thermal convection in unstable boundary layers produces gravity waves in the overlying free atmosphere and that these waves have a significant impact on the resulting convection. Furthermore, the simulations of Redelsperger and Clark (1989) indicated the interplay of these gravity waves and the underlying boundary layer eddies led to the formation of cumulonimbus over gently sloping terrain in the complete absence of any large-scale forcing.

The gravity waves near the top of the boundary layer are present as ripples from z = 3.5-5 km in the u contours of Fig. 6.19. The upward motion associated with some of these waves caused the cloud that originally developed from a wave about 15 km west of the valley wind/gust front

convergence at x = -119 km to start growing again near -179 km after it had nearly dissipated.

Several gravity waves with a horizontal wavelength near 9 km and phase velocity of 14 m s^{-1}, 10 m s^{-1} relative to the ground, are evident in the stable boundary layer west of the squall line in Fig. 6.21. They are very similar in appearance to the gravity waves, which had a 10 km horizontal wavelength and a 12 ± 5 m s^{-1} horizontal propagation speed, Ley and Peltier (1981) examined in the south central United States that initiated clouds but not thunderstorms and also were apparently generated by earlier deep convection (see their Fig. 1). The waves in Fig. 6.21 are being partially reflected without a significant loss of energy by a relatively thin, almost saturated, conditionally unstable layer near the base of the clouds ahead of the squall line in Fig. 6.22. The Richardson number, R:

$$R = \frac{g/\theta \; \partial\theta/\partial z}{(\partial u/\partial z)^2} \qquad 6.2$$

in this layer generally is positive but in few small areas is negative. In addition, the wind speed near the top of the layer, generally 10-13 m s^{-1}, is only slightly less than the estimated 14 m s^{-1} phase speed of the gravity waves. Lindzen and Tung (1976) found these conditions created an effective duct for gravity waves. The reflectivity of the cloudy layer was calculated to be approximately

80% using the two layer model in Eliassen and Palm (1960). This value is very close to the 85% Lindzen and Tung (1976) stated was necessary for their n=0 mode wave, the one with the longest vertical wavelength, to last just two cycles.

The reinvigorated cloud that originally formed at x = -119 km had moved west to -192 km by 1080 min while slowly growing. Deep convection ensued when the upward motion forced by the valley wind/gust front induced convergence zone moved under this cloud so the preexisting upward motion in the cloud was in phase with that below. This caused the squall line to discretely propagate approximately 25 km to the west about an hour later. Nicholls' (1987) 2D simulation of a tropical squall line also produced small clouds, which may have been caused by traveling gravity waves, at large distances ahead of the gust front. He also noticed that deep convection occurred when the gust front moved underneath these small clouds. Similarly, Schmidt and Cotton (1989) observed that convection was enhanced when the vertical motion fields associated with upper and lower tropospheric gravity waves produced by their simulated squall line came into phase.

The next four sets of figures show how the aforementioned episode of discrete propagation occurred. Figures 6.23-26 display u, streamlines in the frame of reference

moving with the squall line, w, and q_{ci} respectively at 1080 min. Figure 6.23 reveals the maximum wind speed in the gust front was 20.5 m s^{-1}, the valley wind west of the squall line had weakened while the mountain wind had strengthened, and that the strong east winds of the RIJ reached x = -157 km with 4 m s^{-1} west winds only 9 km away. The streamline plot, Fig. 6.24, also shows the relatively strong convergence caused by the easterly winds of the RIJ and the westerly boundary layer winds that feed the squall line. Comparison of Figs. 6.25 and 6.23 implies the upward motion at x = -185 km is due to the valley wind/gust front convergence while that at -174 km results from the rapid increase of wind speed in the gust front itself. The updraft near -192 km is in the cloud of interest which is shown in Fig. 6.26. At 1080 min, the center of this updraft was about 7 km west of the updraft caused by the valley wind/gust front convergence zone.

The strong convergence above the gust front that was generated by the valley wind and the RIJ caused renewed convection in the squall line and led to the intensification and redevelopment of the RIJ 10 km further west in the following twenty minutes (Fig. 6.27). The maximum upward velocity in the new cell exceeded 12.5 m s^{-1} at 1095 min and this brought the streamlines in Fig. 6.28 to near

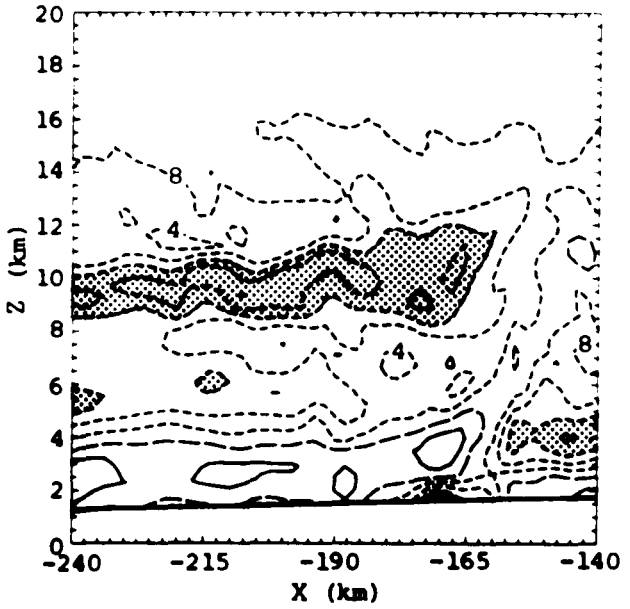

Figure 6.23 As in Figure 6.15 but for 1080 min of the rain and ice simulation.

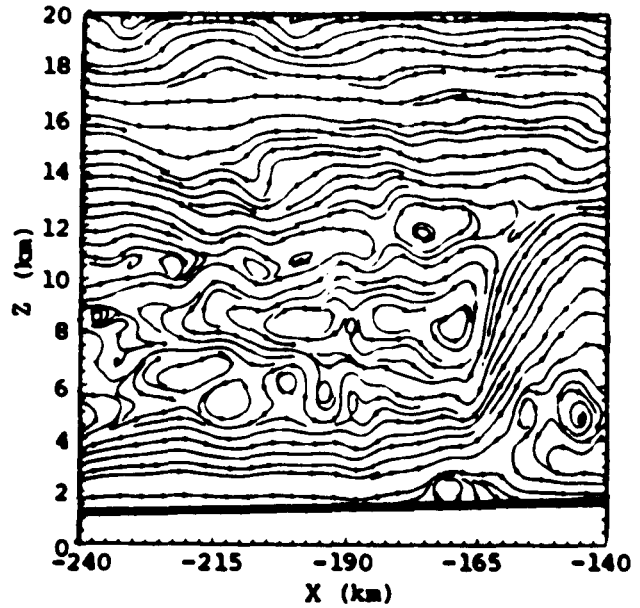

Figure 6.24 As in Figure 6.12 but at 1080 min of the rain and ice simulation.

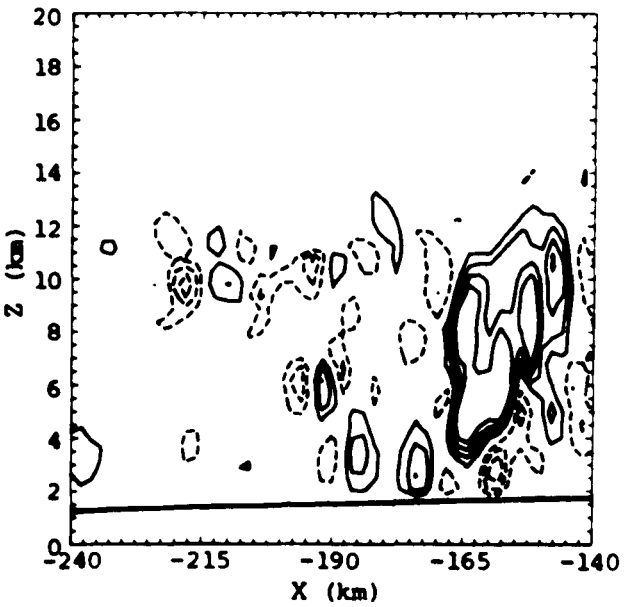

Figure 6.25 Vertical velocity at 1080 min of the rain and ice simulation. The contour interval is 0.50 m s^{-1}. Contours are drawn for $|w| \leq 2$ m s^{-1} with the solid lines showing upward motion and the short-dashed lines downward motion.

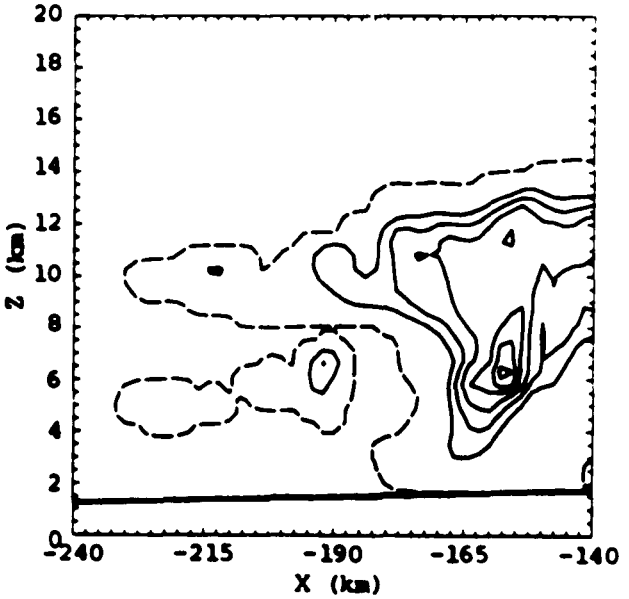

Figure 6.26 As in Figure 6.14 but for 1080 min.

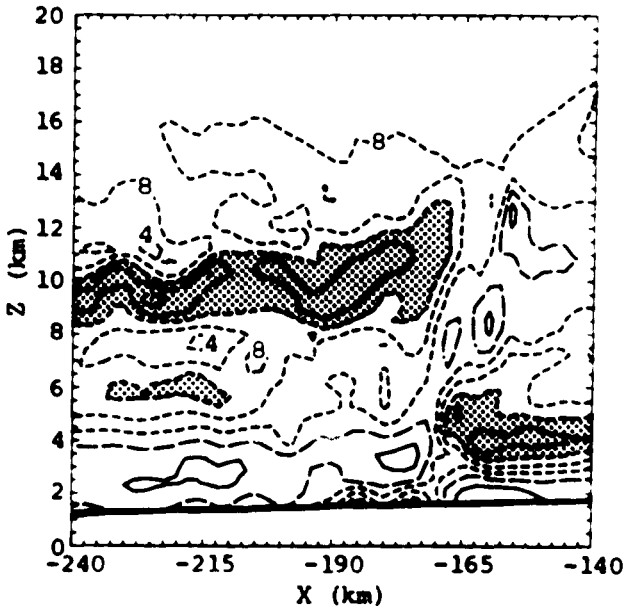

Figure 6.27 As in Figure 6.15 but for 1100 min of the rain and ice simulation.

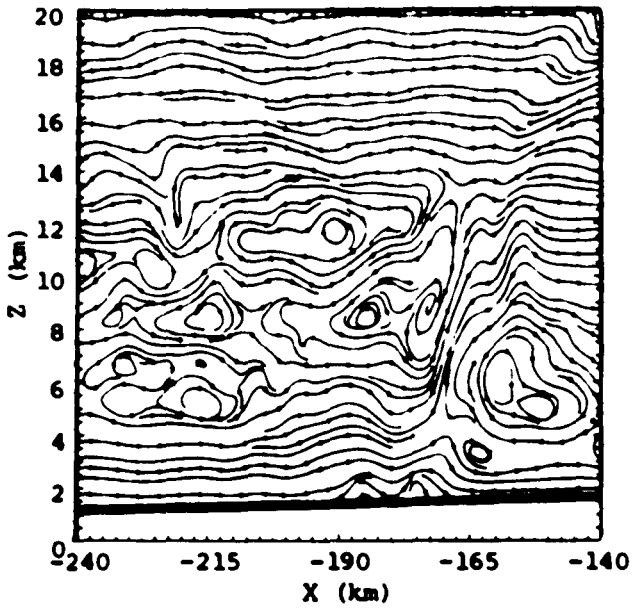

Figure 6.28 As in Figure 6.12 but at 1100 min of the rain and ice simulation.

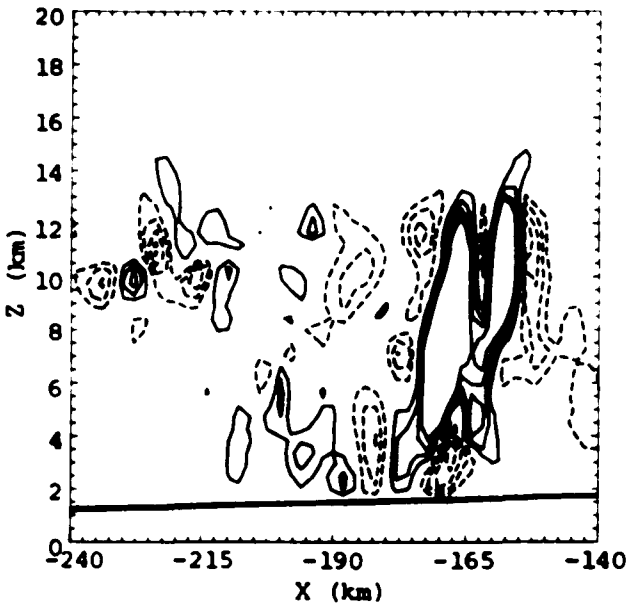

Figure 6.29 As in Figure 6.25 but at 1100 min.

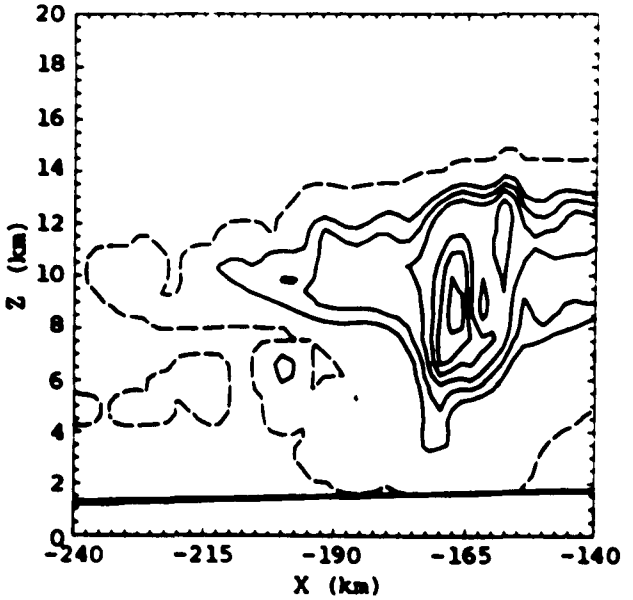

Figure 6.30 As in Figure 6.14 but for 1100 min.

vertical at the squall line. Figures 6.29 and 6.30 show the cell tilted slightly upshear and had a maximum $q_{ci} > 7$ g kg^{-1}. Heavy precipitation was falling from x = -167 to -161 km at this time, 1100 min into the simulation.

The small cumulus under study was located at x = -200 km at 1100 min and had become even smaller (see Fig. 6.29 and 6.30). Only four kilometers separated the maximum upward velocity in the cloud from that induced by the valley wind/gust front convergence. At 1120 min the squall line was about ready to undergo discrete propagation as the two updrafts of interest came into phase near x = -205 km.

The developing cumulonimbus was not aided by convergence associated with the RIJ as it was still more than 20 km to the east as seen in Fig. 6.31 which indicates the low-level westerlies moved up and over the gust front to merge with the air continuing to move up the slope behind the squall line. Deep convection did not develop from the forced ascent of the boundary layer air because the surface outflow never was deep enough to lift the air to the LFC (see Fig. 6.32). This is in contrast to the findings of Droegemeier and Wilhelmson (1985) who showed new convection did occur as the result of frontal lifting by the simulated gust front. However, as previously stated, convergence of the valley wind and the RIJ above the gust front occasion-

ally seemed to initiate new cells beneath the remnants of older, decayed cells.

Comparison of Figs 6.32 and 6.33 with 6.28 and 6.29, respectively, shows the squall line updraft weakened while the one in the growing thunderstorm strengthened. In fact, downward motion has replaced upward motion at altitudes below 4 km in the squall line. The changes in q_{ci} evidenced in Figs. 6.34 and 6.30 were a direct result of these changes in the vertical motion field.

Discrete propagation to x = -210 km was complete by 1140 min, 12 AM model time. The RIJ had not yet developed west to the new location of the squall line while the mountain wind now extended about 50 km ahead of the squall line (see Fig. 6.35). At this instant, the squall line was located at the upward jump in the streamlines near x = -210 km in Fig. 6.36 which coincides with the area of large upward velocities in Fig. 6.37 and high q_{ci} in Fig. 6.38.

The upward jump in the streamlines to the immediate west was caused by a developing cumulonimbus, the updraft at about x = -222 km in Fig. 6.37, that became the squall line in the ensuing half hour. The evolving deep convection may have been initiated either by convergence at the leading edge of the gust front and/or by the last of a series of three westward propagating gravity waves, the

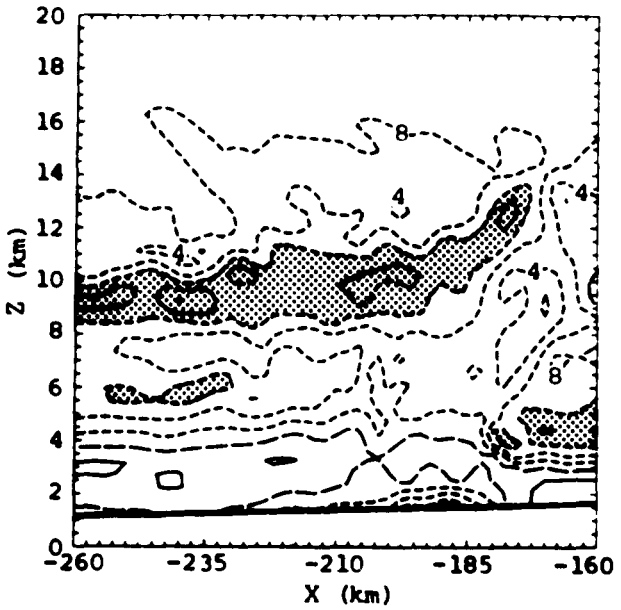

Figure 6.31 As in Figure 6.15 but for 1120 min of the rain and ice simulation.

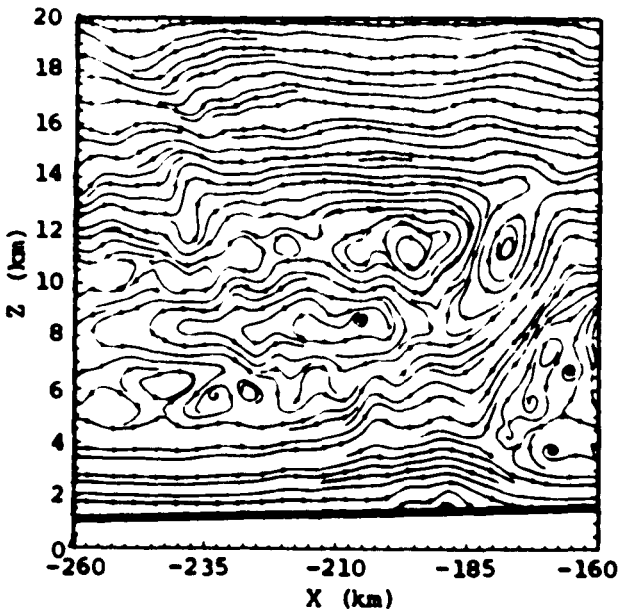

Figure 6.32 As in Figure 6.12 but at 1120 min of the rain and ice simulation.

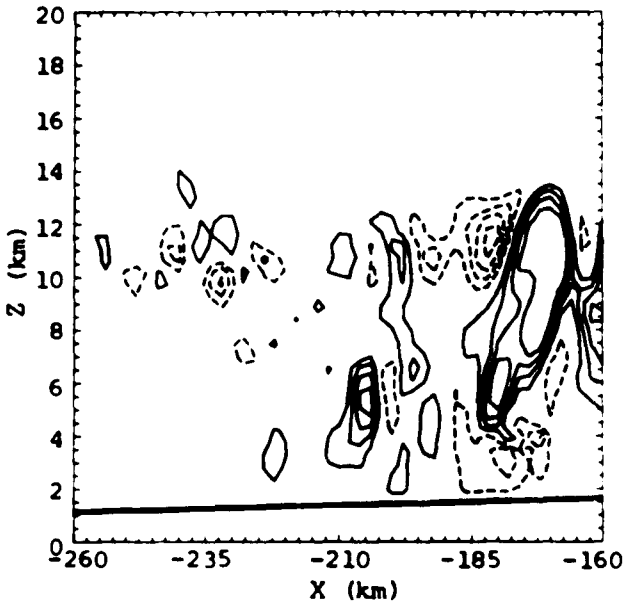

Figure 6.33 As in Figure 6.25 but at 1120 min.

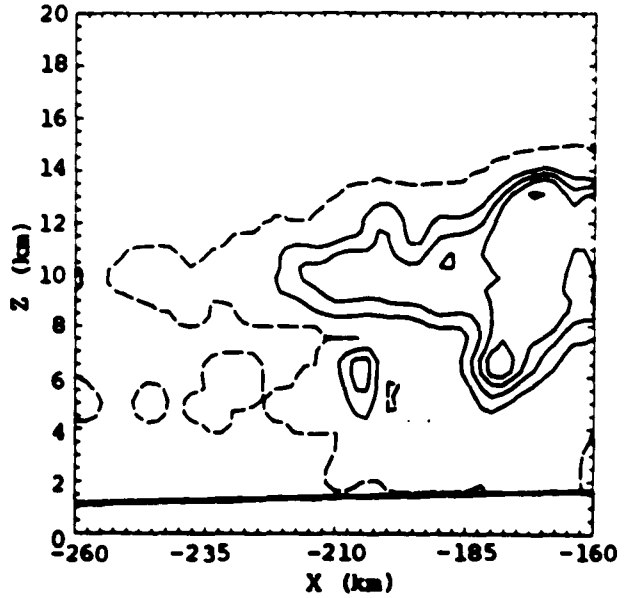

Figure 6.34 As in Figure 6.14 but for 1120 min.

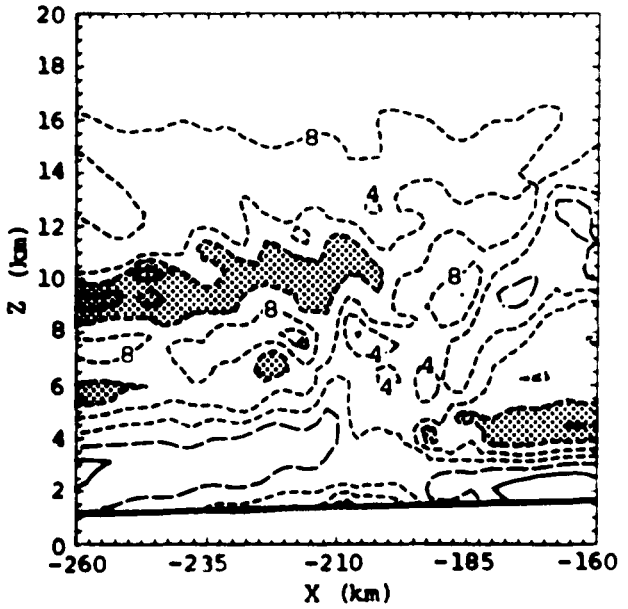

Figure 6.35 As in Figure 6.15 but for 1140 min of the rain and ice simulation.

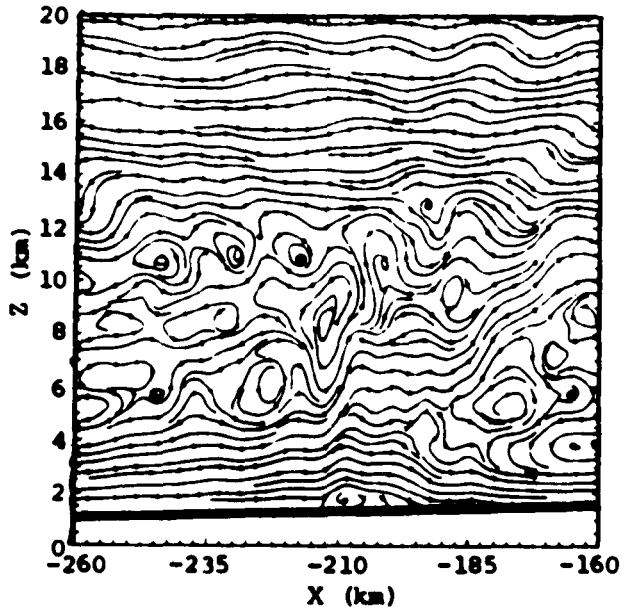

Figure 6.36 As in Figure 6.12 but at 1140 min of the rain and ice simulation.

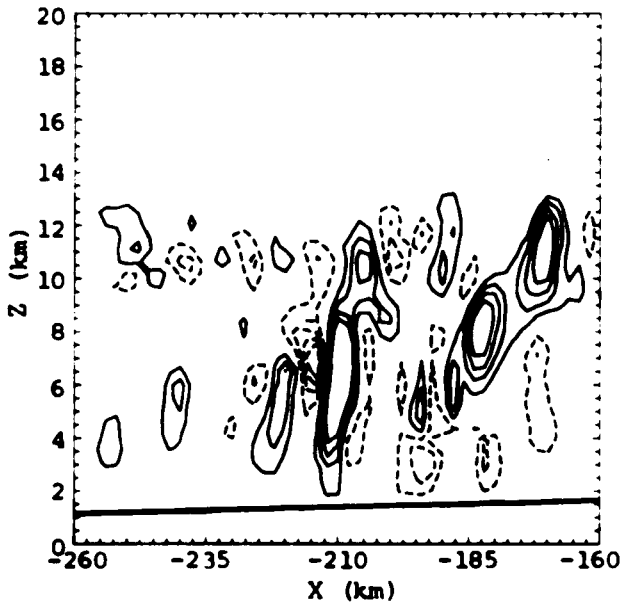

Figure 6.37 As in Figure 6.25 but at 1140 min.

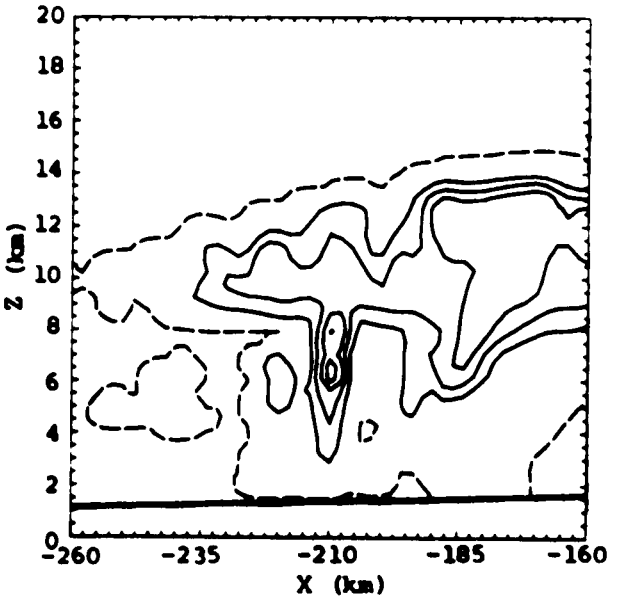

Figure 6.38 As in Figure 6.14 but for 1140 min.

ripples in the u contours of Fig. 6.35, that are associated with the areas of upward motion in Fig. 6.37 west of the squall line. These waves are traveling in the duct that was discussed earlier.

Recent simulations by several different groups of researchers suggest propagating gravity waves may play an important role in the evolution of squall line convection. For instance, ducted gravity waves apparently had an important part in the organization and maintenance of the simulated midlatitude squall line of Schmidt and Cotton (1989). Tripoli and Cotton (1989b) stated new cells in their control run were generated by low-level convergence ahead of the gust front but when they reduced the winds in the control case by 50%, new convection sometimes developed ahead of the system in response to propagating gravity waves which appeared to be ducted by the leading anvil of the squall line. Crook and Moncrieff (1988) also noted that travelling gravity waves could initiate new cells 10-15 km in advance of their modelled squall line and its associated low-level cold pool (density current) and they found that if a larger scale convergence was present, deep convection could be maintained without a cold pool. Likewise, Balaji and Clark (1988) established that discrete propagation, with new cells forming 12-15 km away, could take place in

the absence of a spreading low-level cold pool.

An examination of Figs. 6.39-6.42 shows how the ζ field associated with the RIJ was evolving at 1120 min. At that time, the squall line was located at approximately x = -182 km, the RIJ extended west to -180 km in the $3.5 \leq z \leq 5$ km layer, and the winds ahead of the squall line in this layer were either from the west or were much weaker (Fig. 6.39). The ζ field indicated the jet was associated with a sheet of positive ζ that stretched westward from the convergence zone near the summit to almost directly beneath the squall line updraft (Fig. 6.40). The eastern portion of this sheet may have been maintained by the positive ζ tendency generated in the convergence zone by the two advection terms and the θ induced buoyancy gradient. Rising motion carried the negative ζ gradient created over the eastern slope by the valley wind upward producing a positive tendency which also was created by the positive θ gradient across the zone. The resultant positive horizontal ζ gradient was then advected to the west.

Comparison of Figs. 6.41 and 6.42; which show the ζ tendency neglecting the stress and Rayleigh friction terms and the ζ tendency due to the vertical advection and θ terms, respectively; indicates that most of the negative and positive ζ tendency found under the squall line updraft

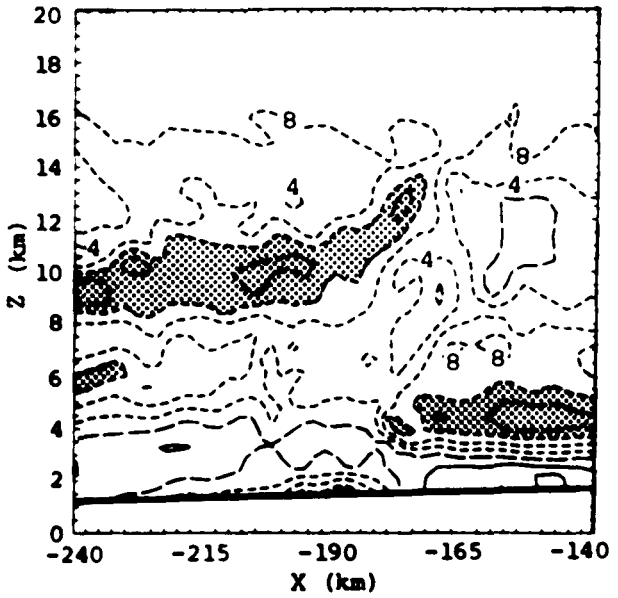

Figure 6.39 As in Figure 6.15 but at 1120 min and for -240 ≤ x ≤ -140 km.

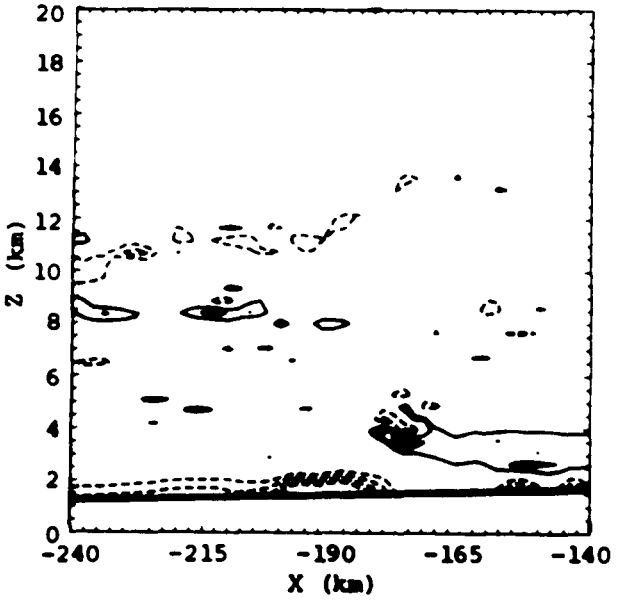

Figure 6.40 Vorticity at 1120 min of the rain and ice simulation. The contour interval is 0.01 s^{-1}. Contours are drawn for $|\zeta| \leq 0.04$ s^{-1} with the solid lines showing positive (counterclockwise) vorticity and the dashed lines negative vorticity.

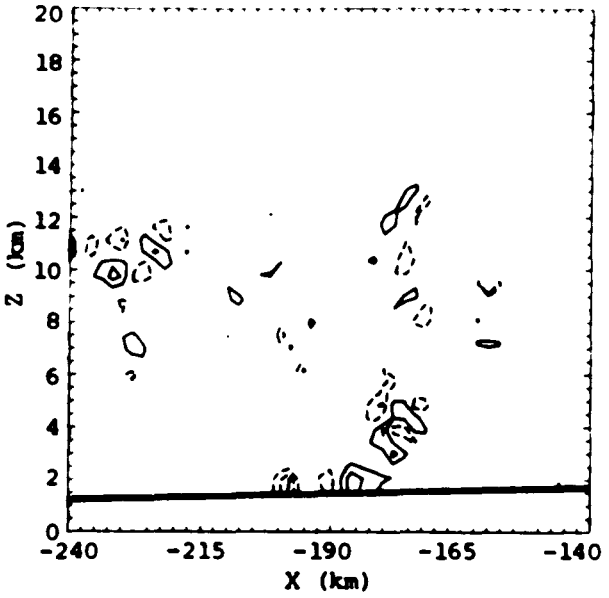

Figure 6.41 Vorticity tendency (neglecting the stress and Rayleigh friction terms) at 1120 min of the rain and ice simulation. The contour interval is 2 X 10^{-5} s^{-2} with the solid lines showing positive values and the dashed lines negative values.

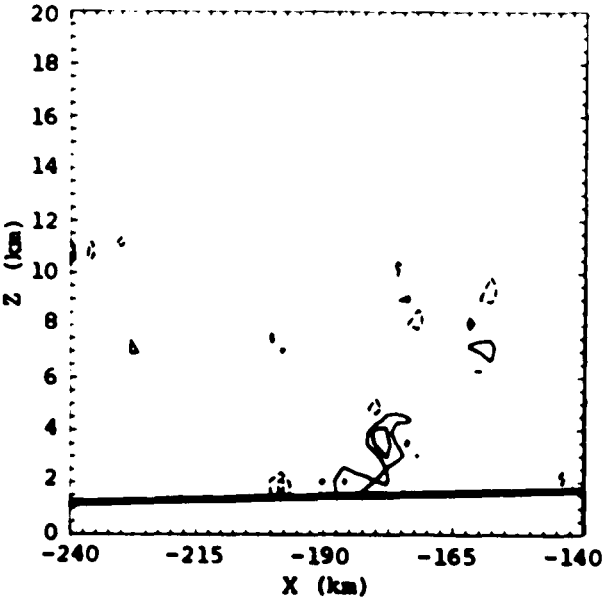

Figure 6.42 Vorticity tendency due to the potential temperature and vertical advection terms at 1120 min of the rain and ice simulation. The contour interval is 2 X 10^{-5} s^{-2} with the solid lines showing positive values and the dashed lines negative values.

(i.e., from x = -179 to -183 km) comes from the θ and vertical advection terms. Horizontal advection accounts for nearly all the rest and for the areas of negative and positive tendency just to the east in Fig. 6.41. The positive ζ tendency and positive ζ at $-179 \leq x \leq -183$ km were generated by the relatively short-lived mesoγ-scale downdrafts of the deep convection which created a positive θ gradient through the squall line via subsidence induced warming and advected the preexisting, positive, vertical ζ gradient downward. On the other hand, the negative ζ tendency and negative ζ just above were produced in a relatively brief period by the updrafts of the deep convection which lifted the positive vertical ζ gradient upward and created a negative θ gradient at the rear of the updraft (the updraft air was slightly warmer than the air to the east).

The same basic features are evident at 1240 min in Figs. 6.43-46. The RIJ and the ζ field associated with the RIJ developed nearly 90 km further westward (see Figs. 6.43 and 6.44) in the intervening two hours. Furthermore, comparison of Figs. 6.45 and 6.46 indicates most of the negative and positive ζ tendency in the vicinity of the squall line again resulted from the θ and vertical advection terms, via the mechanisms previously discussed, with most of the remainder accounted for by horizontal advection.

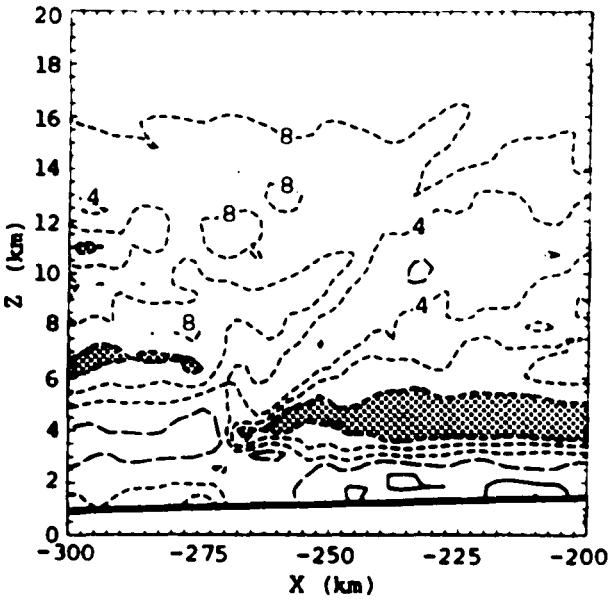

Figure 6.43 As in Figure 6.15 but for 1240 min of the rain and ice simulation.

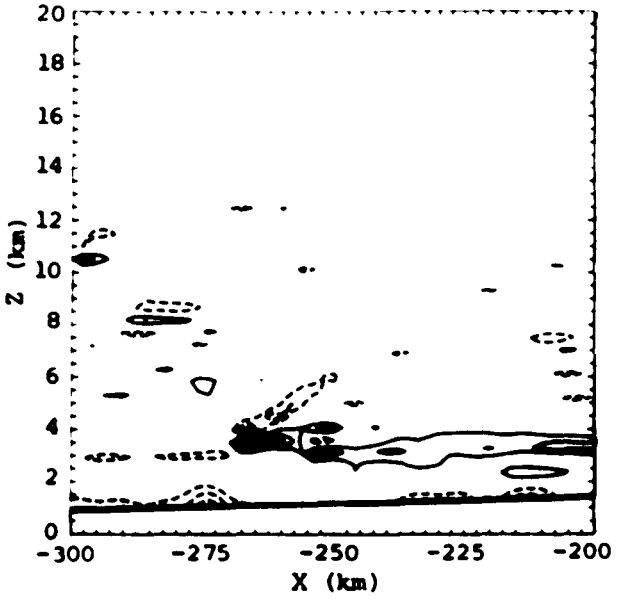

Figure 6.44 As in Figure 6.40 but for 1240 min.

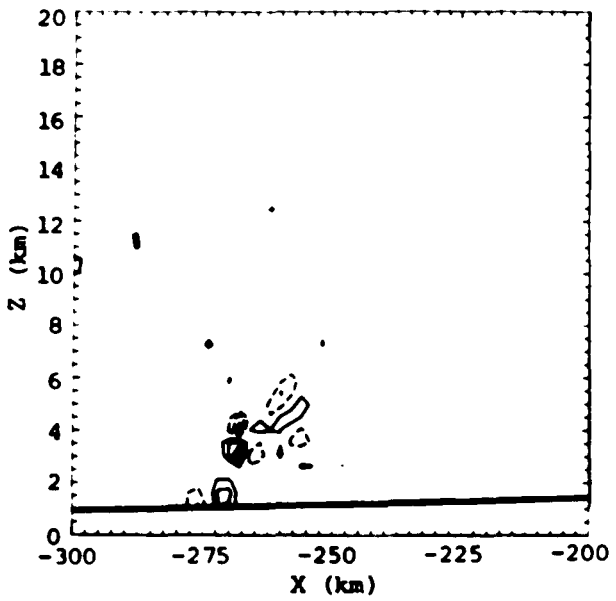

Figure 6.45 As in Figure 6.41 but for 1240 min.

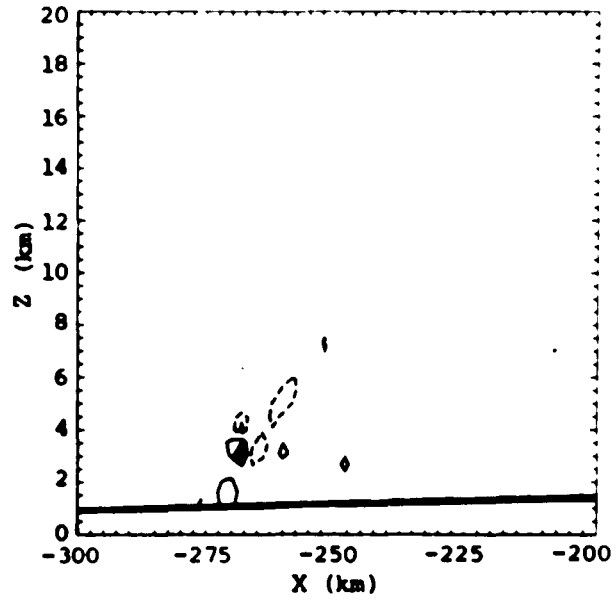

Figure 6.46 As in Figure 6.42 but for 1240 min.

Figure 6.47 is a schematic diagram that shows how the θ and vertical advection terms of the ζ tendency equation (6.1) appeared to create the regions of negative and positive tendency in the squall line which in turn produced the ζ field connected with the RIJ.

Several westward propagating gravity waves could be seen (not shown) late in the simulation at altitudes below 6.0 km west of the squall line. The upward motion associated with some of these waves appeared to cause renewed cloud growth in the $4.0 \leq z \leq 6.5$ km layer. However, the squall line rapidly weakened after 1200 min with w_{max} declining to less than 2.5 m s^{-1} by 1250 min with the remaining convection tilting markedly upshear. Weakening seemed to be due to the near complete elimination of positive buoyancy in the boundary layer coupled with a large reduction in low-level wind shear ahead of the squall line that was caused by the continued decline of the valley wind and ascendence of the mountain wind.

These findings imply the demise of the three observed tropical squall lines at the Gulf of California or before dawn local time also may have been caused by the combination of reduced instability and decreased low-level wind shear. Reduced instability probably resulted from the relatively low temperatures found over the gulf and over

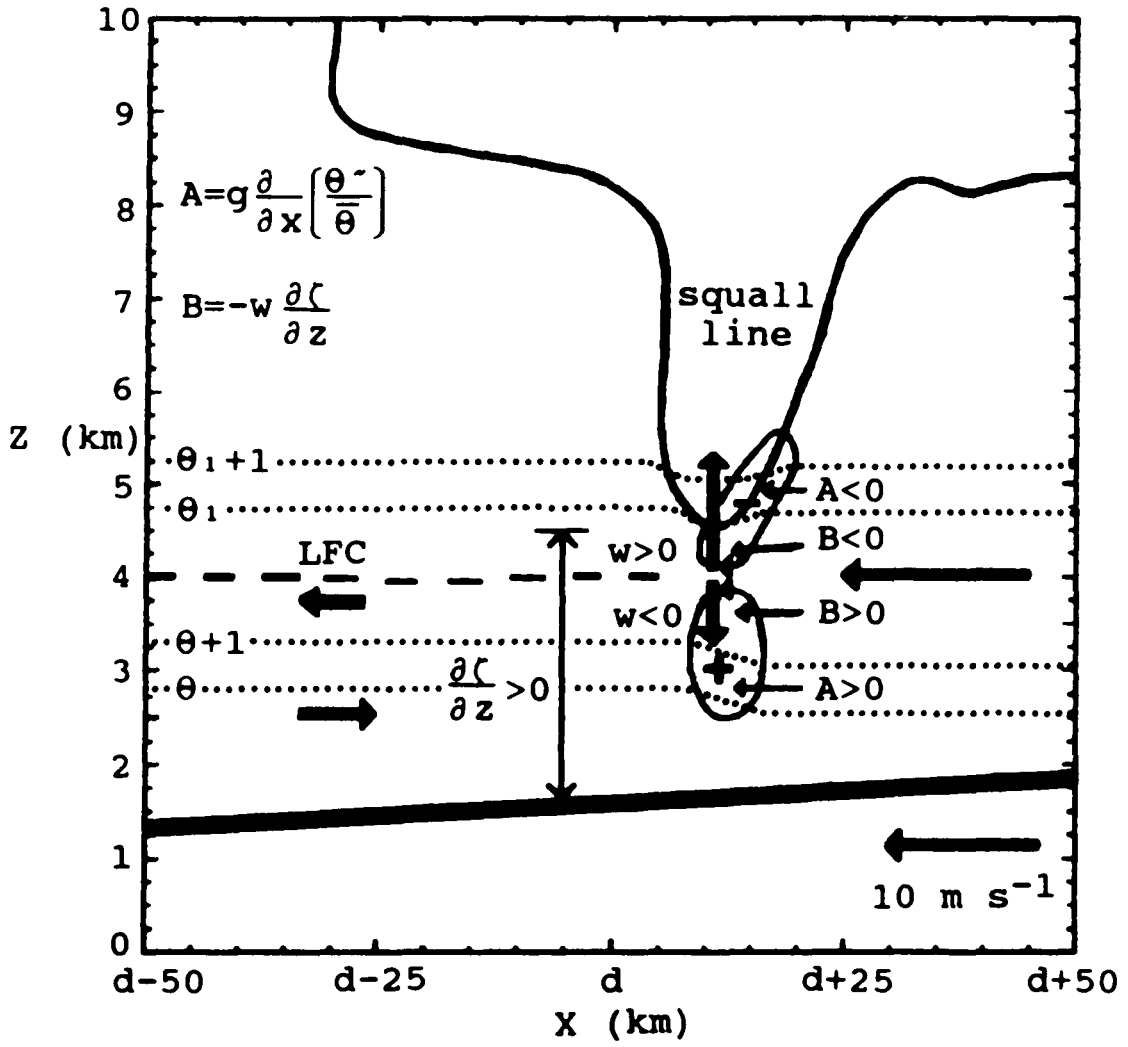

Figure 6.47 Schematic diagram showing how the creation of horizontal potential temperature gradients (A) and the advection of vertical vorticity gradients by the vertical component of the wind (B) may have produced the vorticity field associated with the rear inflow jet in the latter part of the simulation. The dotted lines are isotherms, the thick arrows are wind vectors, the dashed line is the level of free convection, and the thin solid line encompassing the squall line represents regions with a cloud water and ice mixing ratio ≥ 1 g kg^{-1}.

the land at night. Decreased low-level wind shear was brought about by the weakening or elimination at night of the sea breeze near the coast and the valley wind further inland and by the formation of the land breeze near the coast and the mountain wind farther east.

Some additional notable features of the rain and ice simulation include the following. No clouds formed over the lower eastern slope in this run or in R. In fact, the easternmost cloud was located at approximately x = 60 km and no deep convection developed east of the peak. The maximum changes in temperature and pressure across the gust front were only about 2°C (the average was near 1°C) and 0.1 kPa, respectively. The q_v contours were depressed closer to the surface behind the squall line indicative of subsidence which appeared to result from precipitation induced downdrafts as suggested by Brown (1979) and not from a spreading density current as proposed by Miller and Betts (1976). Furthermore, a well developed density current did not form in this simulation or in R just as in the so-called unicell squall lines of Dudhia et al. (1987), Nicholls et al. (1988), and Lafore and Moncrieff (1989). In addition, the RIJ never descended to the surface as reported by Redelsperger and Lafore (1988) and Lafore and

Moncrieff (1989) in their studies of West African tropical squall lines. The surface outflow and RIJ remained separate entities throughout the simulation.

CHAPTER 7

SUMMARY AND DISCUSSION

Three squall lines that developed over southern Arizona and northwestern Mexico possessed almost all the properties of tropical squall lines. The two largest and most intense squall lines formed on the 16-17 and 17-18 July 1984 (1 and 2) and the other on 2-3 August 1986 (3). The first thunderstorms developed in the afternoon over the mountains along the Arizona-New Mexico border and over the Sierra Madre Occidental. These thunderstorms eventually grew into several mesoβ-scale clusters which became organized into squall lines east of the Tucson metropolitan area in the late afternoon-early evening and tracked across Tucson around dusk. Satellite imagery, CG lightning strike data, and surface observations indicated the squall lines were composed of several mesoβ thunderstorm clusters at all times and that they moved from east to west by discrete propagation. The average propagation velocity was approximately 12 m s^{-1} which was greater than the environmental winds at all levels below 20 kPa from 16-18 July 1984 and throughout the entire troposphere on 2-3 August 1986. Consequently, most of the anvil clouds lagged behind the lines. The squall lines continued moving westward most of

the night over the sparsely populated deserts of southwestern Arizona and western Sonora and dissipated either upon reaching the Gulf of California or before dawn.

Radiosonde observations taken at Tucson just before the appearance of the squall lines found 3-8 m s^{-1} west to northwest winds in the boundary layer and 5-10 m s^{-1} east-northeast to southeast winds above. Nearly all the environmental wind shear was confined to the lowest 2.5 km with very little shear at higher altitudes. The soundings also showed moist, high θ_e, potentially warm air beneath a relatively thick layer of extremely dry, low θ_e, potentially cool air. VAS 6.7 μm images showed this dry air was part of a relatively narrow east-west band that extended westward across the Continental Divide to about the Gulf of California. The length of each squall line may have been determined, at least in part, by the width of the dry air bands above the Continental Divide. The dry over moist stratification also was associated with the development of severe thunderstorms and damaging downburst winds. The low-level wind shear seemed to be required for both the formation and propagation of the squall lines. When the dry layer was present during the 1984-88 period and the shear was much weaker or absent, squall lines did not develop.

The weather experienced at any given location in the path of the squall lines was similar. First, thunderstorm formation was suppressed until the squall lines approached. Gust fronts from strong to severe thunderstorms then blew in carrying dust-laden air on winds that commonly reached 20 m s^{-1} and may have exceeded 30 m s^{-1}. These thunderstorms typically were 14-16 km high and in a few instances were 17-18 km high where satellite-derived cloud top temperatures were less than -80°C. Soon after the arrival of the gust fronts some locations observed a brief period, a few minutes to an hour, of heavy rain that brought from 1-75 mm of rain. Light rain, which probably was caused by the development of a mesoscale updraft/cyclonic circulation in the anvil cloud, ensued as the anvil cloud moved overhead and lasted from 3 to 6 hours bringing up to an additional 15 mm of precipitation. In each case, the midlevel cyclonic circulation persisted long after the squall line and its accompanying high clouds had dissipated and could be seen cyclonically rotating the following day. The two from July 1984 appeared to initiate thunderstorms as they tracked across the mountains along the Pacific coast.

The midlevel cyclonic circulation also may have aided the development of thunderstorms, some of which were severe, at the periphery of the anvil cloud late in the even-

ing and at night. This may partly account for the nocturnal thunderstorm maximum observed in portions of central Arizona (Balling and Brazel 1987). Other factors which may help explain the nocturnal maximum are the arrival of westward propagating squall lines from eastern Arizona and of other MCSs late in the evening and at night.

Tropical squall lines occur rather infrequently in Arizona, 1-3 per season in 1984-88. This is due to the anomalous synoptic-scale circulation, strong ridge over the western one-third of the United States and deep trough over the eastern United States, required to generate conditions favorable for their development. The midtropospheric ridge centered to the north of southern Arizona causes easterly winds aloft, brings dry midlevel air to southern Arizona and northern Sonora, and creates an anomalously warm lower troposphere which causes abnormally low 85 kPa heights and a deeper layer of stronger west to northwest winds that produces the necessary low-level wind shear.

The MCS described by Hales (1975) that brought wind gusts of 31 m s^{-1} to western Arizona and southeastern California and up to 79 mm of rain may have developed from a tropical squall line. Given the relatively frequent occurrence of MCSs along the west coast of Mexico, squall lines probably are more common there than in Arizona. Tropical

cyclones, e.g., Hurricane Waldo in October 1985, occasionally develop from these MCSs when they move off the coast of Mexico over the very warm water of the eastern north Pacific.

A 2D nonhydrostatic numerical model simulated the formation and growth of a squall line that possessed many of the features observed in the tropical squall lines of southern Arizona and northwestern Mexico. Solar heating of the elevated terrain in the model caused upslope winds to develop on both the eastern and western slopes and led to the formation of a strong low-level convergence zone over the summit which ultimately initiated moist convection. The squall line evolved from the fourth relatively intense cell that formed over the convergence zone and then drifted downstream. The first three were simply advected to the west where they eventually dissipated. However, they left behind a relatively moist midtroposphere. A period of intense convection from 866-884 min (7:26 to 7:44 PM model time) marked the beginning of the squall line which developed several hours later than the observed tropical squall lines in an environment with significantly higher humidities aloft.

The squall line travelled 232.5 km from 870 to 1240 min at an average speed of 10.5 m s^{-1} while the three docu-

mented tropical squall lines propagated at about 12 m s^{-1}. This 10.5 m s^{-1} propagation velocity is similar to the 10-15.5 m s^{-1} propagation speeds observed in other tropical squall lines by Zipser (1969, 1977), Miller and Betts (1976), Betts et al. (1976), Mansfield (1977), Barnes and Sieckman (1984), and Chong et al. (1987). Furthermore, this result is within the 7-18 m s^{-1} range of propagation speeds recorded in other numerical simulations of tropical squall lines by Raymond (1984), Bolton (1984), Pointin (1985), Dudhia et al. (1987), Nicholls (1987), Redelsperger and Lafore (1988), Nicholls et al. (1988), and Lafore and Moncrieff (1989).

The squall line moved west by translation of preexisting cells and discrete propagation wherein new cells would develop at distances of 10-25 km ahead of the old ones. Discrete propagation accounted for almost 40% of the total distance travelled by the RI squall line. Just after the squall line developed, it seemed to take place as the result of convergence between the valley wind and the gust front and/or RIJ. Later, during the mature phase of the squall line, discrete propagation occurred when propagating internal gravity waves generated by the deep convection moved downstream and formed small clouds near the top of the boundary layer. These clouds then became cumulonimbus

when upward motion in the boundary layer caused by the valley wind/gust front convergence zone and/or possibly westward propagating gravity waves moved into phase with the upward motion in the clouds. Frontal lifting by the gust front alone did not cause discrete propagation because the surface outflow never was deep enough to lift the low-level air to the LFC. The observed squall lines appeared to dissipate and the simulated one to weaken because of the combined effects of reduced instability and decreased low-level wind shear.

The wind profile above the western slope during the initiation and growth of the modelled squall line had strong low-level wind shear with weak shear aloft and was very similar to the shear profiles recorded by the Tucson NWS RAOBs taken prior to the three documented squall lines. This profile (weak shear aloft) was similar to the ones used by Dudhia et al. (1987), Nicholls et al. (1988), and Lafore and Moncrieff (1989) in their unicell squall line simulations which produced analogous results. Their experiments also did not generate a well-developed cold pool/density current but did produce relatively strong, long-lived squall lines with near vertical updrafts and high cloud tops that moved at nearly the same speed, 11-13 $m\ s^{-1}$.

Changes in the vorticity field brought about by the deep convection at the squall line caused the winds near the LFC to accelerate toward the west and produced a rear inflow jet, a feature which has not yet been observed in connection with the tropical squall lines of southern Arizona and northwestern Mexico. Consequently, the simulated RIJ may or may not bear any resemblance to a real RIJ, assuming one exists.

Early in the life of the squall line, the creation of horizontal θ gradients by the mesoγ-scale updrafts and downdrafts of the deep convection and advection of horizontal ζ gradients by u played the most important parts in the generation of the ζ field (negative ζ above the LFC and positive below) of the RIJ. For a few hours after the initiation of the squall line, the vertical advection term of the ζ tendency equation was important only at the convergence zone where it helped establish and maintain the eastern end of the RIJ. However, later the negative ζ tendency and ζ above the LFC were generated by the updrafts of the deep convection which advected the positive ζ gradient upward and produced negative horizontal θ gradients (the updrafts had a slightly higher θ than the air trailing the deep convection). Conversely, the downdrafts associated with the deep convection produced a positive ζ ten-

dency and positive ζ below the LFC primarily by creating positive horizontal θ gradients through subsidence induced warming and by the downward advection of the positive ζ gradient. The advection of horizontal ζ gradients by u helped extend the ζ field of the RIJ further west and helped maintain the eastern part of the jet by advecting the positive ζ gradient to the west of the convergence zone farther west. The other terms in the vorticity tendency equation (the stress and Rayleigh friction terms were not considered) did not appear to play a significant role in either the creation or maintenance of the vorticity field associated with the RIJ.

The results of the rain and ice run (RI) were particularly encouraging. However, more realistic simulations might be obtained by implementing homogeneous nucleation of liquid water to ice at temperatures near -40°C and by incorporating an improved surface heating routine which allows for longitudinal variations in the solar flux and the presence of clouds. Elimination of the specified surface cooling in favor of a surface energy and water balance routine for the land and for the oceans should help produce a better simulation as should the elimination of known errors, e.g., the switched slopes in the solar flux equation (4.19), and the replacement of outdated algorithms,

e.g. the longwave radiation scheme which has been updated in the latest version of the model. Increasing the height of the peak and the slope of the topography near the peak to match those of the actual mountains together with the addition of small peaks to the western slope might also cause the model squall line to form several hours earlier in the day in agreement with observations. Similarly, Tripoli and Cotton (1989a) noted the first thunderstorms in their numerical experiment formed later in the day than observed. Furthermore, they believe this was due to the absence of smaller-scale mountain peaks in their idealized topographic profile.

These improvements to the model may help decide what role, if any, dry midlevel air plays in the initiation and growth of tropical squall lines in Arizona. The importance of the dry air aloft could not be resolved in this limited set of experiments because both the R and RI squall lines developed under relatively moist conditions aloft. While this suggests the dry air may not have an important role, it is possible that a more realistic tropical squall line will develop under dry midtropospheric air when the model is rerun with the altered initial conditions and improved physics.

Tropical squall lines of the Arizona monsoon can only develop and exist in a very limited geographic area bounded in the east by the Continental Divide and in the west by the Gulf of California, coastal mountain ranges, and Mojave desert. As a result, they have a relatively brief lifetime, usually less than half a day. These squall lines also develop under anomalous but identifiable circumstances and therefore should be predictable. Ongoing research is attempting to answer many questions concerning these systems by gathering new observations and by conducting additional 2D numerical simulations with different vertical profiles of wind and moisture at higher vertical and horizontal resolutions. Three-dimensional experiments may also be considered at some future date.

LIST OF REFERENCES

Adang, T. C., and R. L. Gall, 1989: Structure and dynamics of the Arizona monsoon boundary. Mon. Wea. Rev., 117, 1423-1438.

Arakawa, A., 1966: Computational design for long-term numerical integration of the equations of fluid motion: two-dimensional incompressible flow. Part I. J. Comput. Phys., 1, 119-143.

Aspliden, C. I., Y. Tourre and J. B. Sabine, 1976: Some climatological aspects of west African disturbance lines during GATE. Mon. Wea. Rev., 104, 1029-1035.

Asselin, R., 1972: Frequency filter for time integrations. Mon. Wea. Rev., 100, 487-490.

Balaji, V., and T. L. Clark, 1988: Scale selection in locally forced convective fields and the initiation of deep cumulus. J. Atmos. Sci., 45, 3188-3211.

Balling, R. C., Jr., and S. W. Brazel, 1987: Diurnal variations in Arizona monsoon precipitation frequencies. Mon. Wea. Rev., 115, 342-346.

Barnes, G. M., and K. Sieckman, 1984: The environment of fast- and slow-moving tropical mesoscale convective cloud lines. Mon. Wea. Rev., 112, 1782-1794.

Betts, A. K., R. W. Grover and M. W. Moncrieff, 1976: Structure and motion of tropical squall-lines over Venezuela. Quart. J. Roy. Meteor. Soc., 102, 395-404.

Bluestein, H. B., and M. H. Jain, 1985: Formation of mesoscale lines of precipitation: severe squall lines in Oklahoma during the spring. J. Atmos. Sci., 42, 1711-1732.

Bolton, D., 1980: The computation of equivalent potential temperature. Mon. Wea. Rev., 108, 1046-1053.

____, 1984: Generation and propagation of African squall lines. Quart. J. Roy. Meteor. Soc., 110, 695-721.

Brown, J. M., 1979: Mesoscale unsaturated downdrafts driven by rainfall evaporation: a numerical study. J. Atmos. Sci., 36, 313-338.

Chong, M., P. Amayenc, G. Scialom and J. Testud, 1987: A tropical squall line observed during the COPT 81 experiment in West Africa. Part 1: kinematic structure inferred from dual-Doppler radar data. Mon. Wea. Rev., 115, 670-694.

Clark, T. L., 1977: A small-scale dynamic model using a terrain-following coordinate transformation. J. Comput. Phys., 24, 186-215.

____, 1979: Numerical simulations with a three-dimensional cloud model: lateral boundary condition experiments and multicellular severe storm simulations. J. Atmos. Sci., 36, 2191-2215.

____, and R. D. Farley, 1984: Severe downslope windstorm calculations in two and three spatial dimensions using anelastic interactive grid nesting: a possible mechanism for gustiness. J. Atmos. Sci., 41, 329-350.

____, and R. Gall, 1982: Three-dimensional numerical model simulations of airflow over mountainous terrain: a comparison with observations. Mon. Wea. Rev., 110, 766-791.

____, and T. Hauf, 1986: Upshear cumulus development: a result of boundary layer/free atmosphere interactions. Preprints, 23rd Conf. on Radar Meteor. and the Conf. on Cloud Physics, Snowmass, Co., Amer. Meteor. Soc., J18-J21.

____, ____ and J. P. Kuettner, 1986: Convectively forced internal gravity waves: results from two-dimensional numerical experiments. Quart. J. Roy. Meteor. Soc., 112, 899-925.

____, W. D. Hall and P. Smolarkiewicz, 1987: Documentation of The Clark's Anelastic Model: Version G2TC30. Nat. Center for Atmos. Res., Boulder, Co. 80307, 149 pp.

____, and W. R. Peltier, 1977: On the evolution and stability of finite-amplitude mountain waves. J. Atmos. Sci., 34, 1715-1730.

Cotton, W. R., R. L. George, P. J. Wetzel and R. L. McAnelly, 1983: A long-lived mesoscale convective complex. Part I: The mountain-generated component. Mon. Wea. Rev., 111, 1893-1918.

Crook, N. A., and M. W. Moncrieff, 1988: The effect of large-scale convergence on the generation and maintenance of deep moist convection. J. Atmos. Sci., 45, 3606-3624.

Droegemeier, K. K., and R. B. Wilhelmson, 1985: Three-dimensional numerical modeling of convection produced by interacting thunderstorm outflows. Part I: control simulation and low-level moisture variations. J. Atmos. Sci., 42, 2381-2403.

Dudhia, J., M. W. Moncrieff and D. W. K. So, 1987: The two-dimensional dynamics of West African squall lines. Quart. J. Roy. Meteor. Soc., 113, 121-146.

Dutton, J. A., and G. H. Fichtl, 1969: Approximate equations of motion for gases and liquids. J. Atmos. Sci., 26, 241-254.

Eliassen, A., and E. Palm, 1961: On the transfer of energy in stationary mountain waves. Geofysiske Publikasjoner., 22, 3, 23 pp.

Fortune, M., 1980: Properties of African squall lines inferred from time-lapse satellite imagery. Mon. Wea. Rev., 108, 153-168.

Fritsch, J. M., and R. A. Maddox, 1981: Convectively driven mesoscale weather systems aloft. Part 1: Observations. J. Appl. Meteor., 20, 9-19.

____, R. J. Kane and C. R. Chelius, 1986: The contribution of mesoscale convective weather systems to the warm-season precipitation in the United States. J. Climate and Appl. Meteor., 25, 1333-1345.

Gamache, J. F., and R. A. Houze Jr., 1982: Mesoscale air motions associated with a tropical squall line. Mon. Wea. Rev., 110, 118-135.

____, and ____, 1985: Further analysis of the composite wind and thermodynamic structure of the 12 September GATE squall line. Mon. Wea. Rev., 113, 1241-1259.

Goodman, S. J., and D. R. MacGorman, 1986: Cloud-to-ground lightning activity in mesoscale convective complexes. Mon. Wea. Rev., 114, 2320-2328.

Hales, J. E., Jr., 1975: A severe southwest desert thunderstorm: 19 August 1973. Mon. Wea. Rev., 103, 344-351.

Hall, W. D., 1980: A detailed microphysical model within a two-dimensional dynamic framework: model description and preliminary results. J. Atmos. Sci., 37, 2486-2507.

Hamilton, R. A., and J. W. Archbold, 1945: Meteorology of Nigeria and adjacent territory. Quart. J. Roy. Meteor. Soc., 71, 231-264.

Hane, C. E., C. J. Kessinger and P. S. Ray, 1987: The Oklahoma squall line of 19 May 1977. Part II: Mechanisms for maintenance of the region of strong convection. J. Atmos. Sci., 44, 2866-2883.

Harlow, F. H., and J. E. Welch, 1965: Numerical calculation of time-dependent viscous incompressible flow of fluid with free surface. Phys. Fluids, 8, 2182-2189.

Hauf, T., and T. L. Clark, 1989: Three-dimensional numerical experiments on convectively forced internal gravity waves. Quart. J. Roy. Meteor. Soc., 115, 309-333.

Heymsfield, G. M., and S. Schotz, 1985: Structure and evolution of a severe squall line over Oklahoma. Mon. Wea. Rev., 113, 1563-1589.

Houze, R. A., Jr., 1977: Structure and dynamics of a tropical squall-line system. Mon. Wea. Rev., 105, 1540-1567.

____, and A. K. Betts, 1981: Convection in GATE. Rev. Geophys. Space Phys., 19, 541-576.

____, and E. N. Rappaport, 1984: Air motions and precipitation structure of an early summer squall line over the eastern tropical Atlantic. J. Atmos. Sci., 41, 553-574.

Johnson, R. H., and P. J. Hamilton, 1988: The relationship of surface pressure features to the precipitation and airflow structure of an intense midlatitude squall line. Mon. Wea. Rev., 116, 1444-1472.

Johnston, E. C., 1982: Mesoscale vorticity centers induced by mesoscale convective complexes. Preprints, Ninth Conf. on Weather Forecasting and Analysis, Seattle, Amer. Meteor. Soc., 196-200.

Kane, R. J., Jr., C. R. Chelius and J. M. Fritsch, 1987: Precipitation characteristics of mesoscale convective weather systems. J. Climate Appl. Meteor., 26, 1345-1357.

Kessinger, C. J., P. S. Ray and C. E. Hane, 1987: The Oklahoma squall line of 19 May 1977. Part I: A multiple Doppler analysis of convective and stratiform structure. J. Atmos. Sci., 44, 2840-2864.

Kessler, E., 1969: On the Distribution and Continuity of Water Substance in Atmospheric Circulations. Meteor. Monogr., No. 32, Amer. Meteor. Soc., 84 pp.

Klaassen, G. P., and T. L. Clark, 1985: Dynamics of the cloud-environment interface and entrainment in small cumuli: two-dimensional simulations in the absence of ambient shear. J. Atmos. Sci., 42, 2621-2642.

Koenig, L. R., and F. W. Murray, 1976: Ice-bearing cumulus cloud evolution: numerical simulation and general comparison against observations. J. Appl. Meteor., 15, 747-762.

Krehbiel, P. R., 1986: The electrical structure of thunderstorms. The Earth's Electrical Environment, Nat. Academy Press, 90-113.

Kuettner, J. P., P. A. Hildebrand and T. L. Clark, 1987: Convection waves: observations of gravity wave systems over convectively active boundary layers. Quart. J. Roy. Meteor. Soc., 113, 445-467.

Lafore, J.-P., and M. W. Moncrieff, 1989: A numerical investigation of the organization and interaction of the convective and stratiform regions of tropical squall lines. J. Atmos. Sci., 46, 521-544.

Leary, C. A., 1979: Behavior of the wind field in the vicinity of a cloud cluster in the intertropical convergence zone. J. Atmos. Sci., 36, 631-639.

____, and R. A. Houze Jr., 1979a: The structure and evolution of convection in a tropical cloud cluster. J. Atmos. Sci., 36, 437-457.

____, and ____, 1979b: Melting and evaporation of hydrometeors in precipitation from the anvil clouds of deep tropical convection. J. Atmos. Sci., 36, 669-679.

____, and E. N. Rappaport, 1987: The life cycle and internal structure of a mesoscale convective complex. Mon. Wea. Rev., 115, 1503-1527.

Ley, B. E., and W. R. Peltier, 1981: Propagating mesoscale cloud bands. J. Atmos. Sci., 38, 1206-1219.

Lilly, D. K., 1962: On the numerical simulation of buoyant convection. Tellus, 14, 148-172.

____, 1965: On the computational stability of numerical solutions of time-dependent non-linear geophysical fluid dynamics problems. Mon. Wea. Rev., 93, 11-26.

Lindzen, R. S., and K.-K. Tung, 1976: Banded convective activity and ducted gravity waves. Mon. Wea. Rev., 104, 1602-1617.

Lu, D., T. E. VanZandt and W. L. Clark, 1984: VHF Doppler radar observations of buoyancy waves associated with thunderstorms. J. Atmos. Sci., 41, 272-282.

Maddox, R. A., 1980: Mesoscale convective complexes. Bull. Amer. Meteor. Soc., 61, 1374-1387.

____, 1983: Large-scale meteorological conditions associated with midlatitude, mesoscale convective complexes. Mon. Wea. Rev., 111, 1475-1493.

____, K. W. Howard and D. L. Bartels, 1987: Mesoscale convective complexes in the middle latitudes. Mesoscale Meteorology and Forecasting, Amer. Meteor. Soc., 793 pp.

Mahoney, W. P., III, 1988: Gust front characteristics and the kinematics associated with interacting thunderstorm outflows. Mon. Wea. Rev., 116, 1474-1491.

Mansfield, D. A., 1977: Squall lines observed in GATE. Quart. J. Roy. Meteor. Soc., 103, 569-574.

Marshall, J. S., and W. McK. Palmer, 1948: The distribution of raindrops with size. J. Meteor., 5, 165-166.

McIDAS, 1987: McIDAS (Man Computer Interactive Data Access System) Reference Manual. Space Science and Engineering Center, University of Wisconsin-Madison, 462 pp.

Miller, M. J., and A. K. Betts, 1977: Traveling convective storms over Venezuela. Mon. Wea. Rev., 105, 833-848.

Moncrieff, M. W., and M. J. Miller, 1976: The dynamics and simulation of tropical cumulonimbus and squall lines. Quart. J. Roy. Meteor. Soc., 102, 373-394.

Moore, T. J., R. L. Gall and T. C. Adang, 1989: Disturbances along the Arizona monsoon boundary. Mon. Wea. Rev., 117, 932-941.

Mostek, A., L. W. Uccellini, R. A. Petersen and D. Chesters, 1986: Assessment of VAS soundings in the analysis of a preconvective environment. Mon. Wea. Rev., 114, 62-87.

Nicholls, M. E., 1987: A comparison of the results of a two-dimensional numerical simulation of a tropical squall line with observations. Mon. Wea. Rev., 115, 3055-3077.

____, R. H. Johnson and W. R. Cotton, 1988: The sensitivity of two-dimensional simulations of tropical squall lines to environmental profiles. J. Atmos. Sci., 45, 3625-3649.

____, and M. J. Weissbluth, 1988: A comparison of two-dimensional and quasi-three-dimensional simulations of a tropical squall line. Mon. Wea. Rev., 116, 2437-2452.

NOAA, Climatological Data Arizona; National Environmental Satellite, Data, And Information Service; National Climatic Data Center; Asheville, N.C.; 88 No. 7 and 90 No. 8.

____, Hourly Precipitation Data Arizona; National Environmental Satellite, Data, And Information Service; National Climatic Data Center; Asheville, N.C.; 34 No. 7 and 36 No. 8.

____, Local Climatological Data Monthly Summary Tucson, Arizona; National Environmental Satellite, Data, And Information Service; National Climatic Data Center; Asheville, N.C.; July 1984 and August 1986.

____, Summary of Constant Pressure Data WBAN 33 Tucson, Arizona; National Environmental Satellite, Data, And Information Service; National Climatic Data Center; Asheville, N.C.; July 1984 and August 1986.

Ogura, Y., and M. Liou, 1980: The structure of a midlatitude squall line: a case study. J. Atmos. Sci., 37, 553-567.

____, and N. A. Phillips, 1962: Scale analysis of deep and shallow convection in the atmosphere. J. Atmos. Sci., 19, 173-179.

Orlanski, I., 1975: A rational subdivision of scales for atmospheric processes. Bull. Amer. Meteor. Soc., 56, 527-530.

Peltier, W. R., and T. L. Clark, 1979: The evolution and stability of finite-amplitude mountain waves. Part II: surface wave drag and severe downslope windstorms. J. Atmos. Sci., 36, 1498-1529.

____, and T. L. Clark, 1983: Nonlinear mountain waves in two and three spatial dimensions. Quart. J. Roy. Meteor. Soc., 109, 527-548.

Petersen, R. A., and A. Mostek, 1982: The use of VAS moisture channels in delineating regions of potential convective instability. Preprints, Twelfth Conf. on Severe Local Storms, San Antonio, Amer. Meteor. Soc., 168-171.

_____, D. A. Keyser, A. Mostek and L. W. Uccellini, 1983: Severe storms analysis and forecasting techniques using VAS satellite data. Preprints, Fifth Conf. on Hydrometeorology, Tulsa, Ok., Amer. Meteor. Soc., J29-J32.

_____, L. W. Uccellini, A. Mostek and D. A. Keyser, 1984: Delineating mid- and low-level water vapor patterns in pre-convective environments using VAS moisture channels. Mon. Wea. Rev., 112, 2178-2198.

Pointin, Y., 1985: Numerical simulation of organized convection. Part I: model description and preliminary comparisons with squall line observations. J. Atmos. Sci., 42, 155-172.

Raymond, D. J., 1984: A wave-CISK model of squall lines. J. Atmos. Sci., 41, 1946-1958.

Reap, R. M., 1986: Evaluation of cloud-to-ground lightning data from the western United States for the 1983-84 summer seasons. J. Climate Appl. Meteor., 25, 785-799.

Redelsperger, J.-L., and J.-P. Lafore, 1988: A three-dimensional simulation of a tropical squall line: convective organization and thermodynamic vertical transport. J. Atmos. Sci., 45, 1334-1356.

_____, and T. L. Clark, 1989: On the initiation and horizontal scale selection of convection over gently sloping terrain, (submitted to J. Atmos. Sci.).

Reiter, E. R., and M. Tang, 1984: Plateau effects on diurnal circulation patterns. Mon. Wea. Rev., 112, 638-651.

Robert, A. J., 1966: The integration of a low order spectral form of the primitive meteorological equations. J. Meteor. Soc. Japan, 44, 237-245.

Rotunno, R., J. B. Klemp and M. L. Weisman, 1988: A theory for strong, long-lived squall lines. J. Atmos. Sci., 45, 463-485.

Roux, F., 1988: The west African squall line observed on 23 June 1981 during COPT 81: kinematics and thermodynamics of the convective region. J. Atmos. Sci., 45, 406-426.

Rutledge, S. A., and R. A. Houze Jr., 1987: A diagnostic modeling study of the trailing stratiform region of a midlatitude squall line. J. Atmos. Sci., 44, 2640-2656.

____, and D. R. MacGorman, 1988: Cloud-to-ground lightning activity in the 10-11 June 1985 mesoscale convective system observed during the Oklahoma-Kansas PRE-STORM project. Mon. Wea. Rev., 116, 1393-1408.

____, R. A. Houze Jr., M. I. Biggerstaff and T. J. Matejka, 1988: The Oklahoma-Kansas mesoscale convective system of 10-11 June 1985: precipitation structure and single-Doppler radar analyses. Mon. Wea. Rev., 116, 1409-1430.

Schmidt, J. M., and W. R. Cotton, 1989: Interactions between upper and lower tropospheric gravity waves on squall line structure and maintenance. (submitted to J. Atmos. Sci.).

Sellers, W. D., 1965: Physical Climatology, The University of Chicago Press, 272 pp.

Sheets, R. C., 1979: Some aspects of tropical cyclone modification. Aust. Meteor. Mag., 27, 259-280.

Smagorinsky, J., 1963: General circulation experiments with the primitive equations. I. the basic experiment. Mon. Wea. Rev., 91, 99-164.

Smith, W. P., 1986: The effects of eastern North Pacific tropical cyclones on the southwestern United States. NOAA Tech. Memo. NWS WR-197, 229 pp. [Available from NOAA National Weather Service, Western Region Headquarters, Scientific Services Division, P.O. Box 11188, Federal Bldg., Salt Lake City, Utah 84147.]

Smolarkiewicz, P. K., 1982: The multi-dimensional Crowley advection scheme. Mon. Wea. Rev., 110, 1968-1983.

____, 1983: A simple positive definite advection scheme with small implicit diffusion. Mon. Wea. Rev., 111, 479-486.

____, 1984: A fully multidimensional positive definite advection transport algorithm with small implicit diffusion. J. Comput. Phys., 54, 325-362.

____, and T. L. Clark, 1985: Numerical simulation of the evolution of a three-dimensional field of cumulus clouds. Part I: model description, comparison with observations and sensitivity studies. J. Atmos. Sci., 42, 502-522.

____, and ____, 1986: The multidimensional positive definite advection transport algorithm: further development and applications. J. Comput. Phys., 67, 396-438.

Smull, B. F., and R. A. Houze Jr., 1985: A midlatitude squall line with a trailing region of stratiform rain: radar and satellite observations. Mon. Wea. Rev., 113, 117-133.

____, and ____, 1987a: Dual-Doppler radar analysis of a midlatitude squall line with a trailing region of stratiform rain. J. Atmos. Sci., 64, 2128-2148.

____, and ____, 1987b: Rear inflow in squall lines with trailing stratiform precipitation. Mon. Wea. Rev., 115, 2869-2889.

Sommeria, G., 1976: Three-dimensional simulation of turbulent processes in an undisturbed trade wind boundary layer. J. Atmos. Sci., 33, 216-241.

Srivastava, R. C., T. J. Matejka and T. J. Lorello, 1986: Doppler radar study of the trailing anvil region associated with a squall line. J. Atmos. Sci., 43, 356-377.

Tang, M., and E. R. Reiter, 1984: Plateau monsoons of the Northern Hemisphere: a comparison between North America and Tibet. Mon. Wea. Rev., 112, 617-637.

Thorpe, A. J., M. J. Miller and M. W. Moncrieff, 1982: Two-dimensional convection in non-constant shear: a model of mid-latitude squall lines. Quart. J. Roy. Meteor. Soc., 108, 739-762.

Tripoli, G. J., and W. R. Cotton, 1989a: Numerical study of an observed orogenic mesoscale convective system. Part 1: simulated genesis and comparison with observations. Mon. Wea. Rev., 117, 273-304.

____, and ____, 1989b: Numerical study of an observed orogenic mesoscale convective system. Part 2: analysis of governing dynamics. Mon. Wea. Rev., 117, 305-328.

Wetzel, P. J., W. R. Cotton and R. L. McAnelly, 1983: A long-lived mesoscale convective complex. Part II: Evolution and structure of the mature complex. Mon. Wea. Rev., 111, 1919-1937.

Zipser, E. J., 1969: The role of organized unsaturated convective downdrafts in the structure and rapid decay of an equatorial disturbance. J. Appl. Meteor., 8, 799-814.

____, 1977: Mesoscale and convective-scale downdrafts as distinct components of squall-line structure. Mon. Wea. Rev., 105, 1568-1589.